INVESTIGATION OF THE EFFECT OF PULSE ELECTRIC CURRENT ON DUCTILITY IN LOW AND MEDIUM CARBON STEELS

M.K.D.T. Dhanushka

(218107K)

Degree of Master of Science

Department of Materials Science and Engineering

University of Moratuwa

Sri Lanka

November 2024

INVESTIGATION OF THE EFFECT OF PULSE ELECTRIC CURRENT ON DUCTILITY IN LOW AND MEDIUM CARBON STEELS

M.K.D.T. Dhanushka

(218107K)

Thesis submitted in partial fulfillment of the requirements for the degree Master of Science

Department of Materials Science and Engineering

University of Moratuwa

Sri Lanka

November 2024

DECLARATION OF THE CANDIDATE AND SUPERVISOR

I declare that this is my own work and this thesis does not incorporate without acknowledgement any material previously submitted for a Degree or Diploma in any other University or institute of higher learning and to the best of my knowledge and belief it does not contain any material previously published or written by another person except where the acknowledgement is made in the text.

Also, I hereby grant to University of Moratuwa the non-exclusive right to reproduce and distribute my thesis, in whole or in part in print, electronic or other medium. I retain the right to use this content in whole or part in future works (such as articles or books).

Signature: Date: 06.04.2025

The supervisors should certify the thesis with the following declaration.

The above candidate has carried out research for the Masters thesis under my supervision.

Name of the supervisors	Signature of the supervisors	Date:
Dr. A.A.G.A. Abeygunawardena		2025 / 04 / 07
Prof. G.I.P. De Silva		2025-04-07

ABSTRACT

The motivation to do the research is to investigates the impact of the electroplasticity phenomenon on the mechanical behavior of two plain carbon steel samples with different carbon contents (0.09 wt.% and 0.39 wt.%) under uniaxial tensile loading combined with low-frequency high amplitude electrical pulses. Prior to the tensile tests, all samples underwent normalization heat treatment. The experimental results demonstrate a progressive decrease in yield stress accompanied by an improvement in ductility as the pulse frequency increases, up to a frequency of 0.83 Hz. These findings suggest a positive influence of the electroplasticity effect on the tensile properties of plain carbon steels. However, beyond 0.83 Hz, despite further reduction in yield stress, a gradual decline in ductility is observed until a frequency of 1.64 Hz, primarily attributed to enhanced strain localization and induced defects resulting in premature fracture.

Microstructural analysis reveals that the fracture surfaces of samples tested under electrical current exhibit intermediate grain sizes between non-deformed samples and deformed samples tested without current. Additionally, the presence of characteristic dimples on the fractographs further supports the observed variation in ductility with pulse frequency. Notably, the combination of a pulse frequency of 0.83 Hz and an effective current of 777.8 A yields a significant enhancement in formability.

Furthermore, the tensile tests under electric current resulted in increased toughness and fracture strain for both steels compared to normal tests. Simulation results indicate that the maximum temperature accumulation within the material is insufficient to induce phase transformation, and the electroplasticity effect is responsible for reducing the lateral contraction of grains. These findings demonstrate that significant formability enhancement can be achieved by employing this specific combination of pulse frequency and effective current, significantly contributing to understanding the interplay between pulse current and material response, providing valuable insights for optimizing manufacturing techniques and design considerations for plain carbon steel components.

KEY WORDS: Electroplasticity effect, electrically assisted forming, plain carbon steel, uniaxial tensile test, pulsed current

ACKNOWLEDGEMENT

The MSc full-time research project marks a significant milestone in my academic journey. I have been fortunate to receive support and assistance from many individuals who contributed to the successful completion of this research project. I would like to extend my heartfelt gratitude to all who have played a role in making this research a success.

First, I would like to express my deepest thanks to my project supervisors, Dr. A.A.G.A. Abeygunawardena and Dr. G.I.P. De Silva, who introduced me to the project's background and provided essential guidelines for the literature study. Their constant readiness to offer valuable guidance and passionate supervision was crucial for the success of this project.

I also extend my gratitude to all the academic staff of the Department of Material Science and Engineering at the University of Moratuwa, particularly Mr. V. Sivahar, the Head of the Department of Material Science and Engineering. Special thanks go to Dr. Chandima Dedduwa for his continuous support and facilitation whenever needed.

I acknowledge the staff of the Department of Material Science and Engineering, Department of Electrical Engineering, particularly Mr. Keerthi, the technical officer of Electrical Machines Laboratory, for their immense support in providing facilities for laboratory tests and sample fabrication.

Finally, I take this opportunity to express my gratitude to all others, including my colleagues, who have offered me support, courage, and guidance throughout this research work.

TABLE OF CONTENT

LIST OF FIGURES

LIST OF TABLES

LIST OF ABBREVIATIONS

AISI	American Iron and Steel Institute
ASTM	American Society for Testing and Materials
CNC	Computer numerical control
EA	Electricity Assisted
EP	Electroplasticity
EAPW	Electrically-Assisted Pressure Welding Process
FCC	Face-Centered Cubic
FEA	Finite Element Analysis
SEM	Scanning Electron Microscope
TEM	Transmission Electron Microscope
UTS	Ultimate Tensile Strength

1 INTRODUCTION TO RESEARCH

1.1 Background of the research

Steel, especially plain carbon steel, is extensively utilized in engineering applications due to its diverse microstructures and desirable properties which can be achieved through metal forming processes and heat treatments [1,2]. The manipulation of its microstructure allows for the customization of mechanical properties such as hardness, toughness, and ductility, making it an indispensable material across various industries. Moreover, the alloying potential of carbon steel enables the creation of tailored compositions to meet specific application requirements, further enhancing its versatility in engineering applications. However, traditional metal forming methods have notable drawbacks, including limitations in achieving intricate shapes with high precision and the need for elevated temperatures, which can lead to increased energy consumption and material waste.

To address these challenges, there has been a growing interest in advanced manufacturing techniques, with electrically-assist forming emerging as a transformative solution [3,4]. By incorporating controlled electrical currents into the metal forming processes, this innovative approach not only overcomes the drawbacks of traditional methods but also opens new avenues for enhanced formability at room temperature. The application of electrical energy introduces a dynamic interplay between thermal and mechanical effects, reducing forming forces and allowing for the efficient shaping of materials, even those with inherently poor deformability. As research in electrically-assisted forming progresses, the potential to achieve superior precision, energy efficiency, and tailored material properties continues to position this method as a promising frontier in the evolution of steel-based engineering applications.

Furthermore, electrically-assisted forming offers a more sustainable alternative to traditional methods, as it minimizes the environmental impact associated with high-temperature processes and reduces the overall energy consumption during manufacturing.

The precise control afforded by this technique not only improves the quality of formed components but also contributes to waste reduction by minimizing material overuse and enhancing the recyclability of processed steel.

In addition to its environmental benefits, electrically-assisted forming introduces a level of flexibility previously unseen in conventional metalworking. The ability to selectively apply electrical currents enables localized adjustments in temperature and strain distribution, paving the way for the creation of complex geometries with improved accuracy. This capability is particularly advantageous in industries where intricate and customized components are integral, such as aerospace and automotive manufacturing.

The synergy of electrical and mechanical forces in the forming process also allows for novel opportunities in achieving superior material properties. Through careful modulation of electrical parameters, such as current density and frequency, engineers can precisely control phase transformations and grain refinement in the steel microstructure. This level of microstructural control results in components with enhanced strength, corrosion resistance, and fatigue performance, meeting the stringent requirements of modern engineering applications.

As electrically-assisted forming continues to evolve, ongoing research and development promise even more innovative applications. The integration of advanced sensing technologies and real-time process monitoring further refines the precision and reliability of this method.

1.2 Research problem

Despite recent advancements in alloy design that have introduced task-specific alloy steels with enhanced structure-property relationships, conventional plain carbon steels remain widely used in the industry due to their versatility [1]. However, their limited formability and the shortcomings of traditional metal forming methods have prompted the adoption of advanced techniques like powder metallurgy and Electrically Assisted Manufacturing (EAM), a hybrid metal forming method. Studies such as V. I. Stashenko et al, has explored the effects of electric current on electroplastic drawing on medium-Carbon Steel. Yet, the influence of pulsed electric current on low carbon steel during tensile deformation remains unexplored, despite its widespread use in engineering for its moderate formability and low cost. Prior research by the authors has demonstrated the reduction of flow stress in low carbon steel under pulsed electric current. In this work, plain carbon steel samples with 2 different carbon contents were subjected to uniaxial tensile forces and synchronous electrical pulses with low frequency and high current amplitudes to examine the effects on microstructure and flow stress, with a focus on the role of carbon content.

1.3 Objectives

Objectives of this research are as follows

1. To propose appropriate parameters for pulsed electric current by conducting a comprehensive literature review on its effects on low and medium carbon steels.
2. To investigate the microstructural changes induced by pulsed electric current and correlate them with variations in ductility and yield stress.
3. To develop a simulation model to analyze the thermal effect of pulsed electric current and validate the results with experimental data.

The variation in flow stress under different pulse current amplitudes and pulse frequencies is examined in plain carbon steel with different carbon compositions. These variations are better understood by studying the microstructural analysis near the fracture surface of the broken specimens, as this region experiences the highest deformation relative to other areas. While surface temperature can be monitored through a thermal camera during tensile testing, it is necessary to confirm whether the observed microstructural changes are a result of recrystallization due to increased internal temperature caused by joule heating. To investigate this, a Multiphysics based simulation was conducted to determine the internal temperature of the specimen.

2 LITERATURE REVIEW

2.1 Plain carbon steels

The intricate definition of the term 'Steel' encompasses a diverse array of materials and alloys, each displaying variations in production methods, compositions, and alloying elements. At its essence, steel is recognized as an alloy predominantly constituted of iron, with carbon serving as a pivotal component, accompanied by potential impurities or intentional alloying elements like Phosphorous, Sulphur, and Manganese. It is noteworthy that while many steels adhere to specified minimum carbon content, not all necessitate substantial carbon quantities. Deliberate alloy additions are employed to curtail carbon levels in solution, mitigating its inclination to form carbides. The manifestation of steel in various sizes and shapes undergoes diverse forming operations such as rolling, forging, and heat treatments, refining its properties and toughness through crystalline structure enhancement.

In contrast, plain carbon steel, an alloyed iteration of iron and carbon, incorporates manganese and residual elements, which may originate from raw materials during production or be intentionally introduced for specific purposes, diverging from alloying elements added based on stipulated minimum amounts. The meticulous categorization of plain carbon steels is underscored by the comprehensive definition provided by the American Iron and Steel Institute (AISI), which outlines specified limits for manganese, silicon, and copper content within this class, emphasizing the meticulous nature of steel classification within the broader domain of metallurgy [5]. Furthermore, plain carbon steels can be categorized into three major classes low carbon, medium carbon, and high carbon steels based on the weight percentage of carbon present.

Low carbon steels, marked by a carbon percentage up to 0.30%, constitute a substantial component in contemporary steel applications. Notably, these steels exhibit microstructures comprised of ferrite and pearlite, rendering them relatively soft yet exceptionally ductile and tough. Their distinctive proprieties include good formability, good weldability, 55 – 60% weldability, lack of hardenability and cost-effectiveness compared to other steel classes. Found primarily in flat-rolled products like sheets or strips, low carbon steels undergo diverse processes such as cold rolling, subcritical annealing, and tempered-rolled conditions. This comprehensive understanding contributes to the meticulous categorization of plain carbon steels, emphasizing their varied compositions and mechanical properties tailored to specific industrial and structural requirements [6].

Medium-carbon steels, characterized by carbon levels between 0.30% and 0.55% and manganese ranging from 0.60% to 1.65%, occupy a vital niche in applications requiring elevated mechanical properties. Bridging the gap between low and high carbon steels, they offer enhanced strength, 60-70% machinability, and fair formability. Fabrication processes, including hardening and heat treatment, render them versatile for various applications, with treatments like annealing, normalizing, or quenching and tempering further expanding their utility. While predominantly utilized in tempered conditions, medium-carbon steels exhibit a tempered microstructure and limited hardenability, restricting effective heat treatment to thin sections with rapid quenching rates. Despite their mechanical superiority over low carbon steels, trade-offs in ductility and toughness are acknowledged. With carbon content reaching up to 0.5%, these steels may undergo cold drawing for specific mechanical properties, allowing certain applications without the necessity of heat treatment. However, it is crucial to consider the inherent limitations when comparing medium-carbon steels to alloy steels [6,7].

High carbon steels represent the epitome of hardness and strength within the carbon steel spectrum, making them exceptionally well-suited for applications requiring robustness and wear resistance. Characterized by sharp cutting edges upon fabrication, these steels are commonly employed in the hardened and tempered condition. The compositional range of 0.55% to 1.00% carbon and 0.30% to 0.90% manganese distinguishes high carbon steels, emphasizing their unique mechanical properties. However, these impressive mechanical attributes come with inherent trade-offs, including higher production costs and challenges in formability and weldability. These limitations impose restrictions on their applications, especially when compared to their medium carbon counterparts. The nuanced balance between superior hardness and strength on one hand and limitations in formability and weldability on the other underscores the intricate considerations involved in selecting high carbon steels for specific engineering contexts [1, 6].

2.2 Microstructures and thermal processing of plain carbon steels

The performance characteristics of steel are intricately tied to its microstructural properties, encompassing the spatial arrangements, volume fractions, sizes, and morphologies of distinct phases constituting a macroscopic section of steel with a specific composition under given processing conditions. Furthermore, key aspects of the iron-iron carbide system, as illustrated in Figure 2.1, exert significant influence over the resultant microstructure, morphology, phases, and constituents, thereby governing the behavior of plain carbon steel.

The principal constituents within the microstructure of plain carbon steels are the three primary phases: ferrite, cementite, and pearlite. It is crucial to emphasize that these phases necessitate a deliberate, slow cooling process (equilibrium cooling) to preclude the formation of other metastable phases, such as cementite (Fe3C).

The microstructural configuration in plain carbon steel is contingent upon its carbon content. Figure 2.2 provides a visual representation of the microstructures for typical low-carbon, medium-carbon, eutectoid, and high-carbon steels, in conjunction with other phases. In Figure 2.2(a), corresponding to low-carbon steel (below 0.8% C), the microstructure comprises ferrite and pearlite. With increasing carbon content, as evidenced in the microstructure of medium-carbon steel in Figure 2.2(b), featuring proeutectoid ferrite and pearlite, the proportion of pearlite phase, identified by the dark etching constituent, incrementally elevates [1].

Upon surpassing 0.8% carbon content, exemplified by eutectoid steel in Figure 2.2(c), the entire microstructure is characterized by pearlite, manifested as a dark constituent constituting 100% of the structure. Beyond this carbon threshold, an additional

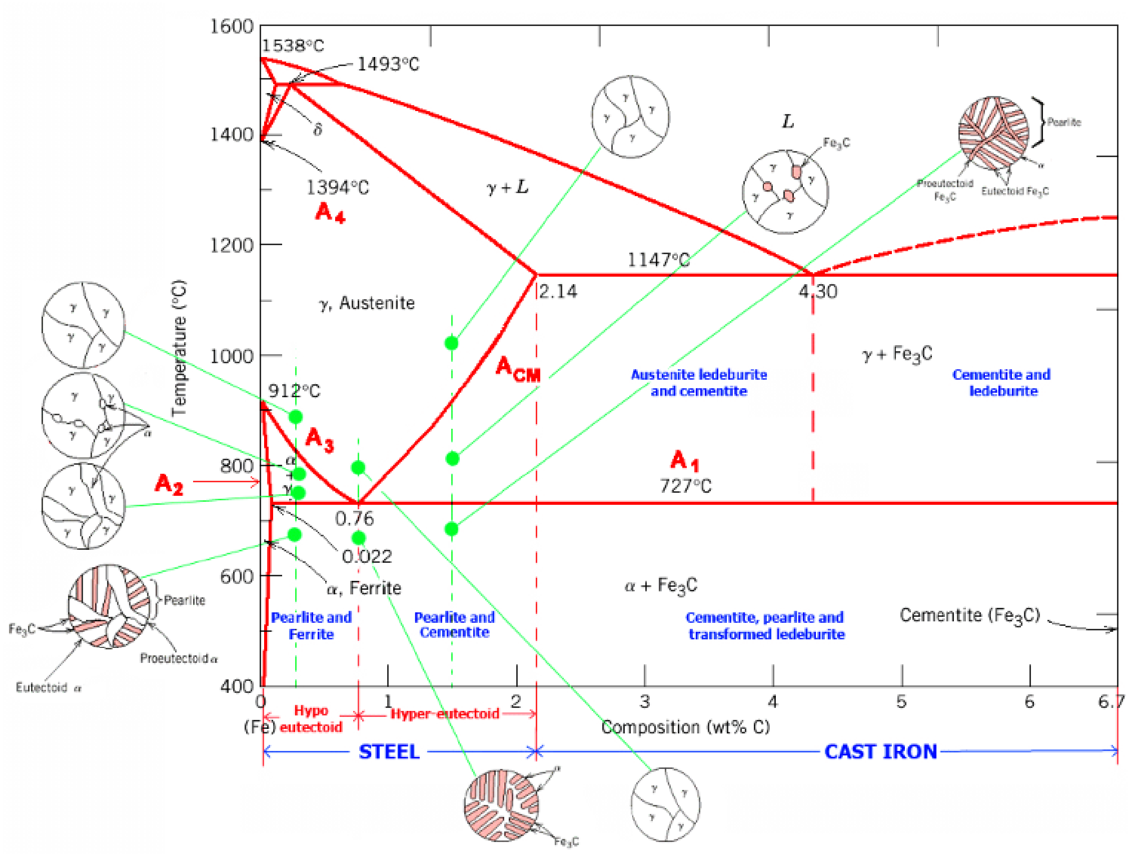

Figure 2.1: Iron – Carbon phase diagram [10]

(A 1: The upper limit of the ferrite / cementite phase field (horizontal line going through the eutectoid point). A2: The temperature where iron looses its magnetism (so-called Curie temperature). Note that for pure iron this is still in the α-phase. A3: The boundary between the γ austenite and the austenite/ ferrite field. A4: The point in this case where α changes to δ at high temperatures. ACM: The boundary between the γ austenite and the austenite / cementite field.)

constituent, proeutectoid cementite, is observed in Figure 2.2(d), appearing white and prevalent in the equilibrium microstructure of high-carbon steels [8,9]. This proeutectoid cementite forms a continuous network surrounding pearlite grain boundaries, particularly evident with higher carbon content, as depicted in Figure 2.2(e).

In the context of understanding and manipulating steel microstructures, heat treatment plays a crucial role. Defined as a series of operations involving the controlled heating and cooling of a metal or alloy, heat treatment aims to induce specific microstructural changes and achieve desired mechanical properties. This is particularly relevant in the case of mild

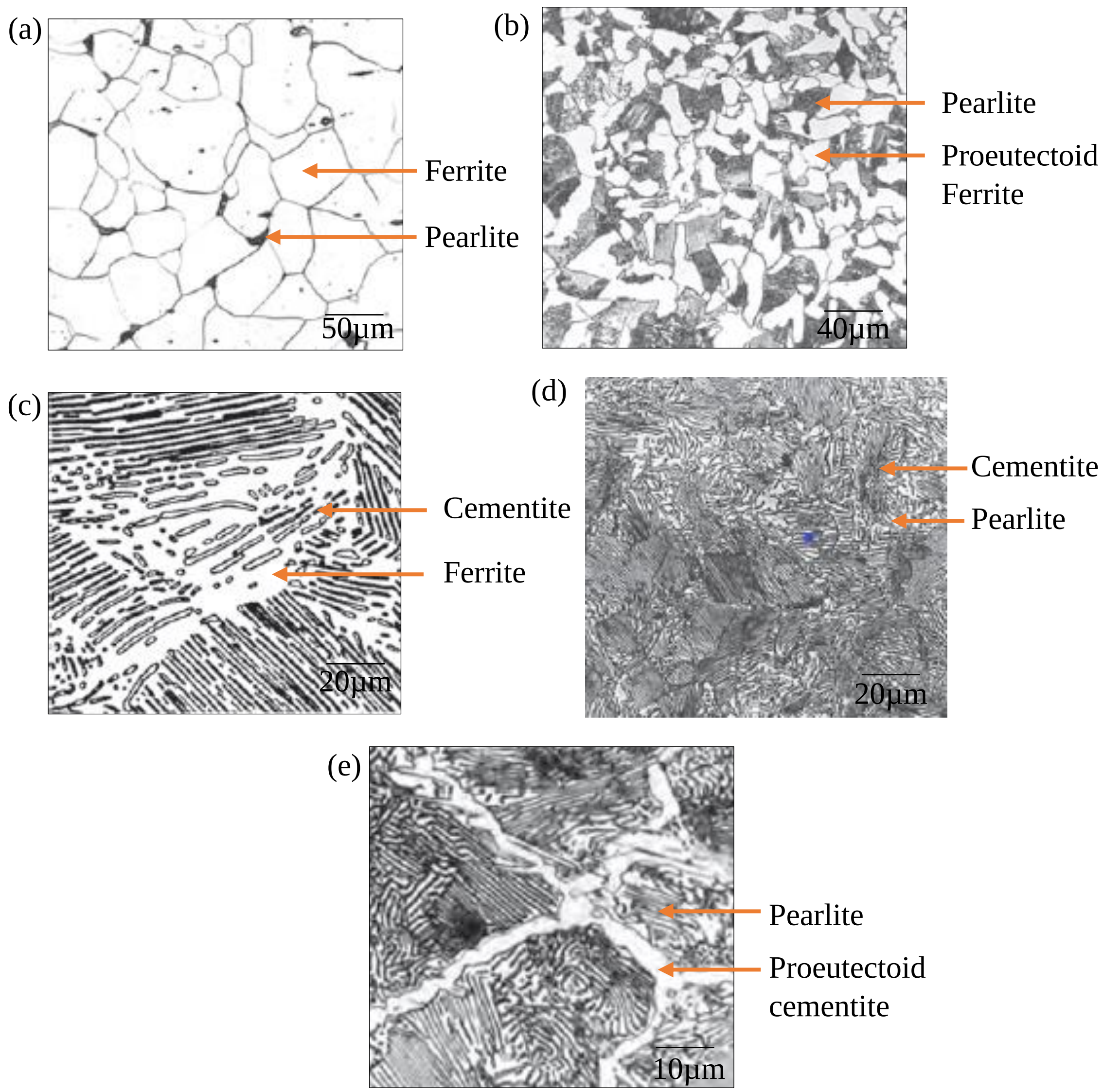

Figure 2.2: Microstructures of plain carbon steels with corresponding phases at room temperature. [1].

(a) Low carbon steel micrograph of low-carbon AISI/SAE 1010 steel showing a matrix of ferrite grains (white etching constituent) and pearlite (dark etching constituent). Etched in Marshall's reagent followed by 2% nital.200×). (b) Medium carbon steel micrograph of medium - carbon AISI/ SAE 1040 steel showing ferrite grains (white etching constituent) and pearlite (dark etching constituent). Etched in 4% picral followed b y2% nital. 300×). (c) Pearlite in eutectoid steel figure shows pearlite microstructure consisting of alternating layers of ferrite (the light phase) and Cementite, Fe3C (thin layers most of which appear dark). 500×. (d) High carbon steel micrograph of high – carbon AISI/ SAE 1095 steel showing a matrix of pearlite and some grain boundary cementite. Etched in 4% picral. 500×. (e) High carbon steel with cementite network microstructure consisting of proeutectoid cementite network surrounding the pearlite colonies in 1.4 wt. %C steel. 1000×.

steel, where the solid-state processes of annealing, normalizing, hardening, and tempering are pivotal. These heat treatments are extensively employed to modify the microstructure of engineering materials, with a direct impact on crucial mechanical properties such as hardness, toughness, yield strength, ultimate tensile strength, Young's modulus, percentage elongation, and percentage reduction.

In metallurgy, precision heat treatments are pivotal for tailoring steel microstructures. Annealing, a meticulously controlled process, involves heating materials to a specific temperature and maintaining it before gradual cooling. This method is crucial for softening iron or steel, refining grain structures, and inducing a ferrite-pearlite microstructure. Applied where elongation and tensile strength are paramount, the heating temperature is meticulously adjusted for desired toughness and hardness. Similarly, normalizing subjects materials to the austenitic temperature range, followed by rapid air cooling, resulting in a predominantly pearlite matrix. This enhances strength and hardness beyond the as-received condition, concurrently eliminating undesirable free carbides. Both annealing and normalizing exemplify indispensable tools, allowing engineers to precisely engineer steel microstructures for diverse applications [11] The prediction of microstructure transformations is a prerequisite for successfully estimating mechanical properties post-heat treatment and for understanding the generation of stresses and strains during this process. The modeling of phase transformations stands out as a key challenge in the broader modeling of heat treatment [12].

2.3 Forming methods of plain carbon steels

Metal forming constitutes a diverse array of manufacturing techniques employed to fabricate metal components or machined workpieces, transforming raw materials into finished goods. Through the application of forces such as tension, compression, shear, and others, the material undergoes deformation, leading to the creation of desired shapes. However, imperfections persist in manufactured items, primarily stemming from the inherent challenge of achieving uniformity in production, resulting in shape errors. For instance, in the cold rolling of nuts, slight deformations are intentionally introduced to prevent their rotation inside bolts post-installation—an imperative adjustment that becomes negligible when employing steel screws instead of bolts. Despite the continuous refinement of forming processes, the inevitability of shape errors underscores the complexity of achieving absolute precision in metal component manufacturing. Notwithstanding these challenges, metal forming processes find widespread application in the production of a diverse range of products, encompassing automobiles, aircraft, cutlery, tools, machinery parts, and various other industrial applications.

Plain carbon steels are fundamental materials extensively used in various industries due to their excellent mechanical properties, cost-effectiveness, and ease of manufacturing. The forming processes employed in shaping these steels play a crucial role in determining their final properties and performance. Table 2.1 shows some advantages and disadvantages of several metal forming processes [13-15].

Table 2.1 Advantages and disadvantages of several metal forming processes

Process	Advantages	Disadvantages
Hot forging	• Improved Material Flow: At higher temperatures, metals exhibit better plasticity and deformability. This results in improved material flow during the forging process, allowing for intricate shapes and complex geometries to be formed more easily. • Reduced Strain and Energy Requirements: Hot forging requires less force compared to cold forging. The reduced strain on the equipment and dies results in lower energy requirements for the overall process. • Minimized Workpiece Defects: Hot forging helps minimize the likelihood of defects such as cracks and voids in the final product. The elevated temperatures allow the metal to deform more uniformly, reducing the risk of internal flaws. • Improved Surface Finish: The elevated temperatures during hot forging help reduce surface defects and improve the overall surface finish of the forged components. This can lead to a	• Warpage Risk and Tolerance Precision: A notable drawback of hot forging, in comparison to cold forging, lies in the potential for warping of certain metals if not meticulously monitored during the heating, forging, and cooling phases. This tendency results in less precise tolerances when compared to metals forged through cold forming. • Higher Cost Implications: Hot forging is often accompanied by higher costs compared to cold forging, primarily due to the requisite heat treatment at the onset of the forging process and the subsequent cooling phase aimed at averting warping. The automation of this heat treatment, particularly on an industrial scale, may necessitate additional initial investments in specialized tools. • Tool Wear and Maintenance: The elevated temperatures during hot forging contribute to increased tool wear. The harsh conditions can accelerate tool degradation, requiring frequent maintenance and replacement, which adds to operational costs.

	higher-quality final product with better aesthetics. • Applicability to High Formability Metals: Hot forging is notably advantageous for metals with a high formability ratio. The elevated temperatures do not compromise the structural integrity of the metal, enabling facile shaping without introducing defects. Consequently, the resulting metal components exhibit a harmonious combination of strength and ductility.	• Surface Oxidation and Scale Formation: The exposure of metals to high temperatures during hot forging increases the likelihood of surface oxidation and scale formation. This requires additional post-forging processes, such as cleaning or pickling, to address surface imperfections. • Environmental Considerations: The high temperatures involved in hot forging can contribute to emissions and environmental concerns. Efficient mitigation measures, such as waste heat recovery systems, are necessary to address the environmental impact associated with the energy-intensive nature of hot forging.
Cold forging	• Economic Efficiency: Cold forging, occurring without pre-heating, offers economic advantages, particularly in the automotive industry. The final product often requires minimal or no finishing, reducing overall production costs. • Material Utilization: The net weight of the original metal remains essentially unchanged in the finished product during cold forging. This efficient material utilization minimizes	• Reduced Ductility: Cold forging results in a reduction in the ductility of the metal. The absence of elevated temperatures during the process can lead to increased brittleness in certain materials, limiting their formability. • Limited Deformation Capability: Cold forging may have limitations in the degree of deformation that can be achieved, particularly for certain materials.

	excess waste, contributing to both economic and environmental considerations. • Extended Die Lifespan: Cold forging operations exhibit prolonged die lifespan compared to hotter processes. The absence of extreme temperatures reduces wear on the dies, leading to fewer replacements and lower maintenance costs. • Reduced Surface Defects: Cold forging minimizes surface defects such as scale and oxidation, leading to a superior surface finish. This reduces the need for additional finishing processes and contributes to the overall quality of the forged components.	This can impact the ability to form intricate or highly complex shapes compared to processes that involve higher temperatures. • Potential for Surface Cracks: Cold forging, especially in materials prone to strain hardening, can lead to the development of surface cracks. These cracks may occur due to the increased hardness resulting from the deformation at lower temperatures. • Limited Applicability to Certain Alloys: Some alloys may not be well-suited for cold forging due to their sensitivity to low-temperature deformation. This limitation in material applicability restricts the range of alloys that can be effectively processed through cold forging. • Strain Localization: Cold forging can lead to strain localization, where excessive deformation occurs in localized regions of the material. This can result in uneven material flow and potential defects in the final product.
Hot extrusion	• Enhanced Formability: The elevated temperatures during hot extrusion increase the formability of metals. This allows for the production of complex	• Tool Wear and Maintenance: The elevated temperatures during hot extrusion can accelerate wear on the tools and dies. The harsh conditions may necessitate

	shapes and intricate profiles that may be challenging to achieve through cold extrusion. • Improved Surface Finish: Hot extrusion often results in a smoother and more refined surface finish compared to cold extrusion. The higher temperatures contribute to better material flow and reduced surface imperfections. • Lower Extrusion Forces: The reduced flow stress at higher temperatures means that lower extrusion forces are required during hot extrusion. This can contribute to less wear on the equipment and tooling, potentially extending their lifespan. • Improved Microstructure and Grain Refinement: The elevated temperatures during hot extrusion promote recrystallization and grain refinement in the metal microstructure. This often results in improved mechanical properties, including enhanced strength and toughness.	frequent maintenance and replacement of tooling, contributing to operational costs. • Surface Oxidation and Scaling: The high temperatures involved in hot extrusion can lead to surface oxidation and scaling on the extruded product. This may require additional post-extrusion processes, such as cleaning or pickling, to address surface imperfections. • Energy Intensive: Hot extrusion typically requires higher energy consumption compared to cold extrusion. The need for elevated temperatures contributes to increased energy demands, impacting the overall energy efficiency of the manufacturing process. • Limited Complexity in Geometries: While hot extrusion is suitable for a wide range of shapes, achieving extremely intricate or highly detailed geometries may be challenging due to the limitations associated with material flow and die design at elevated temperatures. • Increased Material Oxidation: The exposure of the material to high temperatures increases the risk of oxidation. This can impact

		the material properties and require additional protective measures or post-processing steps to address oxidation-related issues.
Cold extrusion	• Reduced Risk of Thermal Cracking: The absence of rapid cooling after extrusion reduces the risk of thermal cracking in certain materials. Cold extrusion provides a controlled process with gradual cooling, minimizing the potential for thermal stresses and cracks. • Reduced Material Waste: Cold extrusion is known for its efficiency in material utilization. The process generates less waste compared to hot extrusion, as minimal machining is usually required after forming. • Extended Tool Life: Cold extrusion often results in lower tool wear compared to hot extrusion. The absence of high temperatures reduces stress on the tools, contributing to longer tool life and reduced maintenance costs. • Reduced Material Waste: Cold extrusion is known for its efficiency in material utilization. The process generates less waste compared to hot extrusion, as minimal machining is usually required after forming.	• Strain Hardening Effects: Cold extrusion can induce strain hardening in the material, leading to increased hardness and reduced ductility. This may affect subsequent manufacturing processes and could necessitate additional annealing steps. • Potential for Surface Defects: Cold extrusion may result in surface defects, such as scratches or marks, due to the higher frictional forces involved in the process. These defects may require additional finishing processes to meet quality standards. • Higher Extrusion Forces: Cold extrusion generally requires higher extrusion forces compared to hot extrusion. The increased forces may lead to greater stress on equipment and tooling, potentially reducing their lifespan and requiring more frequent maintenance. • Limited Formability for Certain Materials: Cold extrusion may be less suitable for materials with limited ductility at room

		temperature. Some materials may not deform easily without the application of heat, restricting the range of metals that can be effectively processed.
Deep drawing	• Complex Shape Formation: Deep drawing allows the production of complex and intricate shapes with a single operation. This is particularly beneficial for creating seamless and deep containers, cups, and other components with intricate geometries. • High Production Speed: Deep drawing can be a high-speed manufacturing process, making it suitable for large-volume production. The rapid forming of sheet metal into various shapes contributes to increased throughput and efficiency • Tight Tolerances and Precision: Offers high dimensional precision and tight tolerances in the final product. The use of dies and a controlled forming process ensures accuracy and consistency in the shape and dimensions of the formed components. • Enhanced Surface Finish: Often results in a smooth surface finish on the formed components. This reduces the need for additional finishing processes,	• Material Grain Direction Considerations: The direction of the material's grain can impact the success of the deep drawing process. Proper consideration of the grain direction is crucial to avoid issues such as cracking and tearing during forming. • Tool Wear and Maintenance: The forces involved in deep drawing can lead to wear on the dies and punches over time. Regular maintenance and potential replacement of tooling are necessary to ensure consistent product quality. • Springback Effects: After the deep drawing process, certain materials may exhibit springback, where the formed part partially returns to its original shape. Springback can affect the accuracy of the final dimensions and may require additional measures to compensate. • Edge Cracking in Certain Materials: Some materials, especially brittle ones, may be prone to edge

	contributing to overall manufacturing efficiency. • Cost-Effective for Large Production Runs: Particularly cost-effective when producing components in large quantities. The high-speed, efficient nature of the process contributes to economies of scale and overall cost savings.	cracking during the deep drawing process. This issue can affect the quality of the final product and may necessitate additional process adjustments. • Material Thickness Limitations: Deep drawing may have limitations on the thickness of the material that can be effectively drawn. Thicker materials may require more force and could pose challenges in achieving uniform deformation.
Hydrodynamic forming	• Reduced Heat Generation: Unlike some traditional forming processes, hydrodynamic forming generates minimal heat during the process. This is advantageous for materials that are sensitive to heat-induced changes in properties. • Uniform Deformation: Hydrodynamic forming ensures uniform deformation of the material. The high-pressure fluid evenly distributes forces, resulting in consistent shapes and dimensions across the formed component. • Complex Geometries: This process allows for the formation of complex and intricate geometries that may be challenging to achieve with traditional forming methods. The fluid pressure can reach into	• Limited Forming Pressure for Certain Materials: Hydrodynamic forming may have limitations in achieving very high forming pressures, which can be essential for certain materials or applications requiring intense deformation. • Dependency on Fluid Properties: The effectiveness of hydrodynamic forming is influenced by the properties of the fluid used, including viscosity and pressure. Variations in these properties can impact the consistency and precision of the forming process. • Limited Control over Material Flow: Compared to traditional forming processes where tool movements

	intricate details, facilitating the production of highly detailed components. • Improved Surface Finish: Hydrodynamic forming can result in a smooth and high-quality surface finish on the formed components. The absence of tool marks and reduced friction contribute to the improved surface aesthetics.	are precisely controlled, hydrodynamic forming may offer limited control over the material flow. This can affect the final geometry, especially in complex shapes. • Complex Tooling Design: The design and fabrication of the forming tools, such as diaphragms or bladders, can be complex and may require careful engineering. This complexity can contribute to higher initial tooling costs.

the shift towards electricity-assisted metal forming processes from traditional methods is imperative due to their ability to overcome inherent limitations. These processes offer enhanced formability for challenging materials, reduce forming forces, improve material properties, increase precision, and address issues such as springback. Embracing electricity-assisted techniques is a strategic move towards more efficient and versatile manufacturing, ensuring the capability to meet the evolving demands of modern industries.

2.4 Electroplasticity concept

Electroplasticity is a concept within materials science and metallurgy that involves the application of electrical energy to induce plastic deformation in metallic materials. This phenomenon exploits the interaction between electrical current and the mechanical behavior of metals, leading to enhanced formability and improved properties. During electroplasticity, an electric current is passed through the metal, generating localized heating and modifying the material's microstructure. This, in turn, results in reduced flow stress and increased ductility, allowing for easier deformation and shaping of the material.

One of the key aspects of electroplasticity is its ability to influence the dislocation movement within the crystal lattice of metals. The application of electrical current facilitates the migration of dislocations, which are crystal defects responsible for plastic deformation, leading to a more malleable material. This concept has significant implications for metal forming processes, as it enables precise control over deformation mechanisms and enhances the overall manufacturability of metallic components. Despite the fact that the underlying physics governing electroplasticity in metals remains elusive, past research papers have put forth several hypotheses aimed at unraveling this intricate concept.

Enhancement of the plasticity by irradiating with 1MeV electron beam on a zinc single crystal during the tensile deformation was first observed by Troitskii and Likthtman. Furthermore, a reduction of flow stress required to continue plastic deformation was observed when the beam was applied along with the slip plane [16]. Over time, instead of using an electron beam, pulse electric current has been used by researchers to study the flow stress reduction during plastic deformation of the metals while keeping the theory persisted.Following the discovery of the Electroplasticity (EP) effect, Kravchenko [17] proposed a theoretical framework to elucidate this phenomenon. In his proposition, Kravchenko posited that the directed motion of electrons imparts a force on the dislocations within the crystal lattice of metallic materials. This "electron wind" force, denoted as Few, was quantitatively estimated using Equation (1), representing a physics-based expression derived from quantum mechanics and characterized as a microscopic parameter.

$$F_{ew} \sim \frac{b}{4}\left(\frac{v_e}{v_d} - 1\right)\frac{v_d \delta n_e}{v_F \delta \mu_c}\Delta^2 \tag{1}$$

Where, F_{ew} is electron wind force, b is the burger’s vector, v_e denotes the electron drift velocity, $v_d$is the dislocation velocity, v_F is the electron fermi velocity, n_e denotes the concentration of the free electrons, μ_c represents the chemical potential and Δ is a material constant of the deformation potential

The equation, presented in scalar form, encapsulates the directionality of the force along the dislocation length contingent upon the electric charge of the dislocation. Kravchenko's "electron wind" theory [17] introduced a non-thermal mechanism to account for the Electroplasticity phenomenon, asserting an equivalence between the effects of electric current on dislocations and mechanical forces and stresses. Yu. I. Bolko et al. [18] conducted measurements on copper, gold, and tungsten samples to investigate the directional influence of an electron wind on dislocations in metals. The choice of these metals was based on both experimental convenience and their representation of n-type (Cu, Au) and p-type (W) conduction, wherein an electron wind is directed in opposite ways. Single crystals of copper and gold were prepared by melting and slow cooling on a sapphire substrate, while tungsten spheres were formed through high-voltage arc melting. The experiments involved passing a short-duration ($t = 10^{-9}$ sec) single direct current (dc) pulse through a compressed spherical single crystal and measuring the difference between pole contact areas as a function of the current. Notably, the results revealed that the drag of dislocations by the current in n-type conductors (Cu, Au) and a p-type conductor (W) occurred in opposite directions. This critical finding supports the proposed notion that the observed effect is specifically attributed to the action of an electron wind on dislocations, excluding alternative explanations. The divergence in the drag directions

in p- and n-type conductors reinforces the validity of the conceptualization of the role of an electron wind in dislocation mass transfer within metals [18].

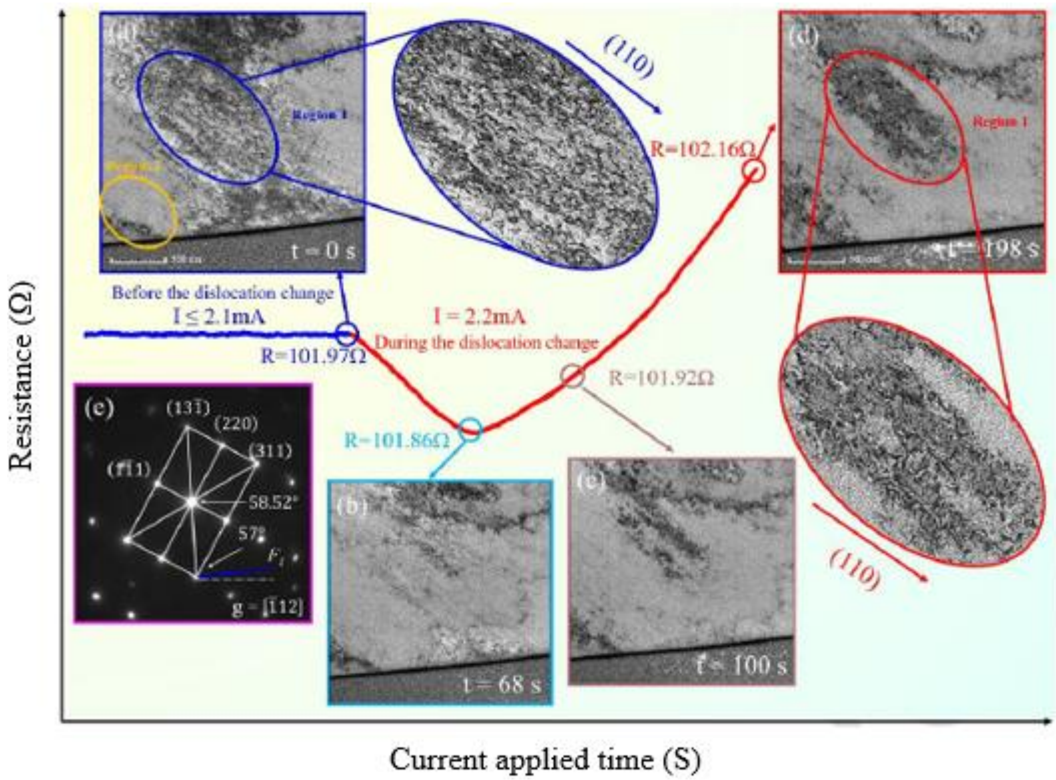

Figure 2.3: Resistance evolution of the sample with the corresponding dislocation structures with the electric current applied time: (a–d) the TEM images showing the evolution of dislocations captured from the electrical in-situ TEM experiment; (e) the diffraction spot of the observed plane [19].

Xin Zhang et al. [19] investigate the dynamic evolution of dislocations in a single-crystal superalloy subjected to electric current. The experimental sample, chosen for its small size, lacked grain boundaries, precipitates, and solute atoms, focusing the study solely on dislocation evolution. The resistance of the sample was observed to be influenced solely by dislocation behavior, as depicted in Figure 2.3. At electric current values below 2.1 mA, dislocations remained stationary, and the resistance exhibited minimal changes. However, as the electric current surpassed 2.2 mA, dislocations initiated movement, leading to a nuanced evolution of dislocation structures with varying current application times. Particularly noteworthy was the observation that dislocations underwent annihilation and subsequent regeneration in specific regions, showcasing the intricate interplay between electron force and dislocation dynamics. The study introduced the concept of an electron force, distinct from the traditional high-temperature conditions associated with dislocation annihilation. The influence of electron force on dislocation movement was corroborated through in-situ transmission electron microscopy experiments, highlighting the unexpected phenomenon of dislocation regeneration under electric current conditions. The detailed analysis of electron force direction and its impact on slip systems provided insights into the mechanisms governing dislocation behavior, distinguishing the experimental findings from those arising solely due to elevated temperatures. The study sheds light on the complex interdependence of electron force, dislocation movement, and local Joule heating effects in the context of single-crystal superalloys [19].

Moreover, according to the previous research studies, the joule heating or the electric current heat generation, is also a most significant effect in electroplasticty. Unlike conventional heating treatments that demand prolonged exposure at specific temperatures, electropulsing achieves a fine-grain microstructure rapidly, challenging its classification as merely a conventional heating process [20]. Hui SONG et al. [21] notes that electropulsing, characterized by its non-equilibrium nature and exceptionally high heating rate (approximately 10^6 °C/s), induces significant overheating during solid-state phase transformations in orthorhombic Ti_2AlNb-based alloys sheet. This overheating, coupled with the enhanced nucleation rate facilitated by electropulsing itself, contributes to the observed rapid microstructural changes. Electric current, as per the research, influences phase transition dynamics through mechanisms related to changes in current configuration based on the electric conductivity of the new phase and the host medium. The study recorded a substantial temperature rise on the specimen surface, reaching 630 K, accompanied by observed phase transformation and recrystallization phenomena that

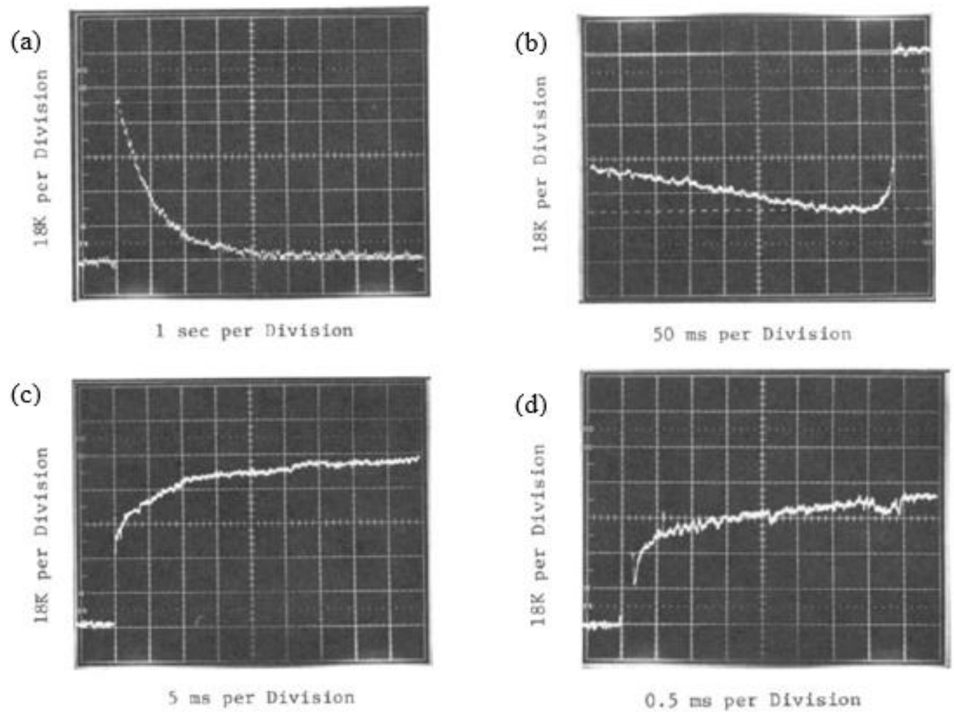

Figure 2.4: Temperature rise ΔT due to the pulse current measured on various time scales: (a) 1s per division, (b) 50ms per division, (c) 5ms per division and (d) 0.5ms per division [22].

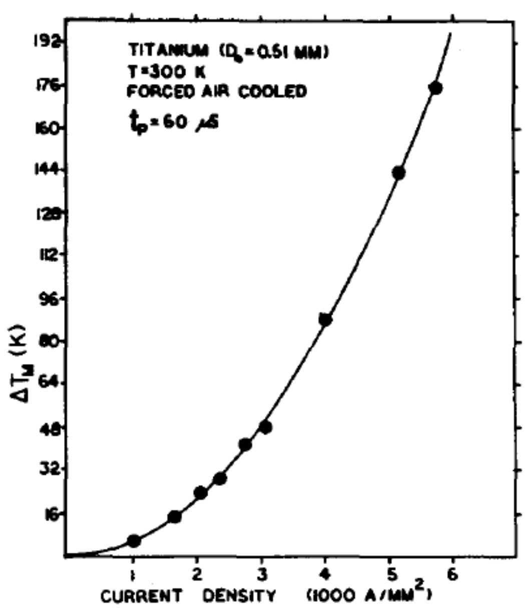

Figure 2.5: Maximum temperature rise ΔT_m versus current density for d.c. current pulses in the elastic region of a Ti polycrystalline specimen. Continuous curve represents calculated value; data points are experimental values [22].

subsequently influence stress-strain behavior [21]. Moreover, in alignment with the investigations conducted by A.F. Sperecher et al. [22], this inquiry into the electrothermal treatment of a titanium wire specimen has provided significant insights into the corresponding thermal dynamics. Within the domain of electroplasticity, a comprehensive exploration of the electro thermal process is crucial for understanding key phenomena. Drawing from the insightful research conducted by A.F. Spetier et al. [22], an in-depth analysis of temperature-time profiles, as portrayed in Figures 2.4 (a) to 4d, offers valuable insights. The study's findings highlight a significant ~6 ms delay in reaching peak temperature, ascribed to the inherent thermocouple response delay—a factor of pivotal importance in unraveling the nuances of the electroplasticity process. The subsequent temperature stabilization, lasting 50-100 ms and documented in the records, underscores the controlled and quasi-steady-state nature inherent in electroplasticity. This study is elucidating the exponential cooling trend, with the specimen returning to room temperature within 3-4 seconds, thereby emphasizing the influence of response times on recorded thermal profiles. Moreover, the comparison between measured and calculated values in Figure 2.5, considering Joule heating and surface heat loss, reveals a notable concordance, enriching the quantitative precision of the investigation. Notably, their records [22] include a calculated maximum temperature rise of 137 K for a current pulse of ~5000 A/mm^2 and a 50 µs duration, further enhancing the understanding of the Joule heating effect within the electroplasticity framework.

In the context of elucidating the de-pinning of dislocations by paramagnetic obstacles, it is imperative to delve into the intricate mechanisms governing the energy dynamics of dislocation bonds with these entities. The spin multiplicity of the radical pairs formed by the orbitals of dislocations and paramagnetic obstacles plays a pivotal role in determining their interaction. The radical pairs can exist in either singlet or triplet spin states, each associated with significantly different binding energies. The application of a magnetic field induces transitions between these states, creating an additional population of triplet states characterized by lower binding energies than their singlet counterparts. This magnetic-induced transition facilitates the de-pinning of dislocations from obstacles, consequently amplifying the plasticity of the material in a magnetic field. This mechanism not only elucidates the fundamental aspects of the magnetoplastic effect but also extends its explanatory power to comprehend key features of the electroplastic effect. The understanding of spin-dependent transitions within dislocation–obstacle systems forms the basis for interpreting the intricate nature of both magnetoplastic and electroplastic phenomena [23]. Molatski et al [24] proposed a comprehensive magnetoplasticity-derived framework to explicate the electroplasticity (EP) phenomenon. The hypothesis posited that the magnetic field induced by the electric current in the conductor heightened the likelihood of dislocation de-pinning from paramagnetic obstacles. In accordance with this postulation, the stress drop ($\Delta\sigma_{EP}$) in a metallic wire undergoing electroplastic deformation was suggested to be directly proportional to the square of the current density (j^2) as follows.

$$\Delta\sigma_{EP} = \frac{\sigma_m j^2 r^2}{4H_o^2} \tag{2}$$

Where, r is the radius of the wire, σ_m is the mechanical stress without electric current

effects, and H_o represents the characteristic magnetic field at which the efficient de-pinning of the dislocations from paramagnetic obstacles takes place. Molotskii [24] asserted that the stress drop arising from this magnetoplastic mechanism exhibited satisfactory concordance with experimental data obtained from certain face-centered cubic (FCC) metals, specifically copper (Cu) and aluminum (Al).

Grain boundary sliding or grain rotation induced by applied electric pulses during the elongation of metal workpieces represents another critical mechanism contributing to the enhancement of metal ductility. This phenomenon facilitates the promotion of dislocation motion while impeding the onset of work hardening effects. The presence of irregular atomic structures at grain boundaries leads to electron entrapment, resulting in elevated electrical resistance compared to the grain interior [25]. Consequently, this charge imbalance weakens atomic bonding strength at grain boundaries, facilitating grain rotation or sliding. As neighboring grains align their slip planes, dislocations traverse across grains, thereby augmenting the plasticity of the metal. Moon et al. [26] investigated this phenomenon in his study focusing on the commercial aluminum 5052-H32 alloy. The reduction in atomic bonding strength induced by electric current has been quantitatively characterized through the introduction of effective temperature, comprising the virtual temperature increase resulting from charge imbalance and the actual measured temperature. Furthermore, electroplastic deformation observed under electric current has been elucidated through finite element (FE) simulations incorporating the concept of effective temperature. Experimental validation of the athermal effect on atomic bonding strength attenuation has been achieved by measuring the elastic modulus under electric current. Collectively, these findings support the explanation of electroplastic phenomena as stemming from the weakening of atomic bonding near defects due to charge imbalance induced by electric current.

Despite over fifty years of experimental and theoretical investigation into electroplasticity, the understanding of electroplasticity theory remains in its nascent stages of development. Previous studies have predominantly adopted a phenomenological approach or focused on particular facets of electroplasticity deformation, without fundamentally challenging the underlying physics and mechanisms governing this phenomenon. While various electroplasticity theories have been proposed, each offering insights from different perspectives, a comprehensive theory that fully elucidates the intricacies of electroplasticity remains elusive to date.

2.5 Electricity assisted manufacturing

Electric currents applied to a metal naturally result in an increase in the metal's temperature due to Joule heating, regardless of the magnitude of the temperature rise. The thermal and athemal effects of continuous electric currents have been investigated by comparing the outcomes of electrically-assisted forming, where electric currents were applied to metals during deformation, with those of conventional methods such as oven heating or hot working at temperatures equal to or higher than those applied during electrically-assisted forming. Perkins et al. [27] revealed that even at lower temperatures, the stress reduction during electrically-assisted compression of aluminum, copper, iron, and titanium-based alloys was markedly higher than that achieved through conventional compression at elevated temperatures. Additionally, Dzialo et al. [28] found that the temperature increase observed during electrically-assisted compression of copper alloys was lower than that during hot working processes at the same stress reduction level. Ross et al. [29] identified isolatable effects of electricity, including Joule heating, kinetic energy (associated with dislocation movement), and retained stress-strain energy, while noting that higher material resistivity led to a more pronounced electroplastic effect. Salandro et al. [30] hypothesized that electric currents during deformation generated both heating and deformation energy and proposed a quantified electroplastic effect coefficient to differentiate between thermal and athermal effects of the electric current. Furthermore, it has been suggested that threshold current density values exist to induce a noticeable electroplastic effect on materials. Perkins et al. [27] reported that such a threshold was not achieved for the copper-based alloy evaluated in their study.

Electricity Assisted Manufacturing processes primarily pertain to bulk deformation and sheet-metal forming. Additionally, joining processes and material-removal processes are regarded as potential applications within manufacturing operations.

Ross et al. (29) documented a notable improvement in the forgeability of Ti6Al4V alloy under the influence of continuous electric current. C.D. Lang [31] et al. conducted compression tests on three M50 bearing steel, revealing the advantages of Electricity Assisted Manufacturing (EAM). They determined threshold current densities for each material and observed significant reductions in strain, with up to 50% improvement. Application of current increased springback, potentially due to heightened hardness near compression ends. These findings highlight the potential of EAM in enhancing manufacturing processes for bearing steels. The schematic representation of the Electricity Assisted forging process is depicted in Figure 2.6.

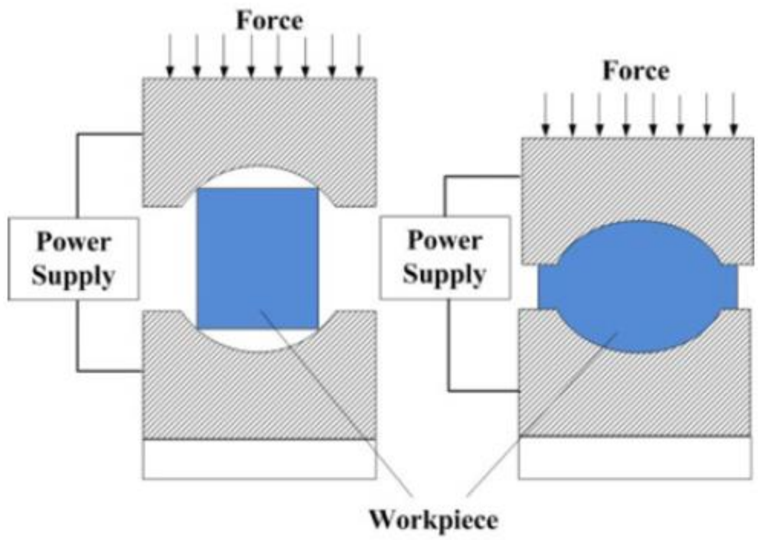

Figure 2.6: Schematic diagram of electricity assisted forging process [32].

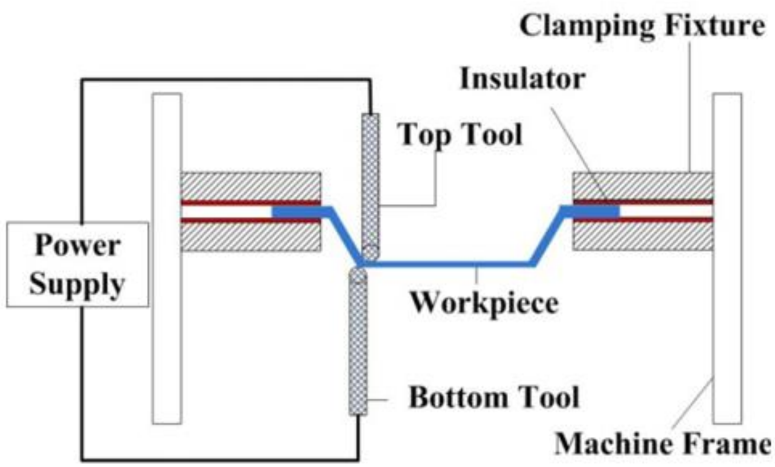

Figure 2.7: schematic of the electricity assisted incremental forming process [39]

Concerning the Electricity Assisted (EA) rolling process, Xu et al. [33] observed a significant reduction in the rolling force of magnesium AZ31 alloy, coupled with notable improvements in its deformation characteristics, while maintaining satisfactory surface quality at ambient temperature. Similarly, Lu et al. [34] reported decreased rolling forces and enhanced deformation for Bi2223/Ag. Additionally, EA rolling of magnesium AZ91 alloy exhibited a transition from brittle to dimple fracture at a 35% pass reduction compared to conventional warm rolling. Moreover, NiTiNb [35] and TiNi [36] alloys were successfully rolled using EA rolling at lower temperatures or without intermediate annealing, contrasting with traditional hot rolling methods. Furthermore, Tang et al. (37) posited that the elevation in temperature did not exert a substantial influence on the alterations observed in the mechanical properties, resistivity, and surface quality of austenitic stainless steel during the electro-chemical assisted (EA) drawing process. Conversely, Stashenko et al. (38) emphasized that the EA drawing process has the potential to diminish the production cycle duration and product expenses owing to the reduction in drawing force and augmentation in drawing velocity.

Moreover, Asghar et al. (39) demonstrated the successful formation of a titanium alloy through the utilization of an Electrically Assisted (EA) double-side incremental forming process, as depicted in Figure 2.7. This approach involved the application of pulsed electric current to the tool, which significantly enhanced the forming capabilities of incremental forming processes, potentially enabling the fabrication of exotic materials. Specifically, Ti6Al4V, known to require temperatures between 900-930°C for conventional forming, was effectively formed at a substantially lower temperature of 47°C through the application of pulsed electric current at the tool-sheet interface. This innovative technique resulted in reduced force requirements and minimized shape distortion compared to conventional methods. Furthermore, the use of electrically-assisted tools facilitated the localization of current conduction, thereby maximizing formability through electroplasticity.

An electrically-assisted pressure welding process (EAPW) was suggested by Xu et al. [40]. EAPW was found to significantly reduce the pressure welding force and improve bond strength under a continuous electric current. For instance, in the warm pressure weld process, SS316L was not bonded at 75°C even with a high welding force. At the same temperature, SS316L could typically be welded using EAPW at a current density of 20 A/mm^2. Both athermal and thermal effects were argued to contribute to the EAPW process. Additionally, the bond area was significantly increased from 89.4 to 278.6 μm. Furthermore, an electricity assisted metal cutting process was proposed by Baranov et al.

[41]. This study was conducted to investigate the relative change in drilling speed by utilizing pieces of copper, steel, duralumin, and cast iron under a pulsed electric current.

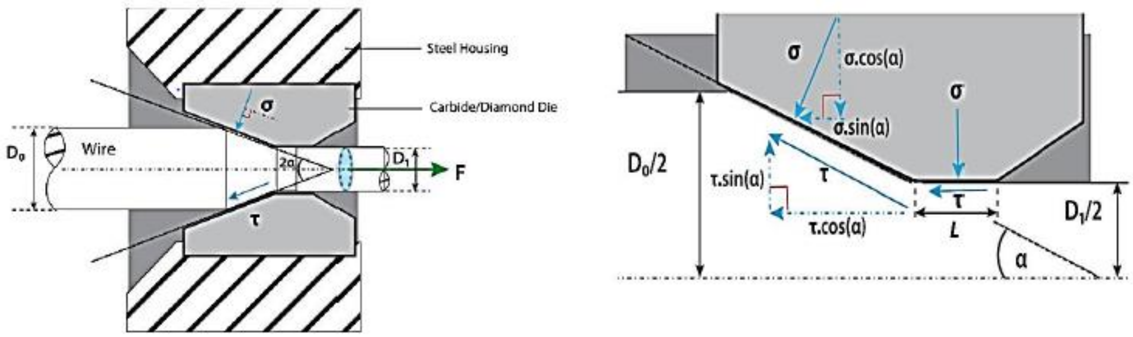

Figure 2.8: Schematic of a drawn wire of initial diameter D0 being pulled by Force F, with die exerting a subsequent normal stress σ and shear stress τ on the wire, α is the die half angle and L is the length of the die bearing [42].

A reduction in both friction force (by 25-30%) and processing time (by 10-12%) was observed compared to conventional methods. Additionally, it was noted that chips produced from steel in the absence of current were fragile and fine. Nonetheless, continuous chips were observed in EA cutting processes.

When consider about the wire drawing process (figure 2.8), the stresses experienced by a wire during the drawing process at the die can be minimized to shear and normal stresses developed at the wire-die interface due to the drawing force exerted. The minimum drawing force necessary for wire deformation depends on die surface friction, metal deformation resistance, and the die's semi-angle (α) [42]. As drawing force directly influences power consumption in wire rod production, decreasing it can lead to cost reductions. Techniques like hydrodynamic drawing, which augment lubrication consumption within the die by approximately 20%, have been shown to lower drawing forces by 15–30% and result in roughly 17% electricity cost savings [42].

A research has been conducted by Salandro et al. [43] and it aimed at disentangling the thermal and non-thermal effects of pulsed current by conducting a comparative analysis of tensile test results between conventionally heated specimens and those exposed to pulsed current. It was observed that specimens subjected to prolonged pulsed conditions demonstrated enhanced formability. The overarching findings of the study indicated a reduction in flow stress and an augmentation in elongation prior to fracture. Several different deformation mechanisms for workpieces under pulsed current have been reported by various researchers. The microstructure of Mg-3Al-1Zn alloy subjected to electropulse treatment for 7 seconds after cold-rolling was investigated by Li et al., who compared it with furnace annealing at a minimum temperature of 200 °C. They observed a significant increase in recrystallization with electropulse treatment, attributed to the enhanced nucleation rate of non-basal-oriented nuclei [44]. Liang and Lin observed an increase in dislocation density and improved formability in materials subjected to electropulse stress during non-deformation tests [45]. Delobelle et al. confirmed that electropulse treatment altered the material properties of NiTi shape memory alloys, with the extent of change dependent on the duration of the pulses [46].

Although numerous studies have been conducted to analyze the influence of electroplasticity on the mechanical properties of metals and alloys, there remains a gap in the literature regarding its impact on plain carbon steels with varying carbon contents and with various pulse frequencies. Therefore, this research aims to investigate the effects of electroplasticity on selected plain carbon steel samples under different pulse frequencies and effective currents.

3 METHODOLOGY

3.1 Preparation of plain carbon steel samples

Ensuring consistent experimental results requires careful selection of plain carbon steel samples. To optimize the specimens' response to pulsed electric current, they were selected, fabricated, and heat-treated according to established best practices. This section details the criteria for material selection, fabrication techniques, and the normalization heat treatment applied to ensure reliable and reproducible results.

3.1.1 Selection of plain carbon steel samples

Mild steel samples were obtained in strip form from various local vendors. Upon acquisition, the samples underwent Spark Emission Compositional Analysis to ascertain their chemical composition. This method, commonly utilized in metallurgical research [47], enables precise and rapid identification of alloying elements, ensuring the material aligns with the specified low- and medium-carbon steel categories. Research indicates that carbon content plays a crucial role in grain refinement, phase transformations, and mechanical properties [48]. Additionally, studies have emphasized the impact of impurities such as sulfur and phosphorus on the mechanical behavior of steel under different thermal and electrical conditions [49]. Therefore, compositional analysis was necessary to ensure material uniformity before further processing.

Tables 3.1 present the pertinent chemical compositions of the steel types utilized in the experiment. Additionally, the specimens exhibited minimal quantities of other inclusions.

Table 3.1: Chemical compositions of selected plain carbon steel strips

Sample No	**C (wt.%)**	**Mn (wt.%) (<1.65)**	**Si (wt.%) (<0.6)**	**Cu (wt.%) (<0.6)**	**S (wt.%)**	**Cr (wt.%)**	**Fe (wt.%)**
1	0.09	0.50	0.01	0.005	0.016	0.003	99.20
2	0.39	0.71	0.23	0.131	0.104	0.087	98.10

3.1.2 Fabrication of tensile specimens

The fabrication of dumbbell-shaped tensile specimens was performed according to methods outlined in the preliminary study [47], utilizing CNC cutting and water jet cutting techniques. These methods were selected for their precision and effectiveness in minimizing heat-affected zones (HAZ), which could otherwise impact the material's mechanical properties [50]. CNC cutting offers high accuracy in specimen shaping, while water jet cutting ensures a thermally neutral process, preventing microstructural alterations from localized heating. The design, depicted in figure 3.1, was generated using SolidWorks software. The tensile specimen was not prepared in accordance with ASTM E8/E8M 16a standard, with the specific aim of maximizing current density within the sample. Research indicates that decreasing the cross-sectional area of a tensile specimen significantly increases current density, resulting in notable microstructural changes [51-53]. To ensure uniform electrical and thermal exposure, a dumbbell-shaped specimen was fabricated with a minimum cross-sectional area of 6 mm² and a consistent thickness of 3 mm.

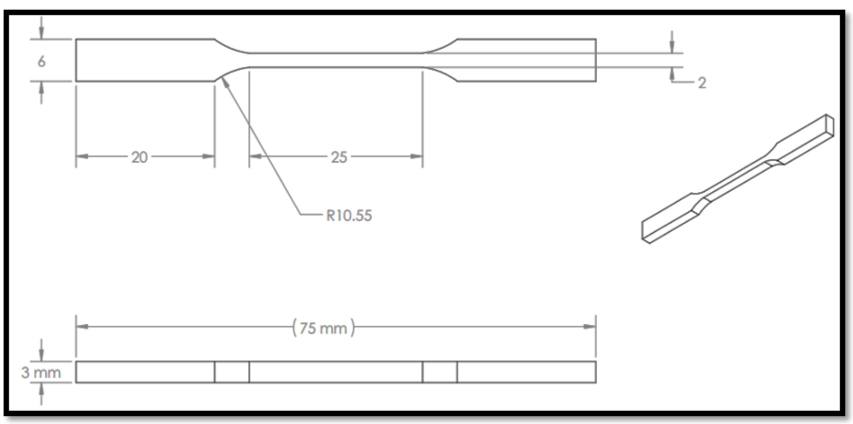

Figure 3.1: Detailed design of the specimen

3.1.3 Normalizing of fabricated specimens

Following fabrication, all tensile specimens underwent normalization heat treatment to eliminate residual stresses introduced during machining and to achieve a uniform, homogenized grain structure. Normalization is a well-established metallurgical process known for enhancing the mechanical properties of steel by refining grain structure and mitigating internal defects. During normalization, the specimens were heated to just above the upper critical temperature to ensure complete austenitization. The critical temperature range for low and medium carbon steels is well-established in the literature, typically between 850°C and 950°C. In this study, the samples were heated to 900°C and held at this temperature for one hour to achieve complete microstructural transformation. Research suggests that maintaining this holding time is crucial for obtaining a uniform grain structure and dissolving any coarse carbides present in the steel [54].

The specimens were subsequently air-cooled in a normal atmospheric environment (room temperature: 30°C), as depicted in Figure 3.2. Literature indicates that air cooling, in contrast to furnace cooling, fosters the formation of a fine ferritic-pearlitic structure, thereby enhancing both ductility and strength [55]. This controlled cooling method was selected to minimize hardness variations and prevent excessive grain growth, which could otherwise result in embrittlement and adversely affect the steel's response to pulsed electric current treatments.

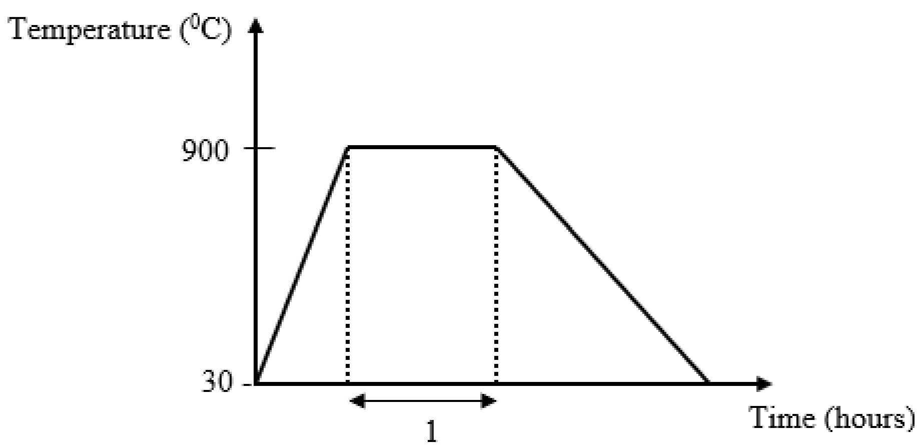

Figure 3.2: Normalization heat treatment cycle

3.2 Experimental setup

Various methodologies have been utilized to investigate the effects of pulsed electric currents on the mechanical properties of metals. Previous studies have shown that applying electric pulses can alter material characteristics, including ductility, yield stress, and microstructural evolution [47]. In related research, welding transformers with modified secondary windings have been effectively employed to generate controlled current amplitudes, demonstrating their capability in delivering precise pulse parameters [48].

3.2.1 Different Methods Used to Set Up Pulse Current Generators

- PEKURIS PVP 2KV1KA Pulse Power Supply

Ichsan et al. [56] utilized the PEKURIS PVP 2KV1KA pulse power supply to study the influence of pulsed electric current on the mechanical behavior of an Ep Mg alloy. In this setup, the positive electrode was connected to the bottom side of a clamping system, and a uniaxial tensile test was conducted under different temperature conditions. Three distinct pulse frequencies (200 Hz, 600 Hz, and 1000 Hz) were applied while maintaining a fixed pulse width of 150 microseconds. To regulate global temperature conditions and minimize the influence of Joule heating, a PID controller was implemented. This approach ensured precise control over peak current densities and isolated the pulsed current effect from thermal effects.

- 4000 FN DC Power Supply (CHANT, Zibo, China)

Xu et al. [51] employed a 4000 FN DC power supply to generate a pulsed current for tensile testing of an AZ80 Mg alloy. The pulsed current was periodically applied to the specimen, with a pulse duration of 100 microseconds and a period of 1000 microseconds. The experimental setup ensured that the average current density remained nearly constant at 2.5 A/mm^2 before the onset of necking, allowing for the assessment of material response under controlled electrical loading conditions.

- Vadal SP-1000U Power Supply with Programmable Pulse Controller

  N.T. Thien et al. [57] conducted quasi-static tensile tests using a Vadal SP-1000U power supply equipped with a programmable pulse controller. The pulsed current was applied to the specimen during tensile deformation with a pulse duration of 0.36 seconds. Different current densities (50, 60, 72, 86, and 103 A/mm²) were used, and the electric current was delivered at a specified engineering strain. This method allowed for precise control over the pulsed current application and facilitated the investigation of its effects on tensile behavior.

Each of these methodologies employs distinct pulse current generator setups tailored to specific experimental requirements. The PEKURIS PVP 2KV1KA system incorporates frequency variation with temperature control, while the 4000 FN DC power supply focuses on periodic current application with a constant density. The Vadal SP-1000U system, on the other hand, integrates programmable control for single-pulse applications at varying current densities. These variations highlight the importance of selecting an appropriate pulse current generator based on the desired testing conditions and research objectives. The preliminary study of this research by N. Hendeniya et al. [48] utilized a step-down transformer with an adjustable pulse controller for tensile testing under pulsed current conditions. A modified transformer with 1.5 kVA power was used to achieve the required current by altering the winding configuration. The secondary coil was redesigned to contain six windings, each consisting of 23 copper wires, while the primary coil remained unchanged. The experimental parameters included a current amplitude of 64 A, a pulse width of 10 seconds, and a pulse frequency of 20 Hz. Their study observed the electroplasticity effect in low-carbon steel containing 0.2% C. Building upon this research, the current study aims to investigate the electroplasticity effect under higher current amplitudes and lower pulse frequencies.

3.2.2 Modification of transformer

- Selection of current amplitudes for the study

When select a pulse current to get the electroplasticity effect, following factors should be considered.

- To achieve high current density without putting large amount of heat pulse current is pulse current is preferable.
- Pulse width should be minimum to reduce the joule heating. (~100 μs)
- To enhance the effect of electrons on electroplasticity application of high current density is recommended. ($10A/mm^2$- $10^5A/mm^2$) [58]

Two different methods were explored to modify the pulse current generator, and the third method was ultimately selected for further experimentation and continuation of the research.

- Experimental Approaches for Pulse Current Generator Setup

Method 1:

Based on the preliminary study, the selected current densities, pulse width, and pulse periods are as follows: the pulse duration was set to 10 ms using a DC current, with pulse periods of 15 ms, 20 ms, and 30 ms. The chosen current densities were 10, 20, and 30 A/mm^2. By maintaining a constant current supply duration of 10 ms, the off-time periods were varied at 5 ms, 10 ms, and 20 ms.

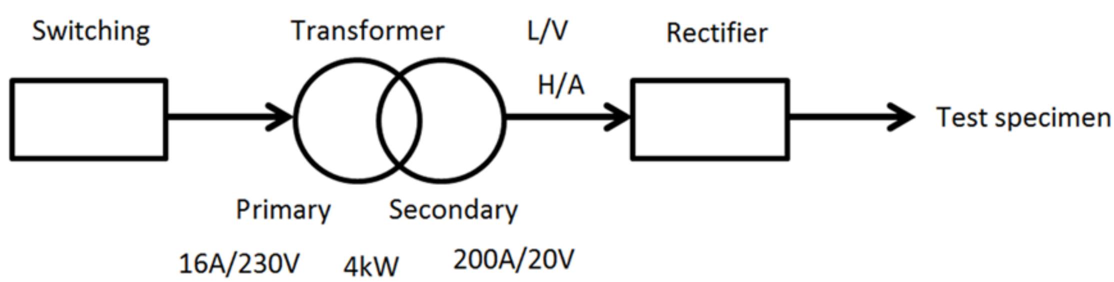

Figure 3.3 Schematic Diagram of the Pulse Current Generator Circuit

To achieve this, a square wave signal generated by an oscillator and an uninterruptible power supply (UPS) was intended to be passed through a switching device with a timer, allowing selective blocking of the current as required. The modified current was then directed through a 4-kW step-down transformer, with the negative portion blocked using a half-wave rectifier (figure 3.3).

However, implementing a timer to block specific portions of the current proved to be highly challenging. During preliminary testing on a project board to verify the feasibility of the setup, several diodes were damaged. Given the limitations of available laboratory facilities and the allocated project budget, Method 1 was determined to be impractical. Consequently, an alternative approach (Method 2) was pursued.

Method 2:

A welding transformer, initially rated at 2kW power, was underwent modification to achieve the desired current amplitudes by altering the windings of the secondary coil while maintaining the windings of the primary coil unchanged. This modification facilitated the generation of discrete current amplitudes. A timer with a minimum resolution of 0.05s was employed with this setup to get electric pulses with distinct pulse frequencies. Figure 3.4 depicts the configuration of this apparatus and the table 3.2 shows the selected effective currents and the pulse frequencies. An oscilloscope (YOKOGAWA DLM2024) was used to measure the amplitude of the peak current and the pulse duration. RMS values of the selected currents were 636.4 A and 777.8 A. By keeping the pulse on-time as constant as 10 ms, the pulse off-time was varied from 600 to 1800 ms by 300 to get five different pulse frequencies. In the experimental set-up, one gripping end was carefully insulated to eliminate the current flow through the testing machine. An infrared thermal camera (testo 870) was used to record the temperature variation of the specimens during the tensile test. A set of three specimens from each condition were used to check the repeatability of the test. Average engineering stress versus engineering strain graphs were plotted for each condition (table 3.3) by using the data obtained from the in-built tensile behavior tracking software of the universal tensile testing machine (WAW-1000E Universal Testing Machine) (figure 3.5).

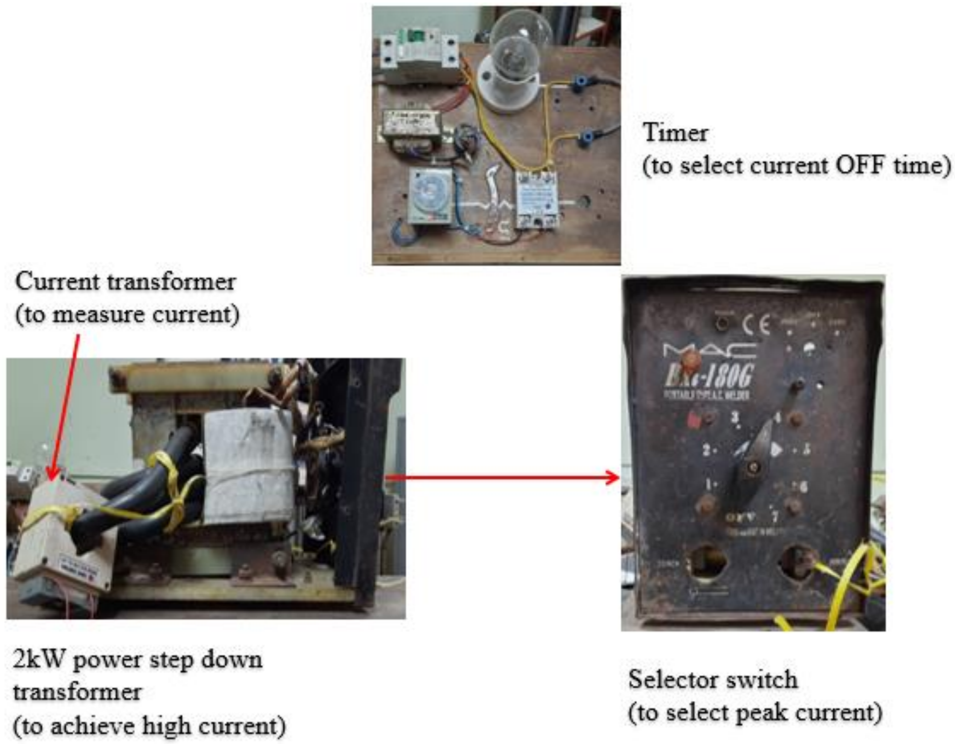

Figure 3.4: The apparatus of current supply

Table 3.2: Details of the selected pulse frequencies and current amplitudes

Effective current (A)	Pulse ON time period (ms)	Pulse OFF time period (ms)	Pulse frequency (Hz)
636.4	10	600	1.64
		900	1.10
777.8		1200	0.83
		1500	0.66
		1800	0.55

Table 3.3: Tensile testing conditions

Carbon content (wt.%)	**Pulse frequency (Hz)**	**Effective current (A)**
0.09 0.39	0.55	636.4 777.8
	0.66	
	0.83	
	1.10	
	1.64	
	0	0

Figure 3.5: Universal tensile testing machine

3.2.3 Yield stress and UTS measurements

The average engineering stress versus engineering strain curves were generated for each experimental condition utilizing data collected through the integrated tensile behavior tracking software of the universal tensile testing apparatus. For each condition, a series of three specimens were tested to derive an average stress-strain profile. Subsequently, the average yield stress and ultimate tensile strength (UTS) were determined from these average stress-strain curves for every experimental condition.

3.2.4 Microstructural analysis

Microstructures of the as-annealed samples, at the fracture surface and the strained surface of the fractured specimens were observed using the metallurgical microscope (MEIJI). According to the ASTM E3 standard, sample preparation for microstructural analysis involved several sequential steps. Initially, the test piece was carefully separated from the damaged area using a precision cutter. Subsequently, the surface was subjected gradual grinding utilizing a series of emery papers. Following this, the sample was meticulously polished using a polisher to achieve a smooth surface. After polishing, the sample was washed with water and thoroughly dried. Etching of the dried sample was performed using a Nital solution (2% HNO_3: 98%C_2H_5OH v/v%). Then, the sample was rinsed with water to eliminate any excess etchant effectively. Finally, the prepared sample was examined under an optical microscope, focusing on specific points as illustrated in the figure 3.6. Microstructural images were taken for each sample under 100x magnification in the purpose of comparing the grain sizes.

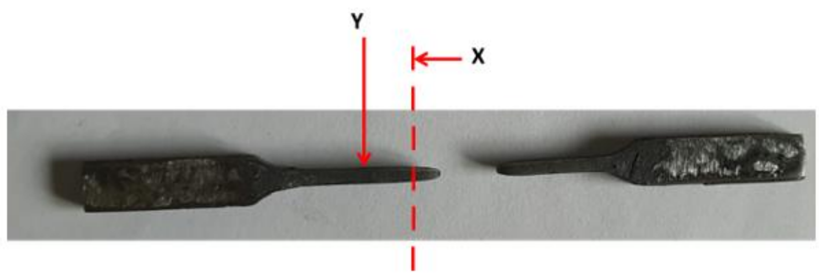

Figure 3.6: Points of microstructural Analysis. X – Normal to the elongated direction, Y – Along the elongated direction

3.2.5 Morphology analysis

The examination of fracture surface morphology was conducted employing a scanning electron microscope (SEM) (Carl Zeiss EVO 18 research model). A specimen measuring 10mm in length, inclusive of the fracture surface, was prepared for analysis.

3.2.6 Ductility calculation

The diminishment in area subsequent to a tensile test serves as a quantitative indicator of a material's ductility. To examine the influence of electrical current on the ductility of the material, the reduction in area was assessed concerning samples tested both with and without current. The lengths of two sides of the fractured surface were measured using a Vernier caliper, and this process was repeated for both pieces of the sample, tested under without current and with current for both carbon compositions and all the conditions. The aggregated measurements facilitated the computation of the average area of the fractured samples, enabling a comparative analysis of the reduction in area and its relative proportionate decline.

3.2.7 Strain energy calculation for the sample shows highest ductility

Energy absorbed by the sample during the deformation was obtained by calculation the area under the average stress strain curve.

The area under the curve was computed using a Python script, which integrated the data points from the true stress vs. true strain graph. The strain at fracture was determined by identifying the strain value at the point of final fracture on the average true stress vs. true strain curve, which was derived from the tensile test experiment.

Strain energy and toughness were calculated only for the samples that exhibited the highest ductility among all tested samples. The selected current parameters for these calculations were an effective current of 777.8 A and a pulse frequency of 0.83 Hz. These calculations were performed for both 0.09 wt.% C and 0.39 wt.% C samples.

3.2.8 FEA for analyzing the thermal and mechanical behavior of the samples

3.2.8.1 Selection of the boundary conditions

Temperature built-up inside the test piece and induced magnetic field due to the current during the tensile were investigated using COMSOL Multi-physics software. All relevant material properties were sourced from established research papers and material property references [58-61]. The ‘normal’ mesh sized was selected for the component (figure 3.7).

Assumptions included zero prescribed displacements in the y and z directions, a room temperature of 30°C, a Poisson's ratio of 0.28, adherence to the Ludwik equation for the plastic region of the stress-strain curve, and negligible heat transfer to the surroundings. Additionally, parameters such as yield strength, maximum displacement, hardening

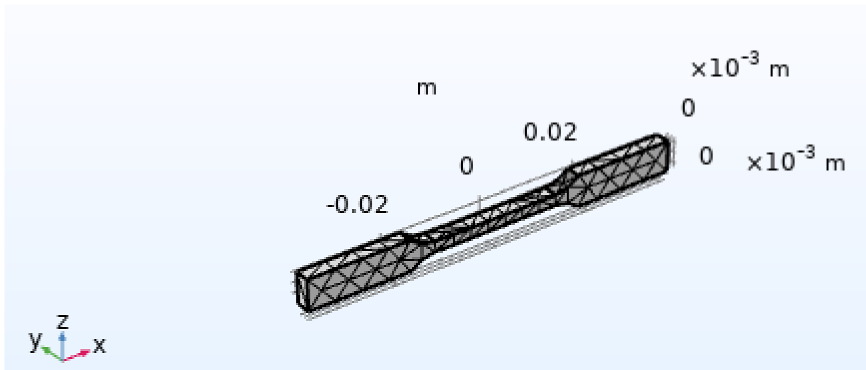

Figure 3.7: Mesh of the component (gauge length -25 mm, thickness – 3 mm, width – 2 mm)

exponent, and strength coefficient corresponding to each condition were obtained from experimental data.

3.2.8.2 Selection of the Physics interfaces

Electric current and electrical circuit physics interfaces were incorporated to apply relevant electrical pulses to the specimen. The interface for heat transfer in solids was implemented to simulate the Joule heating effect. Furthermore, the solid mechanics physics interface was employed to analyze the tensile behavior, with prescribed displacement in the x direction derived from experimental results, while displacements in the y and z directions were set to zero. The study also involved the examination of magnetic flux density resulting from the induced magnetic field during testing. This was achieved by integrating the magnetic field physics interface into the material model. Additionally, multiphysics coupling was established to link the aforementioned physics interfaces, incorporating electromagnetic heating, thermal expansion, and magnetostriction effects.

4 RESULTS AND DISCUSSION

The selection of pulse electric current over continuous current was motivated by the goal of minimizing excessive heat generation on the workpiece. The softening caused by "Joule Heating" would have hindered the understanding of the effect of electron wind flow and its interaction with dislocations on the electroplasticity effect. This phenomenon had the tendency to promote the formability of metals by facilitating the movement of dislocations in the sample. Therefore, the usage of a higher pulsating current accelerated the movement of dislocations, consequently delaying dislocation pile-up and improving the formability of the workpiece.

4.1 Analysis of the thermal and mechanical properties from the experimental results

4.1.1 Temperature variation of the samples during the tensile test

Applying an electric field along the metal, induces a force on each electron due to the interaction between the field and the electron's electric charge. Consequently, the moving electrons gain additional kinetic energy as a result of this force acting upon them, in addition to the kinetic energy they already possess. Similar to the process of heating a portion of the metal, the electrons promptly transfer their extra energy to the atoms of the metal, leading to an overall increase in the metal's temperature.

If the amplitude of the current is higher, more energy is input into the metal. In this experiment, higher pulsed currents (636.4 and 777.8 A) with fixed pulse ON time (10 ms) and varying pulse OFF times are utilized. As the pulsating frequency increases, a greater amount of energy is input into the metal during a specific time period, leading to a more even distribution of energy throughout the metal and an increase in its temperature during the electricity-assisted tensile test. Consequently, a gradual increment in the surface temperature of the test piece was observed with the pulse frequency (figure 4.1 and 4.2).

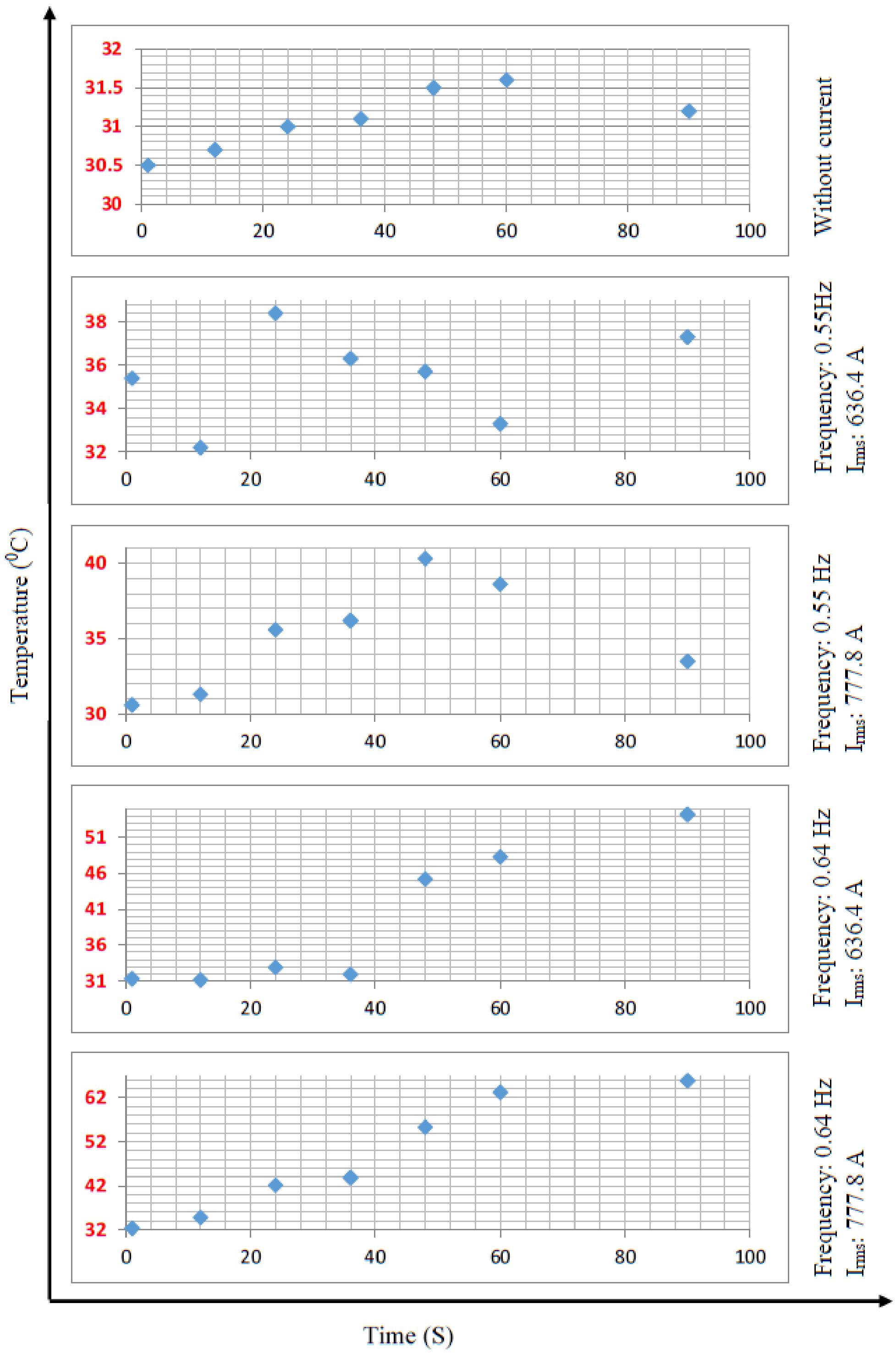

Figure 4.1: Temporal variation of the specimen's (contain 0.09 wt.%C) surface temperature - recorded at randomly selected time intervals during the tensile test

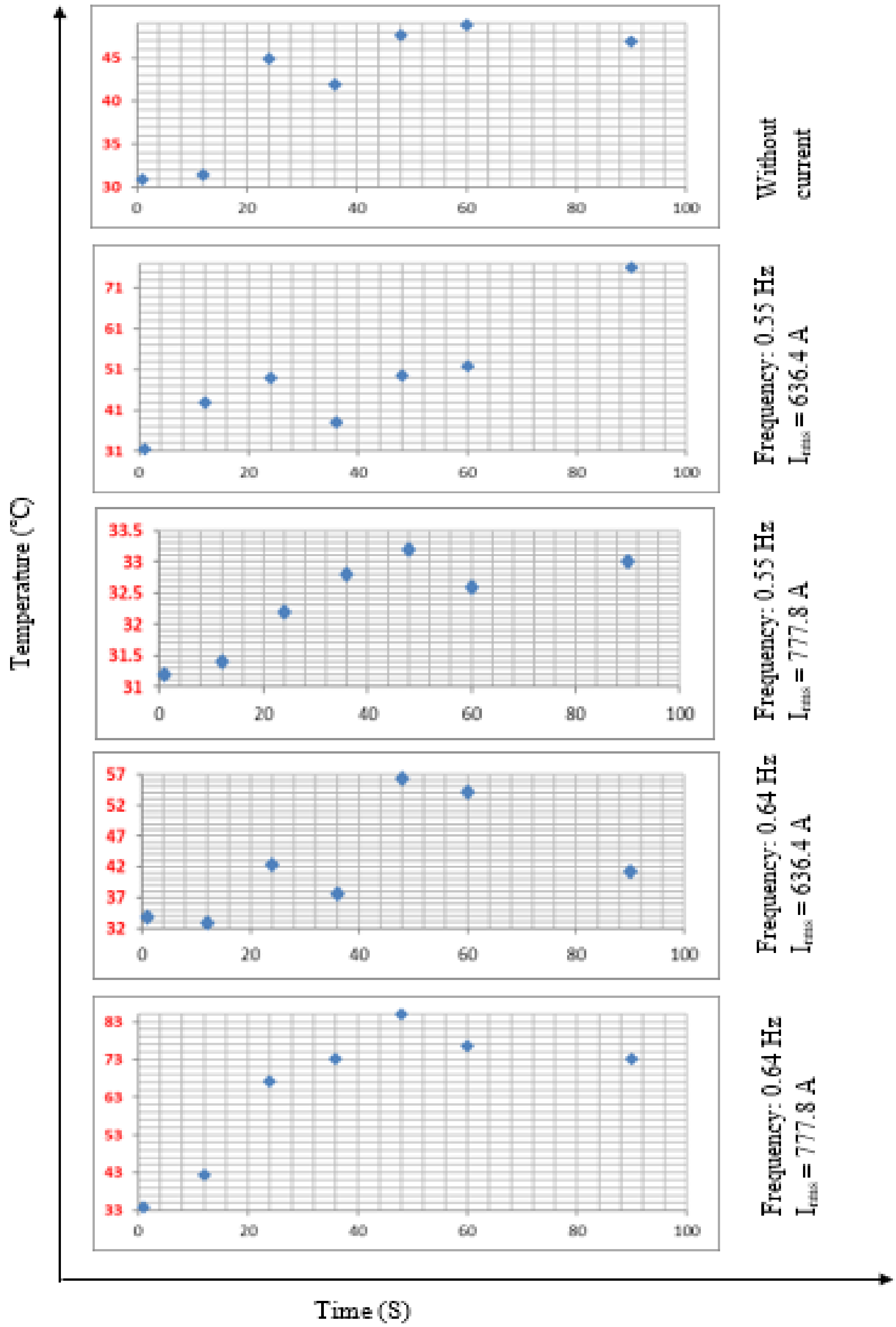

Figure 4.2: Temporal variation of the specimen's (contain 0.39 wt.%C) surface temperature - recorded at randomly selected time intervals during the tensile test

(a)

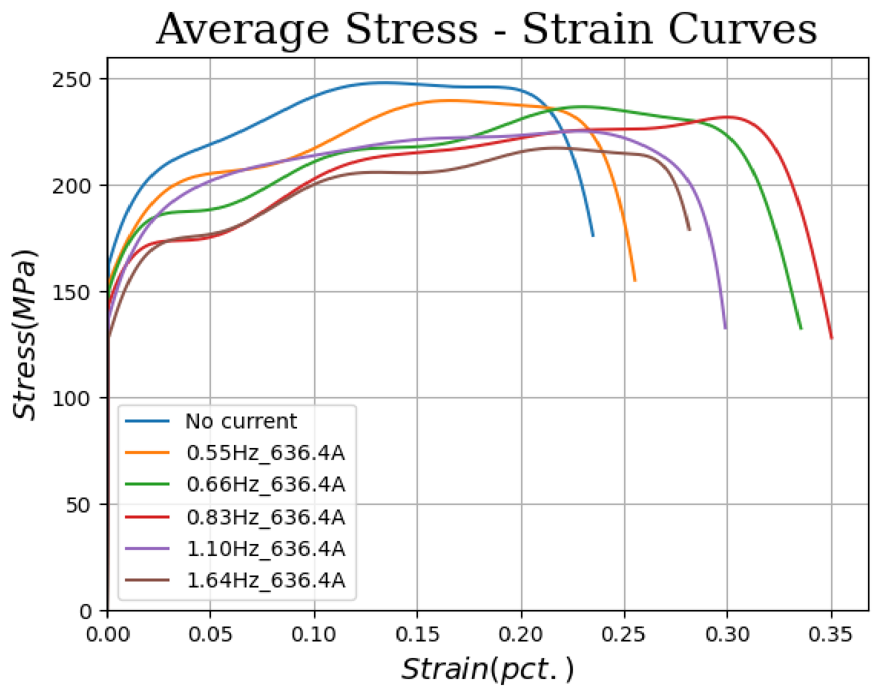

(b)

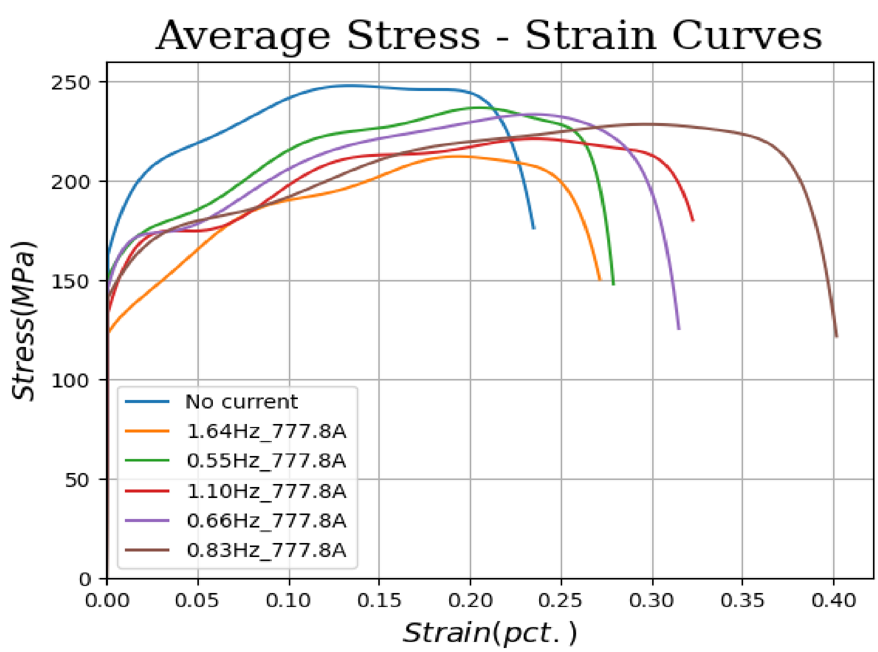

Figure 4.3: Average stress – strain curves obtained for the samples contain 0.09 wt.% C (a) When I_{rms} = 636.4 A (b) When I_{rms} = 777. 8 A

(a)

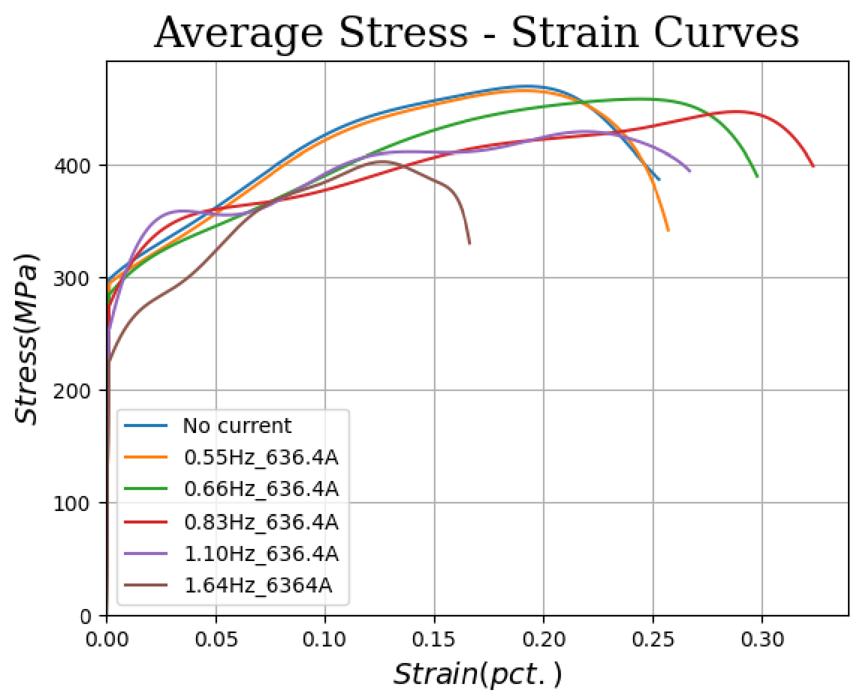

(b)

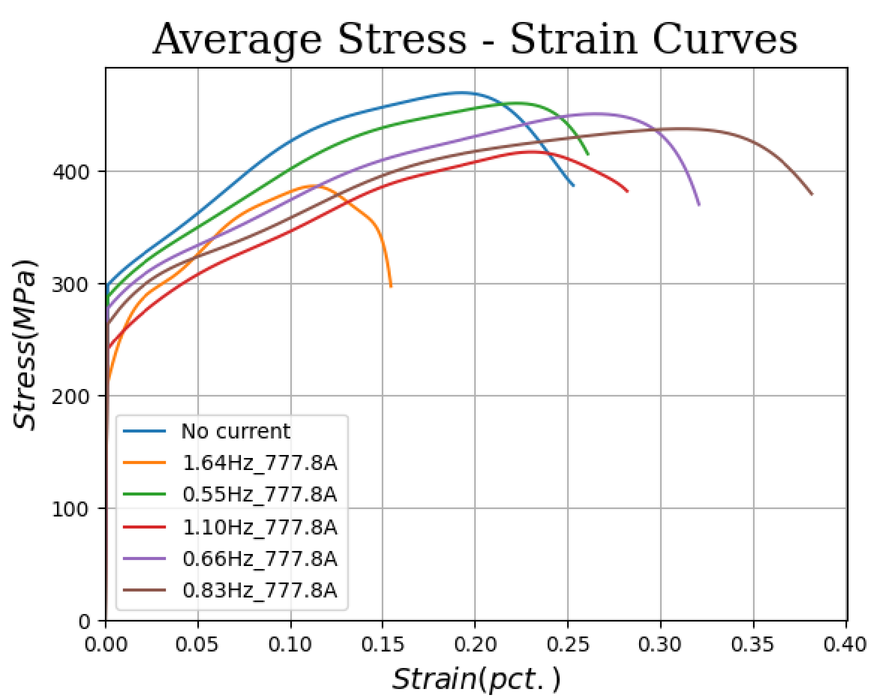

Figure 4.4: Average stress – strain curves obtained for the samples contain 0.39 wt.% C (a) When I_{rms} = 636.4 A (b) When I_{rms} = 777. 8 A

Average stress strain curves for each and every condition (figure 4.3 (a), (b) and figure 4.4 (a), (b)) were plotted using a python program. Upon examination of the stress-strain graphs obtained under various conditions, it is noted that the average stress-strain graph derived without the application of electric current surpasses the other graphs obtained under different current amplitudes and pulse frequencies. Additionally, for both carbon contents (0.09 wt.% C and 0.39 wt.% C), the curves obtained from tensile tests conducted without electricity exhibit a less fracture strain. Moreover, for both carbon contents, the samples subjected to an effective current of 777.8 A and a pulse frequency of 0.83 Hz demonstrate the maximum fracture strain. Despite an increase in strain at fracture from a pulse frequency of 0.55 to 0.83 Hz, a reduction in fracture strain is observed upon exceeding 0.83 Hz for both carbon steels. Notably, samples containing 0.39 wt.% carbon display a fracture strain even lower than that observed under normal conditions. The detailed explanation for this behavior is provided in the ductility variation section.

In both plain carbon steel samples with 0.09wt.%C and 0.39wt.%C, a progressive decrease in yield stress (Figure 4.5) and UTS (Figure 4.6) was observed as the pulse frequency and effective current were increased. Thermal softening of the material was potentially induced by the increase in the rms value of current, which determines the average energy input [62], before reaching its original yield stress level. As a result, an increase in the rms value of the current led to a reduction in the material's yield stress, initiating plastic deformation. Moreover, a more uniform distribution of energy throughout the material, brought about by an increase in pulse frequency, contributed to a gradual reduction in yield stress. Tensile testing of the specimen under the conditions of the highest pulse frequency (1.64 Hz) and effective current (777.8 A) resulted in a maximum surface temperature of 84.8 °C, conclusively demonstrating that no phase transformation occurred due to heat build-up. Therefore, the initial ferrite phase remained unchanged. Consequently, the observed improvement in formability can be solely attributed to the phenomenon of electroplasticity.

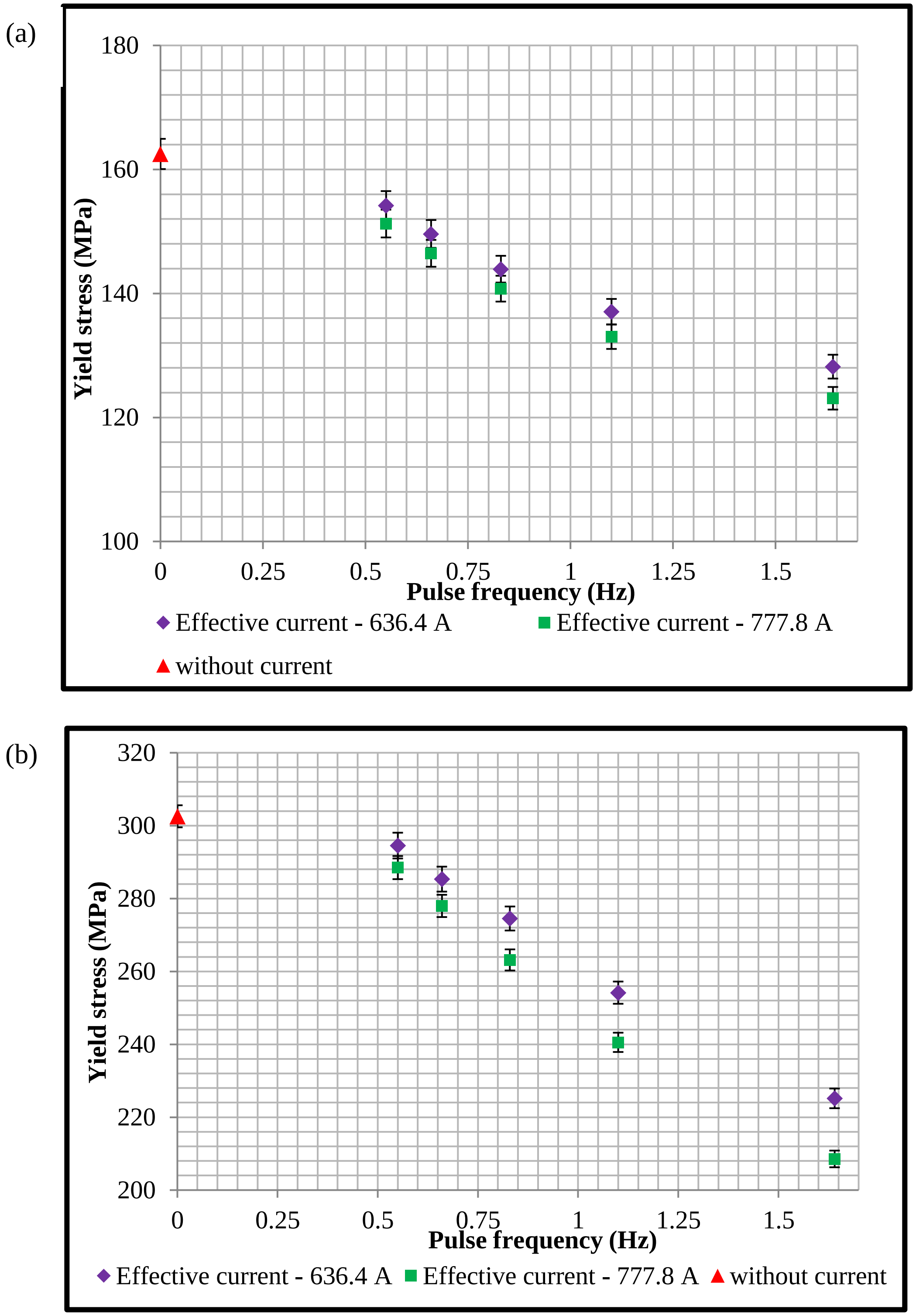

Figure 4.5: Yield stress variation with pulse frequency for the samples contain (a) 0.09 %wt. C (b) 0.39 wt.%C

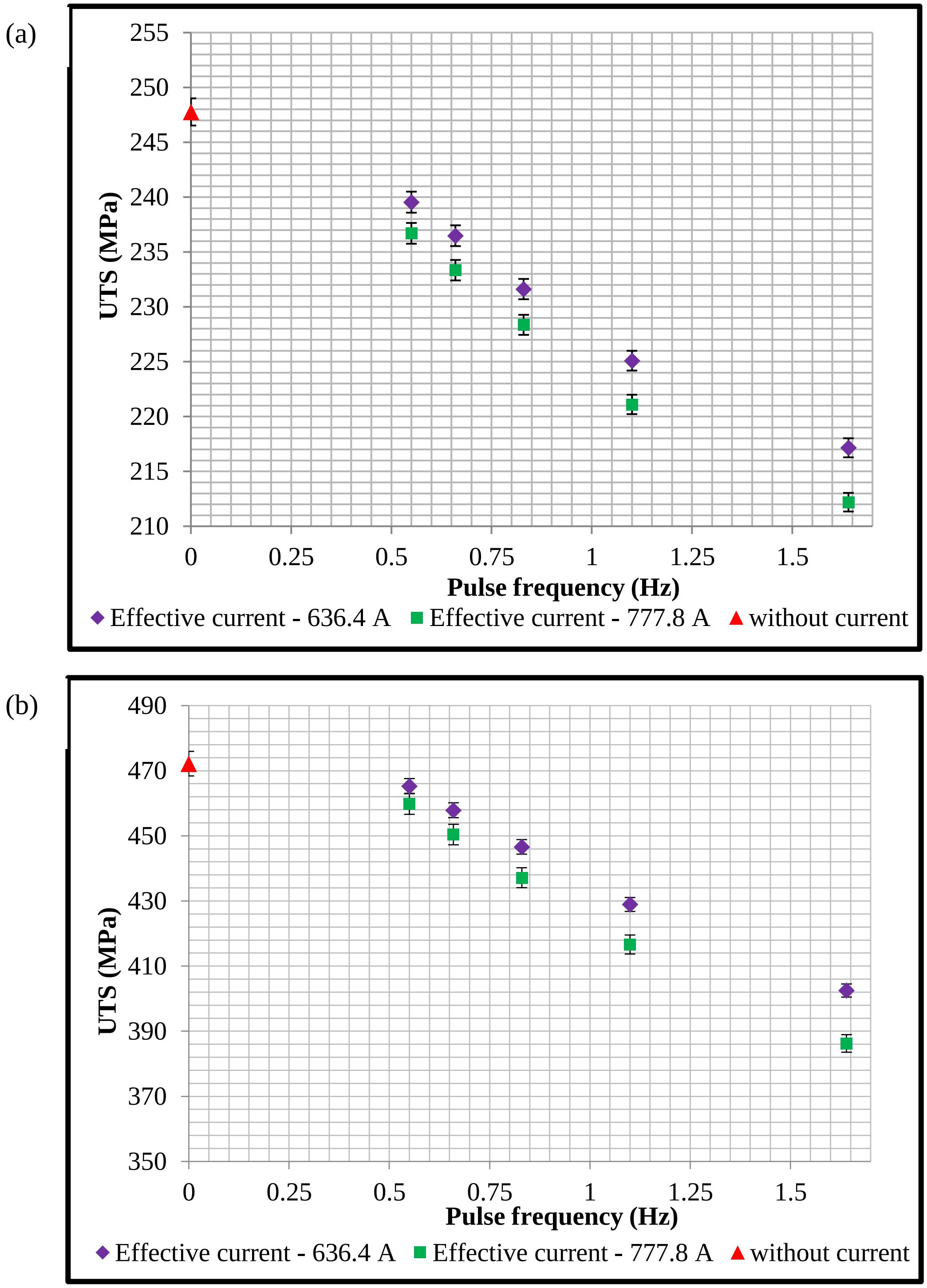

Figure 4.6: UTS variation with pulse frequency for the samples contain (a) 0.09 wt.% C (b) 0.39 wt.% C

Furthermore, the distribution of energy throughout the workpiece is influenced by the frequency of pulsating current, promoting dislocation motion. Uneven energy distribution inside the material occurred when the frequency of pulsing is lower, as the lower frequency resulted in a relatively long OFF-time period during which no energy is added to the workpiece. Consequently, this created a higher energy gradient between local areas, inhibiting dislocation movement and causing a relatively higher flow stress. Conversely, a high frequency of pulsating current led to even energy distribution throughout the material, facilitating uniform dislocation movement and reducing flow stress [63]. Consequently, yield stress varied with the current amplitude and frequency of pulsing. Given that plastic deformation in metals primarily occurs through dislocation movement, the effect of electroplasticity on dislocation generation and movement should be taken into account.

The sudden value of stress required to maintain the plastic deformation of a material is considered as the flow stress, and the reduction of flow stress with the applied pulse currents can be explained using the Taylor strengthening equation (equation 3) [48].

$$\sigma_f = \frac{\sigma b \mu}{M}\sqrt{\rho} \tag{3}$$

Where, σ is a dimensionless constant, b is the Burger's vector, μ is the shear modulus, M is the Schmid's factor and ρ is the dislocation density. Pulse current influences both the dislocation density and the Schmid's factor. Grains rotation can alter the Schmid's factor, directly affecting the flow stress. Grain boundaries, characterized by relatively large disorientation, exhibit high resistance to dislocation motion, and plastic strain leads to dislocation accumulation at these boundaries. Upon the application of an electric field, moving electrons encounter scattering at these defects, impeding their mobility. Consequently, an electric field imbalance arises at the grain boundaries, creating a driving force for grain rotation, thereby facilitating easier transmission of dislocation slip across the grain boundaries. The distribution of electric energy becomes more uniform as the pulse frequency increases, enhancing the ease of dislocation movement and resulting in easier softening. A.Rahnama and R.Qin observed rotation of crystals during electropulsing treatment at room temperature in duplex steel when the peak current density is 10.18 A/mm^2, pulse width 10 μs, and pulse frequency is 1 Hz. It has been demonstrated that crystal rotation occurs in directions that offer lower resistance to electric current flow [58,63].

Table 4.1 illustrates a discernible trend whereby incremental adjustments in effective current and pulse frequency correspond to a gradual reduction in both yield stress and ultimate tensile strength (UTS). Notably, the minimum yield stress is recorded at an effective current of 777.8 A and a pulse frequency of 1.64 Hz. This observation underscores the significance of current density and frequency as determinants influencing the impact of electric current pulses on material plasticity under ambient conditions, without concomitant thermal effects on either the materials or operational environment temperature.

Table 4.1: Percentage reduction of UTS and yield strength with pulse frequency

I_{rms} (A)	**Pulse frequency (Hz)**	**0.09 wt.% C**		**0.39 wt.% C**	
		UTS reduction (%)	**Yield stress reduction (%)**	**UTS reduction (%)**	**Yield stress reduction (%)**
636.4	0.55	3.32	5.11	0.83	1.35
	0.66	4.55	7.94	2.41	4.44
	0.83	6.52	11.44	4.81	8.05
	1.10	9.15	15.65	8.58	14.87
	1.64	12.36	21.11	14.21	24.58
777.8	0.55	4.47	6.91	1.99	3.37
	0.66	5.82	9.86	4.00	6.90
	0.83	7.83	13.37	6.83	11.86
	1.10	10.6	18.14	11.20	19.43
	1.64	14.36	24.25	17.67	30.15

4.1.2 Ductility variation

(a)

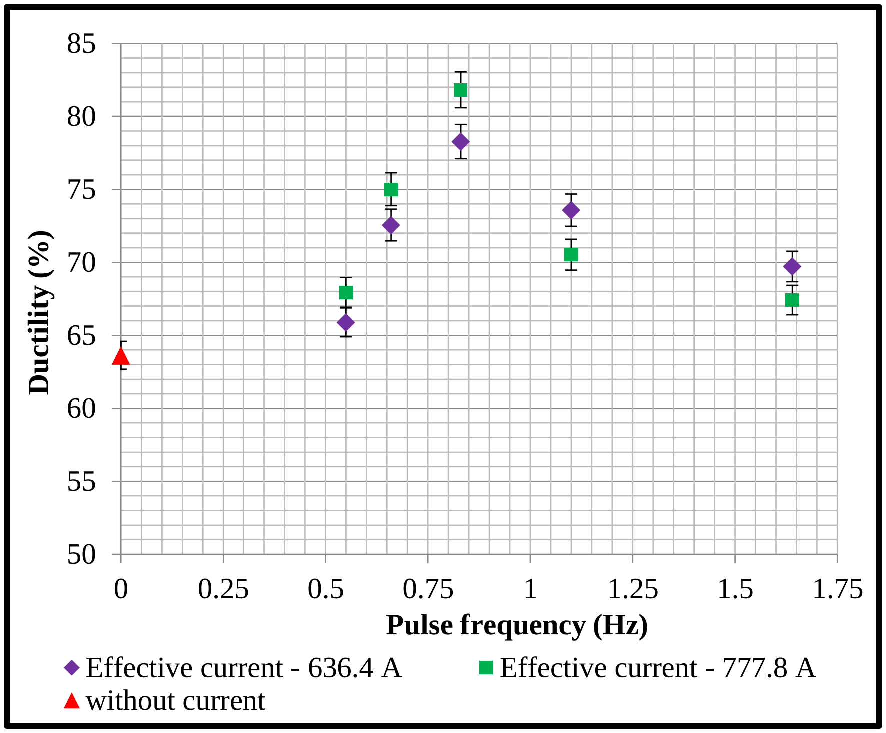

(b)

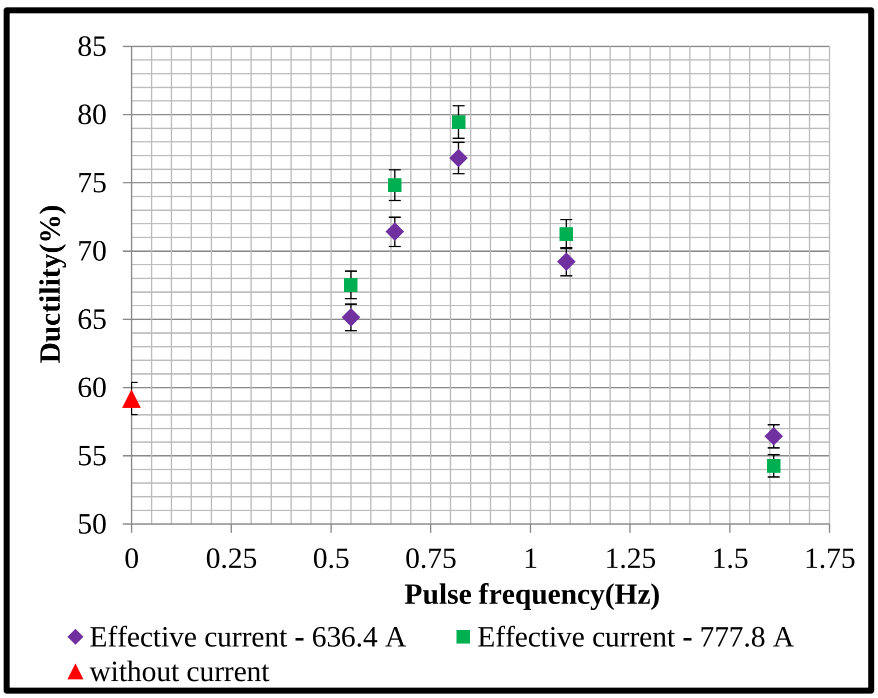

Figure 4.7: Ductility variation with pulse frequency (a) 0.09 wt.%C steel (b) 0.39 wt.%C steel

Ductility variations were assessed by analyzing the area reduction concerning pulsed frequency for both effective currents. An increasing trend in ductility was evident for plain carbon steel samples at both effective currents across a pulse frequency range of 0.55 Hz to 0.83 Hz (figure 4.7). This trend substantiates the favorable influence of electroplasticity on metal plasticity. Conversely, a subsequent rise in pulse frequency beyond 0.83 Hz (figure 4.7) for the aforementioned samples and currents led to a gradual decline in ductility. At relatively higher effective currents (636.4 A or 777.8 A) and pulse frequencies (1.10 Hz or 1.64 Hz), resulting in elevated electric energy input, localized heating within the material occurred. This localized heating may affect the thermal softening and facilitating increased plastic deformation due to enhanced dislocation motion. However, if the rate of dislocation generation/motion surpasses the rate at which dislocations reorganize or annihilate, accumulation of dislocation tangles, pile-ups, and other dislocation-related defects may occur. These defects can serve as stress concentration sites, potentially initiating cracks prematurely and reducing ductility. An additional hypothesized explanation for this phenomenon may attributed to the elevated electric energy input experienced during the material elongation phase of the tensile test. This heightened energy may induce increased atomic vibrations, potentially resonating with the material's natural frequencies. Consequently, such vibrations could lead to the rupture of atomic bonds, particularly in proximity to defect sites, ultimately culminating in material fracture at lower strain levels. The variation in fracture strain, inferred from stress-strain curves obtained for each pulse frequency under selected effective currents, further supports the observed ductility alterations. Additional insights into these phenomena can be gleaned through microstructural and morphological analyses of the fracture surfaces of the specimens.

4.1.3 Microstructural analysis

Table 4.2: Microstructural Analysis for the Samples contain 0.09 wt.% carbon

	Virgin sample	At fracture (X)	At surface (Y)
Without current	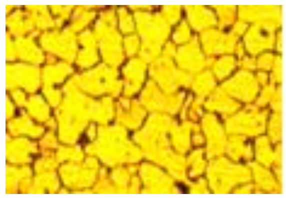	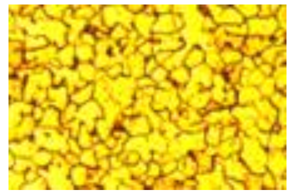	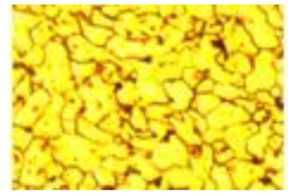
Frequency = 0.55 Hz Irms = 636.4 A	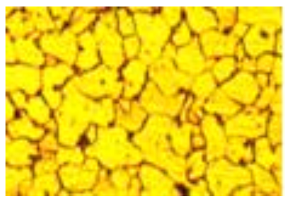	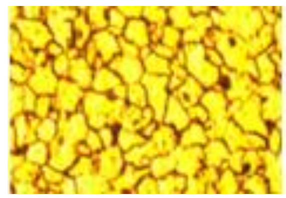	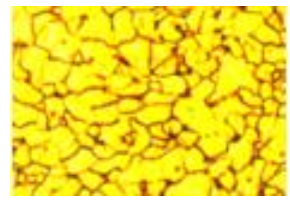
Frequency = 0.66 Hz Irms = 636.4 A	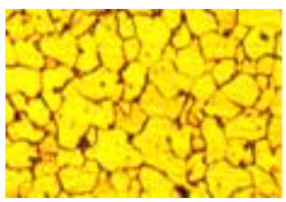	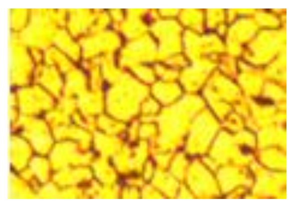	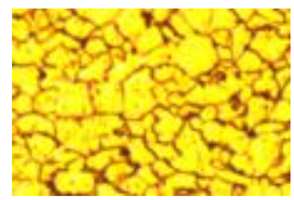
Frequency = 0.83 Hz Irms = 636.4 A	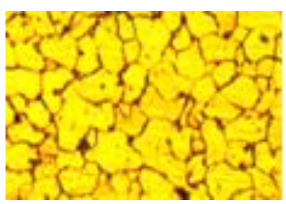	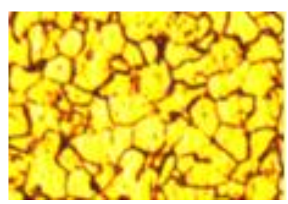	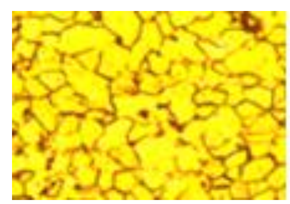
Frequency = 1.09 Hz Irms = 636.4 A		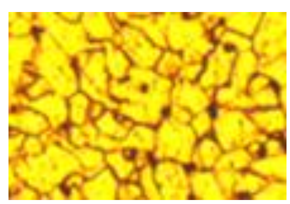	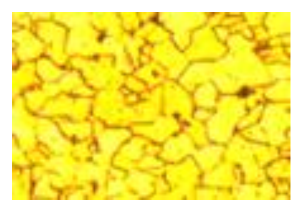
Frequency = 1.64 Hz Irms = 636.4 A		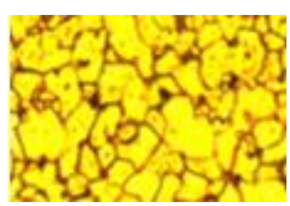	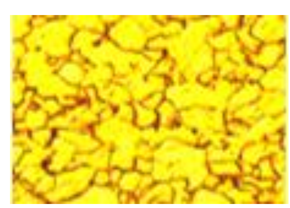

	Virgin sample	At fracture (X)	At surface (Y)
Without current	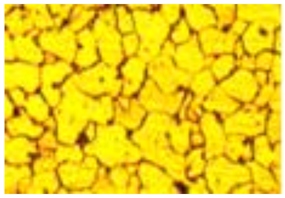	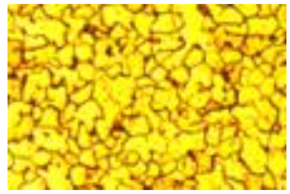	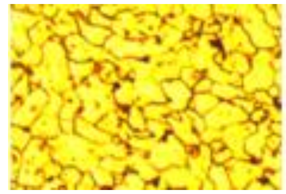
Frequency = 0.55 Hz Irms = 777.8 A	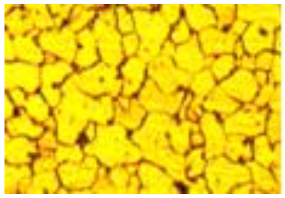	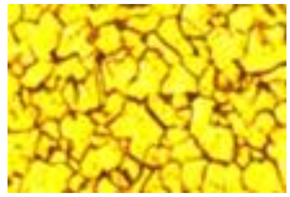	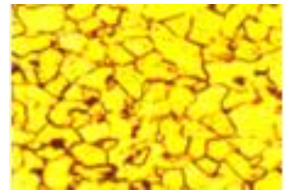
Frequency = 0.66 Hz Irms = 777.8 A	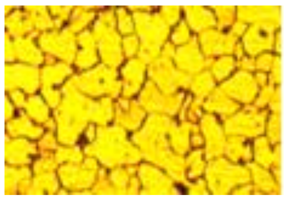	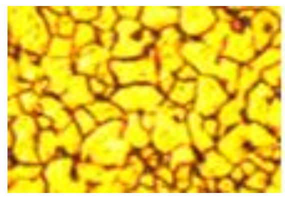	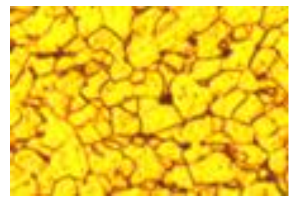
Frequency = 0.83 Hz Irms = 777.8 A	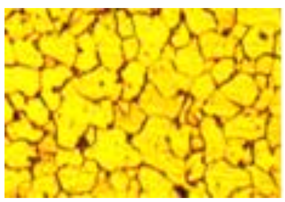	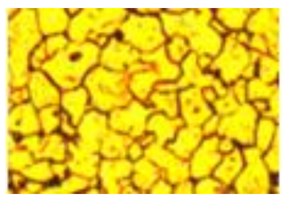	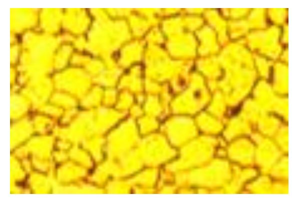
Frequency = 1.09 Hz Irms = 777.8 A	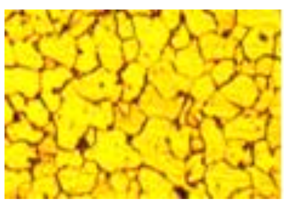	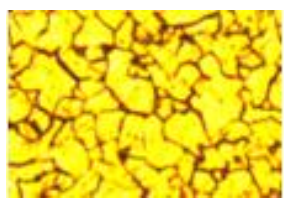	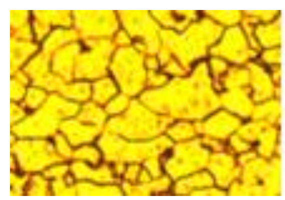
Frequency = 1.64 Hz Irms = 777.8 A	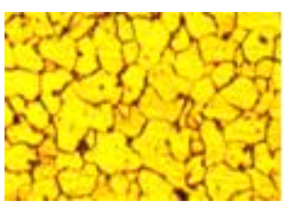	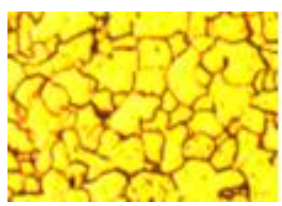	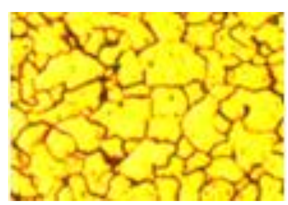

Table 4.3: Microstructural analysis for the samples contain 0.39 wt.% carbon

	Virgin sample	**At fracture (X)**	**At surface (Y)**
Without current	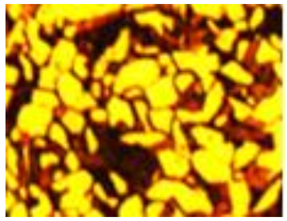	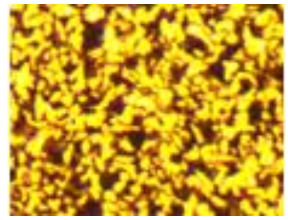	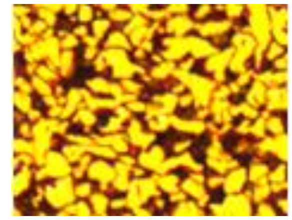
Frequency = 0.55 Hz Irms = 636.4 A	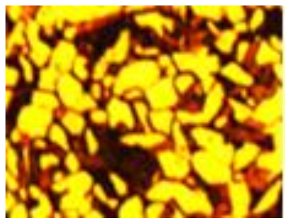	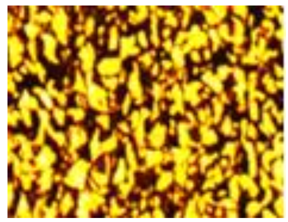	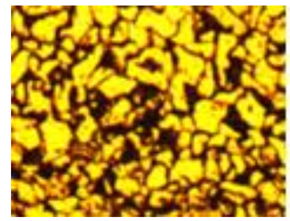
Frequency = 0.66 Hz Irms = 636.4 A	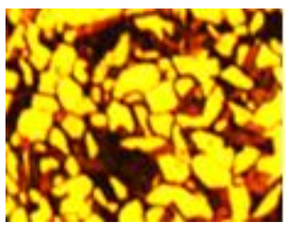	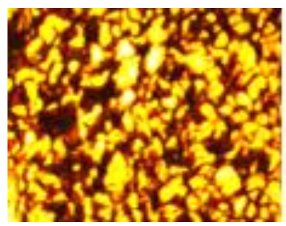	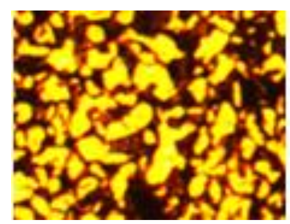
Frequency = 0.83 Hz Irms = 636.4 A	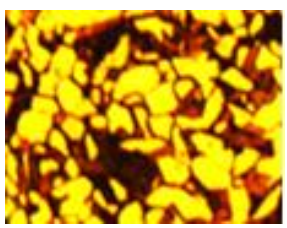	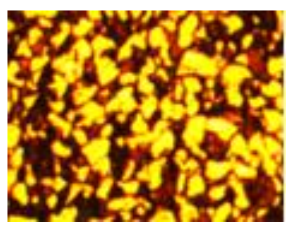	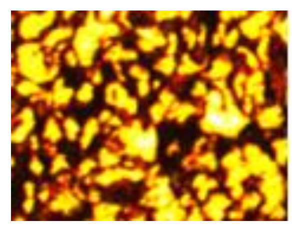
Frequency = 1.09 Hz Irms = 636.4 A	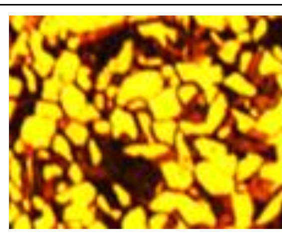	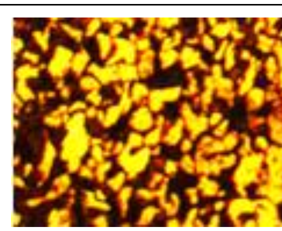	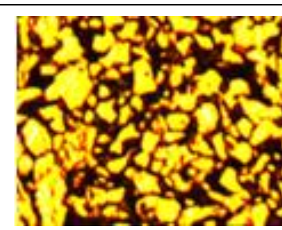
Frequency = 1.64 Hz Irms = 636.4 A	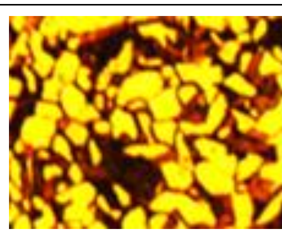	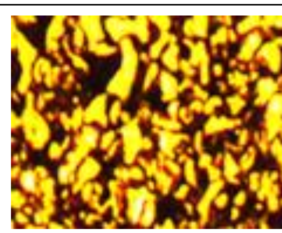	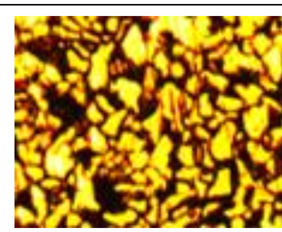

	Virgin sample	At fracture (X)	At surface (Y)
Without current	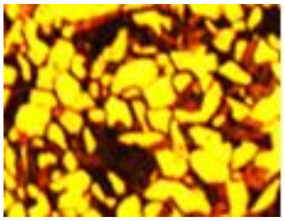	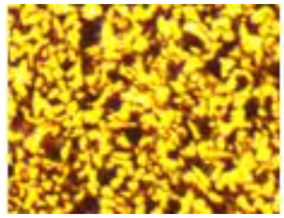	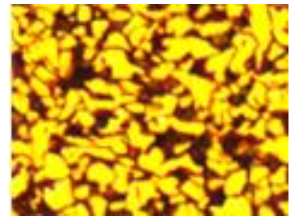
Frequency = 0.55 Hz Irms = 777.8 A	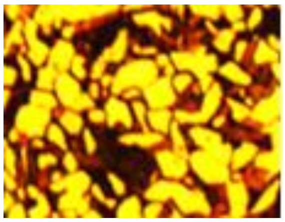	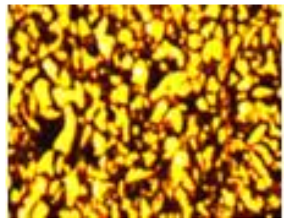	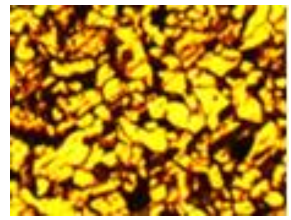
Frequency = 0.66 Hz Irms = 777.8 A	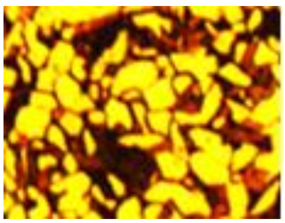	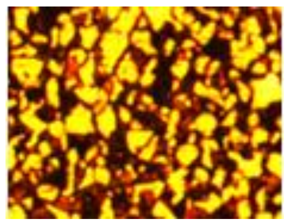	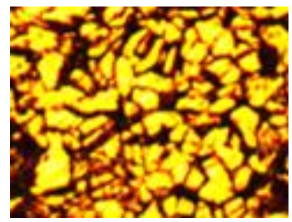
Frequency = 0.83 Hz Irms = 777.8 A	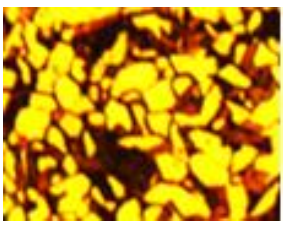	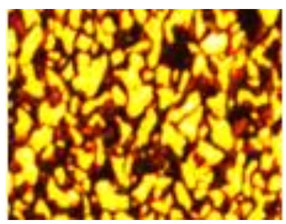	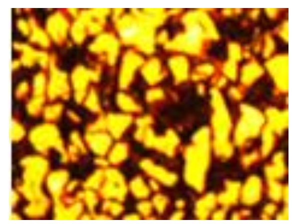
Frequency = 1.09 Hz Irms = 777.8 A	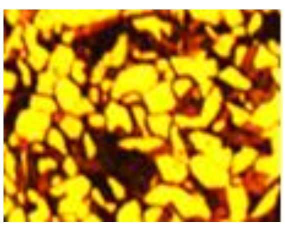	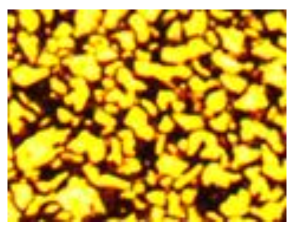	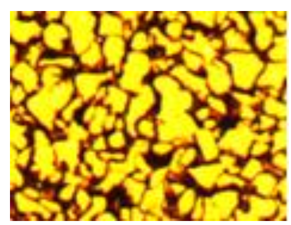
Frequency = 1.64 Hz Irms = 777.8 A	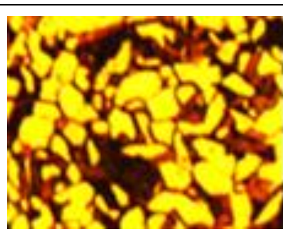	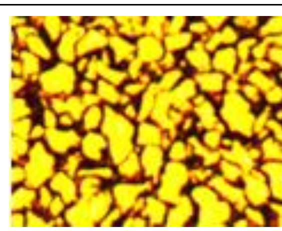	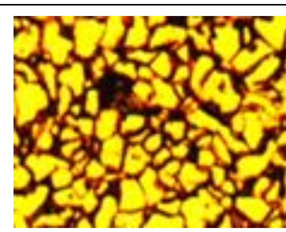

Table 4.4: Average grain size variation

Amplitude of effective current (A)	Pulse frequency (Hz)	Average grain size (mm)			
		0.09 wt.% C		0.39 wt.% C	
		At fracture point (x)	At surface (Y)	At fracture point (x)	At surface (Y)
0	0	0.0598	0.0595	0.0464	0.0597
636.4	0.55	0.0635	0.0651	0.0483	0.0602
	0.66	0.0642	0.0657	0.0485	0.0611
	0.83	0.0655	0.0660	0.0497	0.0618
	1.09	0.060	0.0672	0.0501	0.0625
	1.64	0.0768	0.0681	0.0526	0.0631
777.8	0.55	0.0641	0.0655	0.0553	0.0616
	0.66	0.0645	0.0659	0.0557	0.0623
	0.83	0.0658	0.0664	0.0568	0.0628
	1.09	0.0666	0.0669	0.0571	0.0632
	1.64	0.0772	0.0673	0.0579	0.0638
Virgin specimen		0.0855		0.0685	

Microstructures were analyzed across all test conditions employing a metallurgical microscope, with a focus on two distinctive surfaces (figure 3.6). One surface corresponds to the fractured plane, oriented perpendicular to the elongation axis, while the other surface is situated at a distance of 5 mm from the fracture point and aligned parallel to the elongation axis. Additionally, to provide a basis for comparison, the microstructure of the as-normalized specimens was assessed (table 4.2 and 4.3) . The average grain sizes were quantified using the ASTM-E112-10 method.

Upon examination of the grain structures on the fracture surfaces, both carbon steels showcased a decrease in average grain size post-tensile testing in the absence of pulsed current application. Specifically, the 0.09% carbon steel exhibited an average grain size of 0.0589 mm, while the 0.39% carbon steel exhibited 0.0464 mm (table 4.4), which were smaller compared to their respective non-deformed samples (normalized) with average grain sizes of 0.803 mm and 0.685 mm, respectively. Notably, samples subjected to electricity-assisted tensile testing displayed larger grain sizes compared to those tested without current. Higher pulse frequency (1.64 Hz) and effective current (777.8 A) resulted in significantly larger grain sizes for both 0.09% carbon steel (table 4.4) with an average size of 0.0702 mm and 0.39% carbon steel with an average size of 0.0579 mm. Conversely, lower pulse frequency (0.55 Hz) and effective current (636.4 A) led to relatively smaller grain sizes for both 0.09% carbon steel (0.0635 mm) and 0.39% carbon steel (0.0483 mm). Moreover, a progressive increase in average grain size was observed with other pulse frequencies (0.66 Hz, 0.83 Hz, and 1.10 Hz).

The reduction in grain size at the fracture surface, compared to the non-deformed (normalized) sample, is attributed to grain elongation during tensile testing and lateral contraction of grains due to Poisson's effect. The observed increase in grain sizes with pulse frequencies may be explained by the localized heating effect caused by the application of electric current pulses, resulting in elevated temperatures at higher localized deformation areas, promoting grain growth through the diffusion of atoms within the crystal lattice. Moreover, the electric current induces recrystallization, leading to the nucleation and growth of new grains. This recrystallization process involves the rearrangement and annihilation of dislocations, particularly in regions experiencing higher localized deformation or temperature. As a result, areas undergoing significant deformation or thermal effects during the testing exhibit larger grain sizes due to recrystallization.

Additionally, a similar trend to the one described above was observed in the variation of grain sizes on the surface of the sample located 5 mm away from the fracture point, aligned parallel to the elongation axis. The elongation of grains during tensile testing decreased with the increase in pulse frequency and effective current. Consequently, during tensile testing with relatively higher pulse frequency and effective current, a notable phenomenon emerged: the grain sizes at both surfaces approached those of the as-normalized sample. This suggests that deformation induced by the electroplasticity effect influences grain size, thereby enhancing plasticity. This effect is particularly evident in 0.09% carbon steel samples, as they contain a larger fraction of ferrite compared to 0.39% carbon steel.

4.1.4 Fracture surface morphology analysis

Table 4.5: Fracture surface morphology analysis for the samples contain 0.09 wt.% C

	Irms = 636.4 A	**Irms = 777.8 A**
Frequency = 0.55 Hz	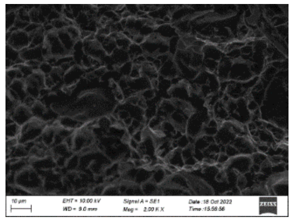	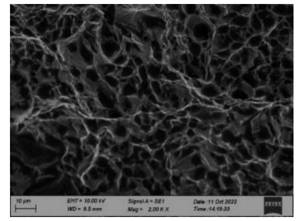
Frequency = 0.66 Hz	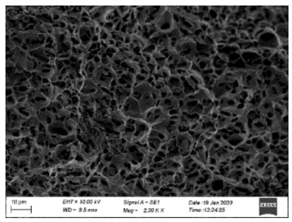	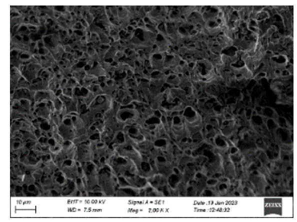
Frequency = 0.83 Hz	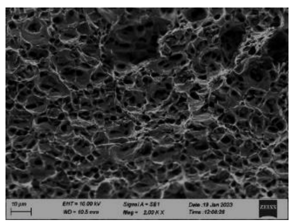	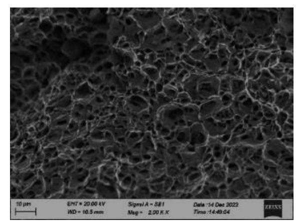
Frequency = 1.09 Hz	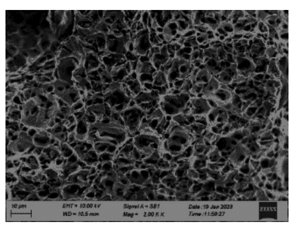	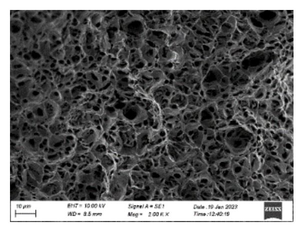
Frequency = 1.64 Hz Irms = 636.4 A	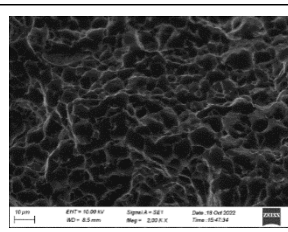	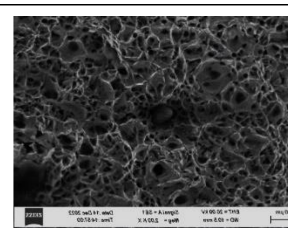
Without current	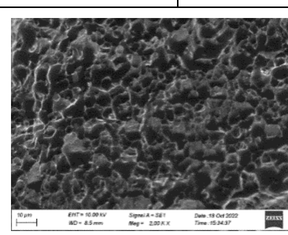	

Table 4.6: Fracture surface morphology analysis for the samples contain 0.39 wt.% C

	Irms = 636.4 A	**Irms = 777.8 A**
Frequency = 0.55 Hz	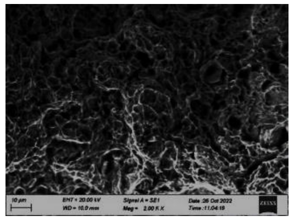	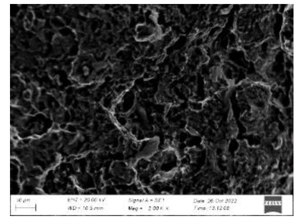
Frequency = 0.66 Hz	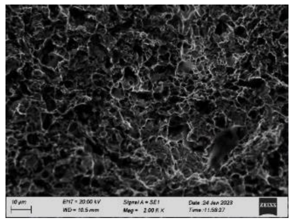	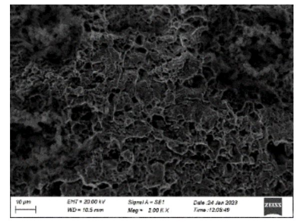
Frequency = 0.83 Hz	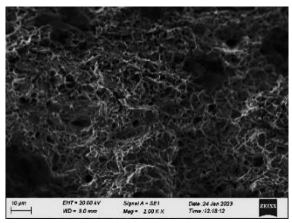	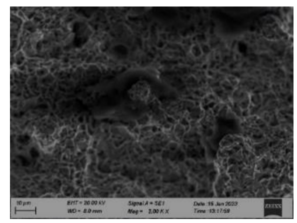
Frequency = 1.09 Hz	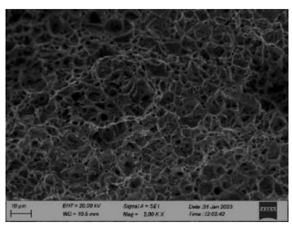	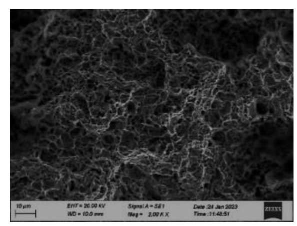
Frequency = 1.64 Hz Irms = 636.4 A	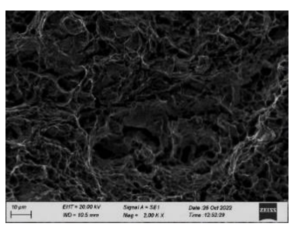	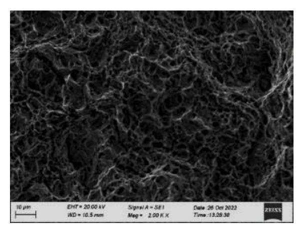
Without current	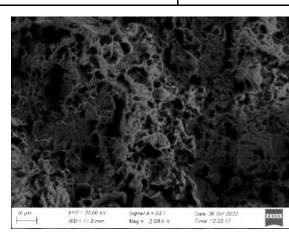	

SEM images revealing the fracture surface morphology of the selected samples are presented in table 4.5 and table 4.6. Samples containing 0.09% carbon exhibit a clearly discernible dimple structure compared to those containing 0.39% carbon. Fractographs of the tensile-tested samples without electrical pulse application reveal a relatively higher count of shallower and smaller dimples, particularly evident in the 0.09% carbon sample compared to the 0.39% carbon sample. Conversely, a smaller number of larger and deeper dimples is observable in the sample displaying the highest ductility during the tensile test, conducted at a pulse frequency of 0.83 Hz and an effective current of 777.8 A. As discussed in section 4.1.2, the fractograph of the tensile-tested sample at a higher effective current (777.8 A) and relatively higher pulse frequency (1.64 Hz) exhibits relatively smaller and shallower dimple structures, further confirming the manifestation of reduced ductility under increased energy input. Moreover, an increase in dimple size and depth was observed up to a pulse frequency of 0.83 Hz compared to the dimple structure of the fracture surface under tensile testing without electrical application in both plain carbon steel samples. The electroplasticity effect, promoting dislocation motion and plastic deformation, leads to enhanced plastic deformation, which can result in greater energy absorption and strain accommodation, consequently manifesting as larger and deeper dimples on the fracture surface.

However, a decrease in dimple size and depth was observed beyond 0.83 Hz. This reduction may be attributed to localized heating and softening caused by excessive energy input, leading to a loss of strain hardening capacity and a decrease in the material's overall ability to undergo plastic deformation. Consequently, reduced plastic flow and diminished dimple formation may occur, resulting in smaller dimple size and depth. This variation in dimple structure according to ductility is particularly evident in samples containing 0.09% carbon steel, which contains a larger fraction of ferrite compared to 0.39% carbon steel.

4.1.5 Strain energy calculation for optimum condition

Table 4.7: Toughness and strain variation of selected samples

Carbon content	Material property	Without current	With current	Percentage of increment (%)
0.09wt. %	Toughness (MJm^{-3})	53.99	82.40	52.64
	Fracture strain	0.24	0.40	70.84
0.39wt. %	Toughness (MJm^{-3})	104.70	148.60	41.93
	Fracture strain	0.25	0.38	50.89

Table 4.7 illustrates the fluctuations in toughness and strain observed among the samples subjected to tensile testing devoid of electric pulses and the specimens exhibited heightened ductility when subjected to electricity-assisted tensile testing with 0.83 Hz pulse frequency and 777.8 A effective current. Observations revealed that for both steel variants, the percentage augmentation in fracture strain surpassed the toughness. Consequently, this phenomenon holds significant implications for the manufacturing sector, particularly in contexts necessitating elevated ductility.

The area under the curve represents the energy absorbed by the sample during deformation. Despite the notably larger values observed in the area under the curve for samples subjected to the electricity-assisted tensile test (with increments of 52.64% for samples containing 0.09 wt.% carbon and 41.93% for those containing 0.039 wt.% carbon) compared to samples tested under normal conditions, a substantial increase in fracture strain was noted for both steel types (table 4.7). This observation underscores the beneficial effects of applying electric current with precise control over current amplitudes and pulse frequencies to the forming process of the specified steels. As outlined in our recent investigation [64], this phenomenon aligns with the concept of electroplasticity.

Electroplasticity promotes the retardation of dislocation accumulation by facilitating the rotation or sliding of individual grains and aiding in the motion and rearrangement of dislocations. Consequently, strain energy becomes stored within the crystal lattices. This mechanism mitigates grain elongation during the tensile test, thereby enhancing material ductility while augmenting the strain energy absorbed during the tensile test conducted with controlled pulse frequency (0.83 Hz) and effective current (777.8 A). Consequently, relative to the normal tensile test, a higher fracture strain was attained under the selected electric pulse for both steel compositions (with fracture strain increments of 70.74% for samples containing 0.09% C and 50.89% for those containing 0.39% C), notwithstanding the notable energy absorption.

4.1.6 Impact of carbon content on yield stress and ductility

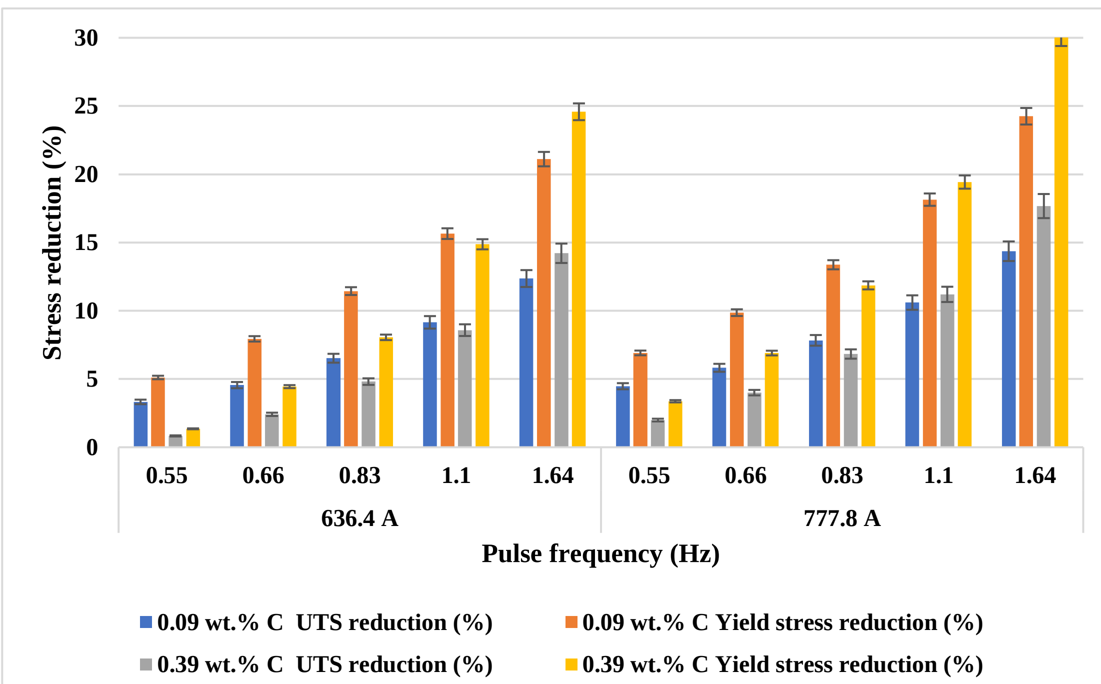

Figure 4.8 Percentage reduction of UTS and yield stress with pulse frequency and carbon content

The variation in yield stress and UTS reduction with carbon content (figure 4.8) can be understood by analyzing the phases present in low-carbon (0.09 wt.% C) and medium-carbon (0.39 wt.% C) steels. Low-carbon steel primarily consists of ferrite (α-Fe) with small amounts of pearlite, while medium-carbon steel contains a higher proportion of pearlite along with ferrite. Ferrite is a relatively soft and ductile phase with a high capacity for dislocation movement, whereas pearlite, which consists of alternating layers of ferrite and cementite, is much harder and more resistant to deformation.

At lower pulse frequencies, low-carbon steel exhibits a higher yield stress reduction because its ferrite-rich microstructure allows for easier dislocation motion. The application of electrical pulsing generates localized heating and electromigration effects, promoting softening in ferrite. In contrast, medium-carbon steel, with its higher pearlite content, resists softening initially because pearlite's structure limits dislocation movement, making it less responsive to the initial effects of electrical pulsing.

As the pulse frequency increases, medium-carbon steel begins to show a more significant yield stress reduction. This is likely due to enhanced thermal effects at higher frequencies, which lead to microstructural changes such as partial dissolution of cementite in pearlite. The weakening of the pearlitic structure reduces its strength, causing the material to exhibit greater softening. This explains why at high pulse frequencies, medium-carbon steel eventually experiences a higher percentage of yield stress reduction than low-carbon steel.

Additionally, at a higher current amplitude (777.8 A effective current) the thermal and electromagnetic effects become more pronounced, further accelerating the softening of medium-carbon steel. This trend suggests that at sufficiently high pulse frequencies and current amplitudes, medium-carbon steel becomes more affected by electrical pulsing than low-carbon steel, despite its initial resistance to softening.

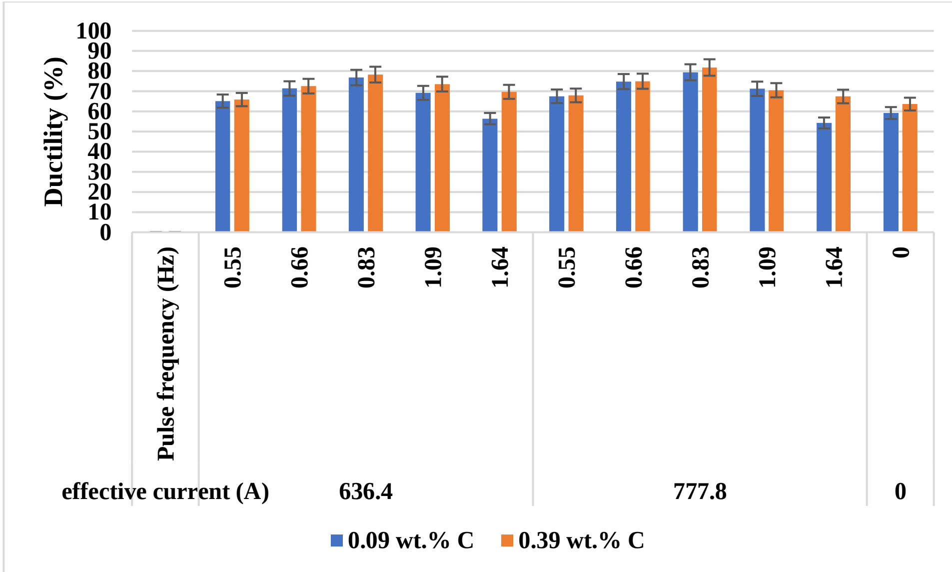

Figure 4.9 Ductility variation with pulse frequency and carbon content

The ductility of both low-carbon steel (0.09 wt.% C) and medium-carbon steel (0.39 wt.% C) varied with pulse frequency and effective current shown in figure 4.9, influenced by their microstructural composition. Under normal conditions (without electrical stimulation), the medium-carbon steel exhibited higher ductility (63.64%) compared to low-carbon steel (59.20%), likely due to the increased pearlite content in the ferrite-pearlite structure, which enhances strength while maintaining reasonable ductility. When an effective current was applied, both steels experienced an increase in ductility, peaking at a pulse frequency of 0.83 Hz. At 636.4 A, the ductility of low-carbon steel increased from 65.14% (0.55 Hz) to 76.82% (0.83 Hz), while medium-carbon steel increased from 65.89% to 78.28% within the same range. A similar trend was observed at 777.8 A, where ductility reached maximum values of 79.46% and 81.82% for low- and medium-carbon steels, respectively. This improvement can be attributed to electroplasticity, where dislocation movement is facilitated by electrical current, reducing the resistance to plastic deformation within the ferrite and pearlite phases. However, at pulse frequencies above 0.83 Hz, a decline in ductility was observed, with the lowest values recorded at 1.64 Hz. This reduction is likely due to excessive Joule heating, causing localized thermal softening and altering the balance between ferrite and pearlite deformation. Notably, medium-carbon steel consistently exhibited higher ductility across all conditions, suggesting that the pearlite-rich microstructure interacts more favorably with electroplastic effects, enhancing overall formability.

4.2 FEA for analyzing the thermal and mechanical behavior of the samples

4.2.1 Model validation

The convergence of computational results with experimental data is a pivotal aspect in validating numerical simulations. the investigation focused on demonstrating convergence by systematically decreasing the mesh size in simulations conducted using COMSOL Multiphysics software. As the mesh size decreased from an initially coarse resolution to finer levels, the stress-strain curves exhibited a discernible trend towards alignment with the experimental curve (figure 4.10). This observation underscores the importance of mesh refinement in accurately capturing the intricacies of physical phenomena. Furthermore, the stress-strain graph derived from the simulation closely aligns with the experimental data (figure 4.11 and 4.12).

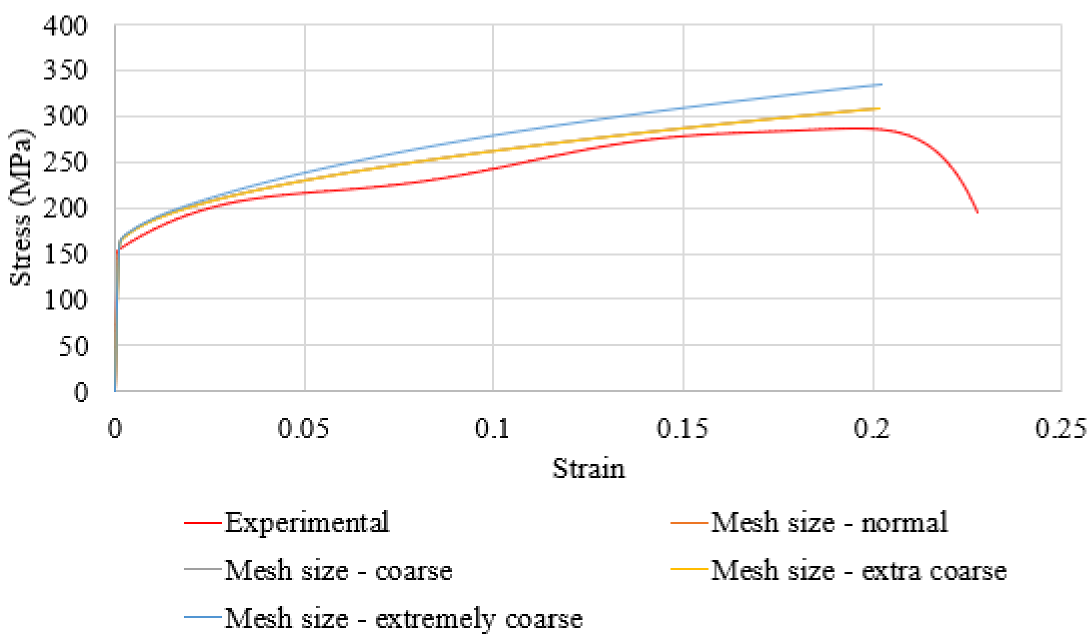

Figure 4.10: Graph for the FEA mesh convergence study

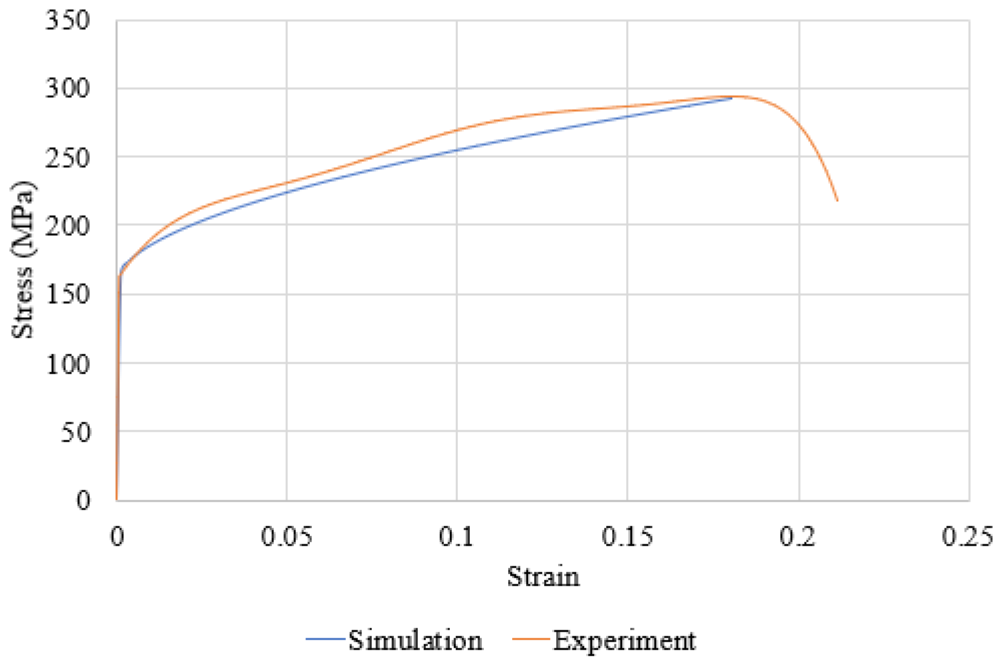

Figure 4.11: Comparison of experimental and simulation stress – strain graphs obtained under tensile test without electricity supply for 0.09 wt.% C

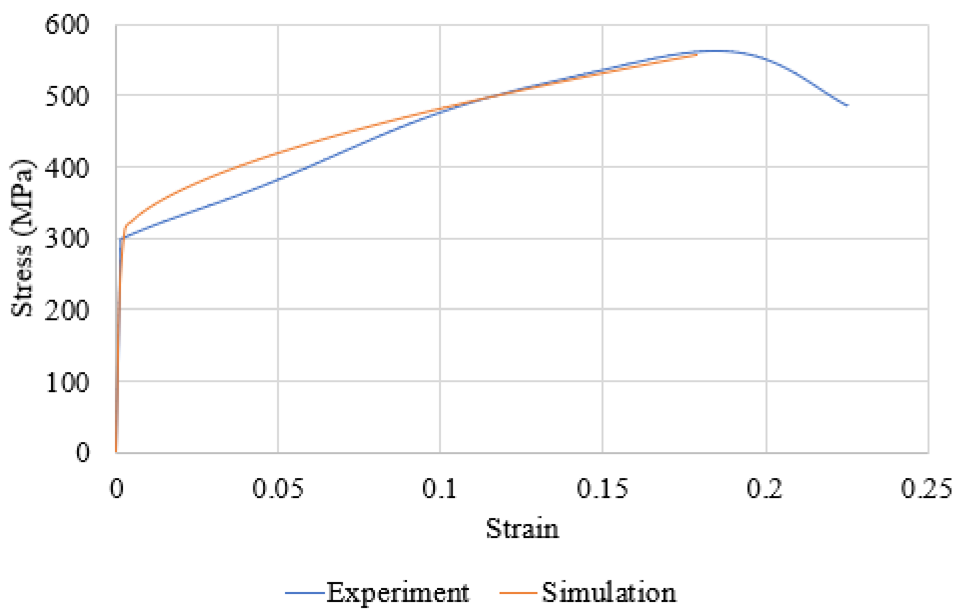

Figure 4.12: Comparison of experimental and simulation stress – strain graphs obtained under tensile test without electricity supply for 0.39 wt.% C

4.2.2 Maximum temperature of the samples variation

The increase in temperature primarily results from Joule heating, induced by the flow of electric current. Experimental results demonstrate that the maximum surface temperature of test specimens for both steel variants remains below 100°C [64]. Additionally, an observed increase in grain sizes near the fracture surface of the tensile specimens corresponds to a rise in pulse frequency. To investigate the occurrence of thermal softening or phase transformation during the tensile test under electroplasticity effects, simulations were conducted to assess temperature accumulation within the test piece. Temperature build-up during the test was calculated using equation 4 where, T is temperature, ρ is density, Cp is specific heat capacity, k is thermal conductivity and Q is heat generation. The temperature (T) was determined based on the heat generation (Q) due to the electric current passing as a heat source, which was connected to the electric current interface.

$$\rho C_p \frac{\partial T}{\partial t} - \nabla.(k \nabla T) = Q \quad (4)$$

Despite the increase in maximum temperature occurring at the stress reaching the ultimate tensile strength, which is seen to rise with pulse frequency (Figure 4.14(a), (b) and Figure 4.15(a), (b)), simulation results confirm that the maximum temperature attained within the material is insufficient to induce phase transformation for the selected steels. Specifically, maximum temperatures of 108 °C for steels with 0.09% carbon content (Figure 4.14) and 110.2 °C for those with 0.39% carbon content (Figure 4.15) were determined. FEA image of temperature variation throughout the specimen which contain 0.09 wt.% carbon at UTS is shown in figure 4.14. Consequently, it is evident that the enlarged grain sizes observed at the fracture surface stem from minimized grain elongation during the tensile test due to the electroplasticity effect, despite the lateral contraction between grains at the fracture surface due to the Poisson's effect in conventional tensile tests.

The decrease in grain elongation is supported by the electroplasticity effect, which introduces supplementary energy, distinct from strain energy, into the material under elevated electrical energy supply conditions (777.8 A effective current and 1.64 Hz pulse frequency). Hence, the sample's fracture during the tensile test could be ascribed to the breaking of metallic bonds at heightened atomic vibrational frequencies under increased energy supply. Deeper inquiries at the quantum mechanics level will elucidate the fundamental mechanisms of metallic bond rupture at intensified vibrational frequencies, providing insights into the complex interplay between atomic interactions and energy provision during tensile testing.

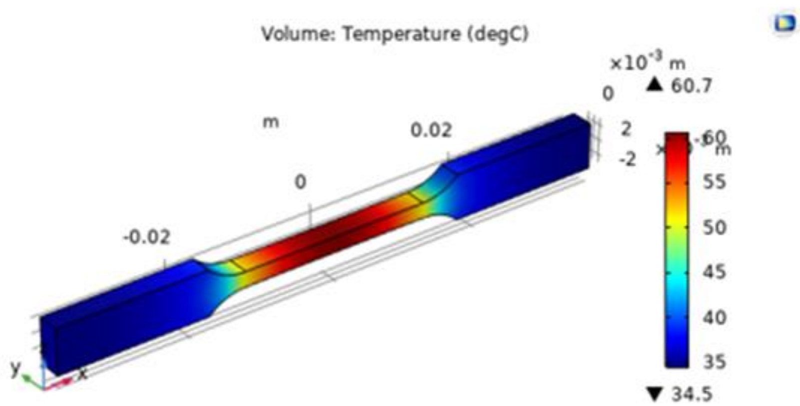

Figure 4.13: Temperature variation throughout the specimen contain 0.09 wt.% C at UTS when pulse frequency – 0.55 Hz & I_{rms} – 636.4 A

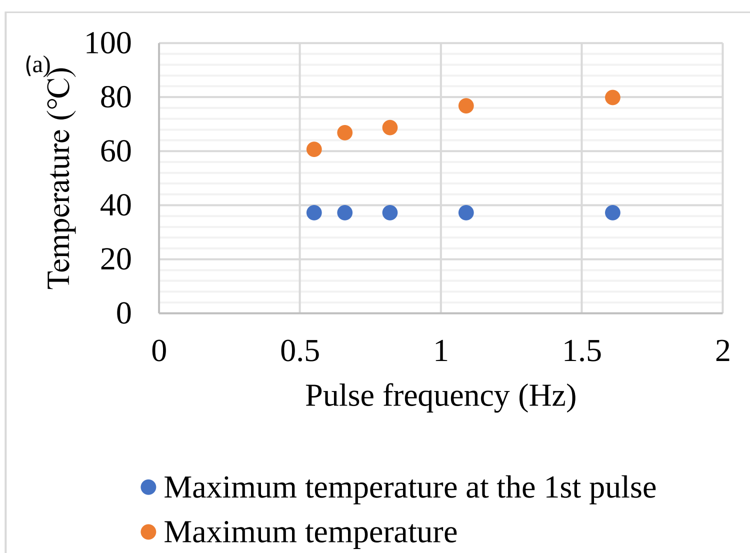

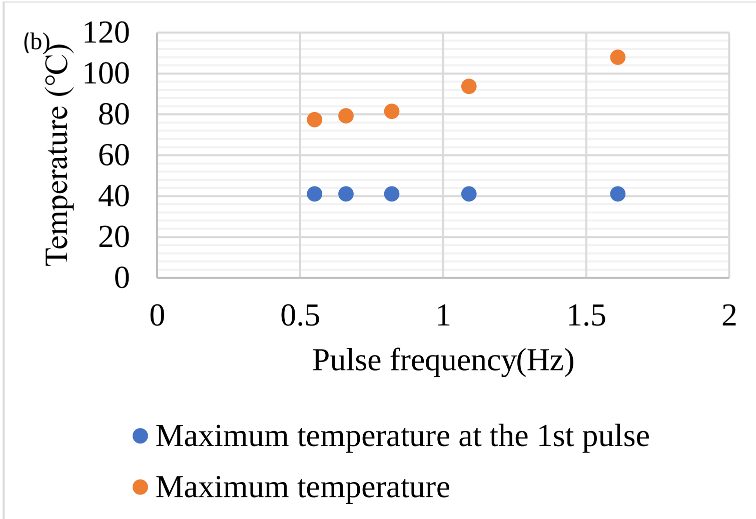

Figure 4.14: Maximum temperature variation with pulse frequency for the samples containing 0.09%C (a) Effective current – 636.4 A (b) Effective current – 777.8 A

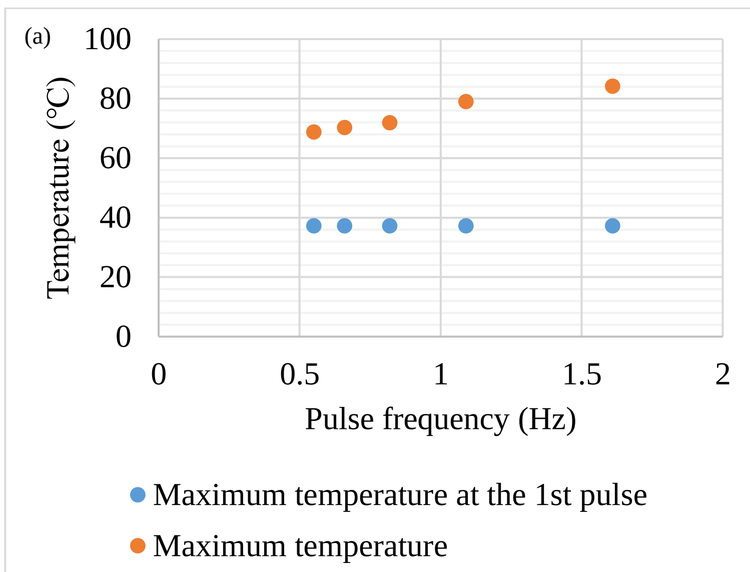

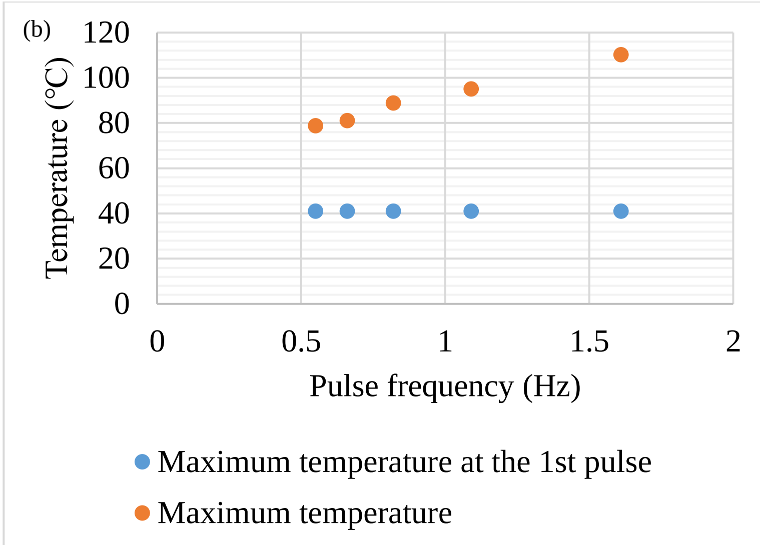

Figure 4.15: Maximum temperature variation with pulse frequency for the samples containing 0.39%C (a) Effective current – 636.4 A (b) Effective current – 777.8 A

4.2.3 Magnetic flux density variation

In the context of this study, the presence of paramagnetic obstacles within a material prompts the alignment of spins associated with these obstacles when exposed to an induced magnetic field generated by the flow of current through the material. Consequently, this alignment weakens the bond between these obstacles and dislocations, thereby facilitating dislocation movement and bolstering the plastic deformation of the metal [65]. Previous investigations have established that a magnetic flux density of 0.1 T can exert a discernible influence on the mechanical properties of materials [66]. The variation in magnetic flux density during electroplasticity-assisted tensile tests was simulated for both steels (Figure 4.16, 4.17).

$$E = -\frac{\partial A}{\partial t} \tag{5}$$

$$B = \nabla \times A \tag{6}$$

$$J = \sigma E \tag{7}$$

Here,

A – Magnetic vector potential

B – Magnetic flux density

J – Current density

E – Electric potential

σ – Electric conductivity

As per equations (5), (6), and (7), it is evident that the magnetic flux density is directly proportional to the current density. Specifically, the relevant current density was derived by concerning the interface between magnetic field physics and electric circuit physics. The findings unequivocally demonstrate that despite the induced magnetic field surpassing 0.1 T (measuring 0.11 T for 636.4 A in figure 4.16 (a) and figure 4.17 (a), and 0.14 T for 777.8 A in figure 4.16 (b) and figure 4.17 (b) for both steels), no frequency-dependent variation in the magnetic field was observed. FEA image of magnetic flux density variation throughout the sample which contain 0.09 wt.% carbon at UTS when pulse frequency – 0.55 Hz and effective current – 636.4 A is shown in figure 4.18. However, an increase in effective current resulted in a corresponding elevation in magnetic flux density for both steels.

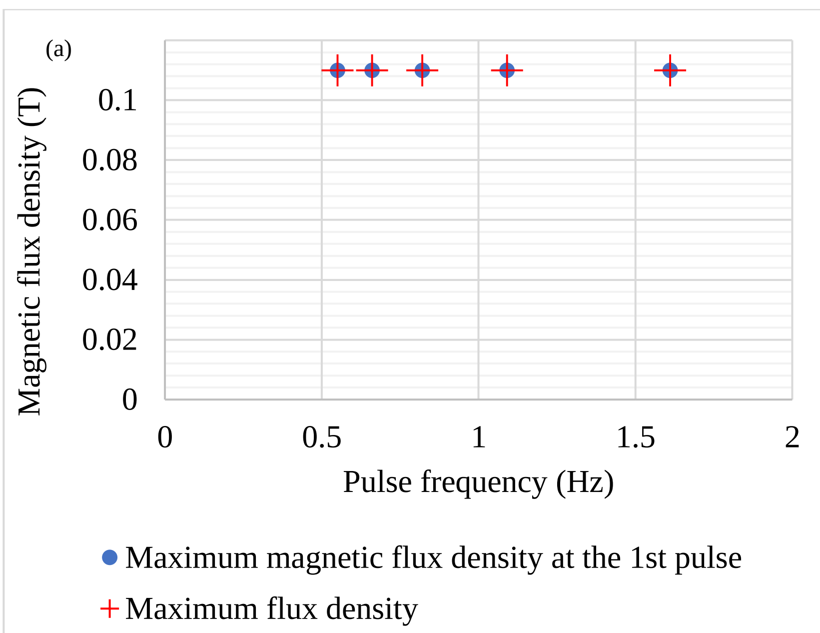

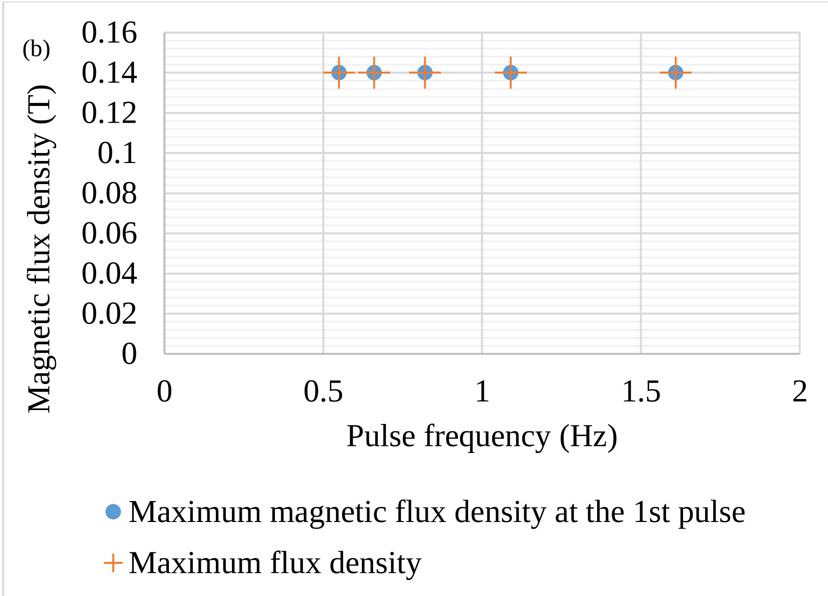

Figure 4.16: Maximum magnetic flux density variation with pulse frequency for the samples containing 0.09%C (a) Effective current – 636.4 A (b) Effective current – 777.8 A

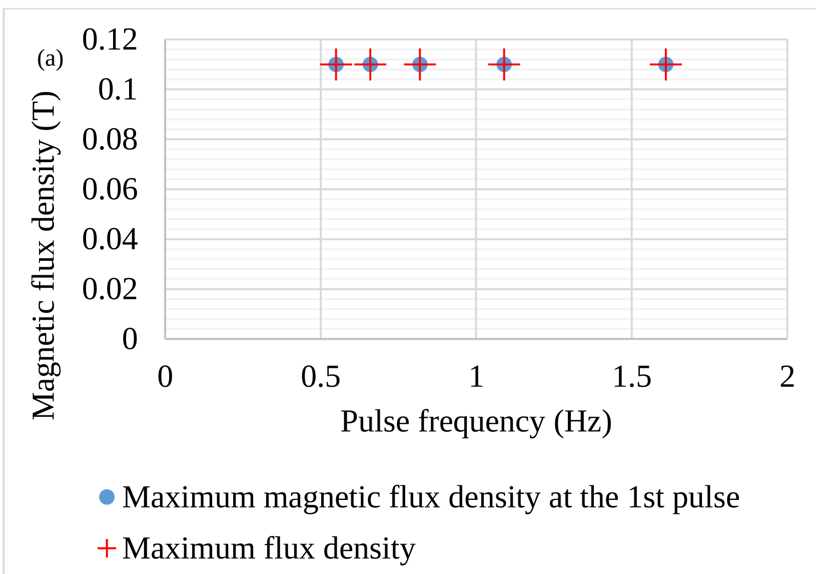

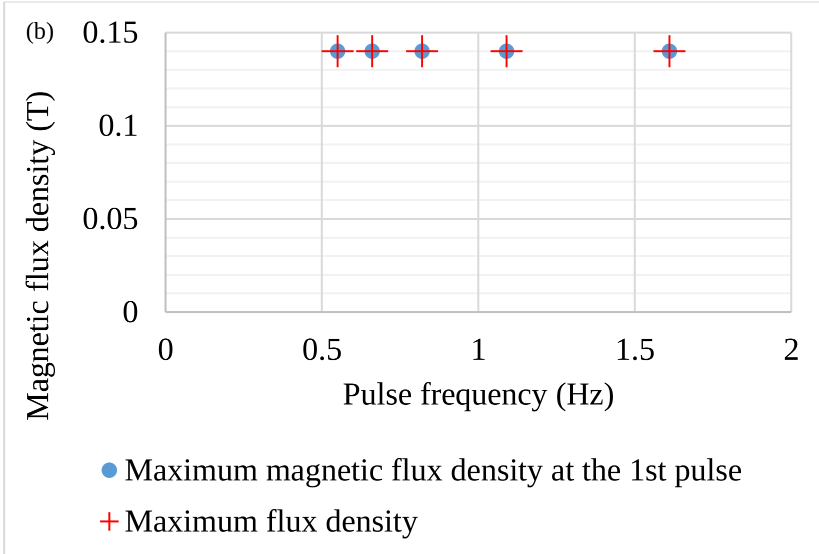

Figure 4.17: Maximum magnetic flux density variation with pulse frequency for the samples containing 0.39%C (a) Effective current – 636.4 A (b) Effective current – 777.8 A

Although the augmentation of effective current introduces more electrons into the metal, the alteration in magnetic flux density displayed no correlation with pulse frequency. This inconsistency can be attributed to the comparatively shorter on-time period (10 ms) of the electric pulses in contrast to the off-time period (> 600 ms). Consequently, it is affirmed that while pulse frequency failed to influence the variation in magnetic flux density, the effective current assumed a pivotal role in instigating a magnetic field within the metal, thereby augmenting its plasticity.

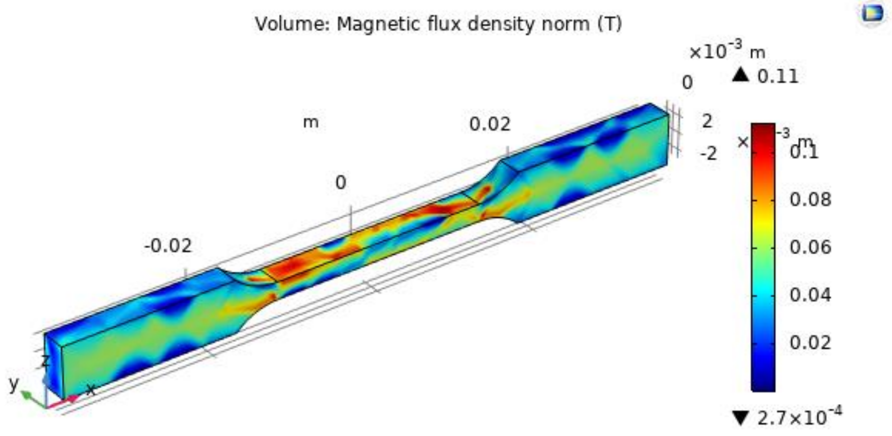

Figure 4.18: Maximum magnetic flux density variation throughout the specimen contain 0.09 wt.% C at UTS when pulse frequency – 0.55 Hz & I_{rms} – 636.4 A

4.2.4 Ultimate tensile strength variation

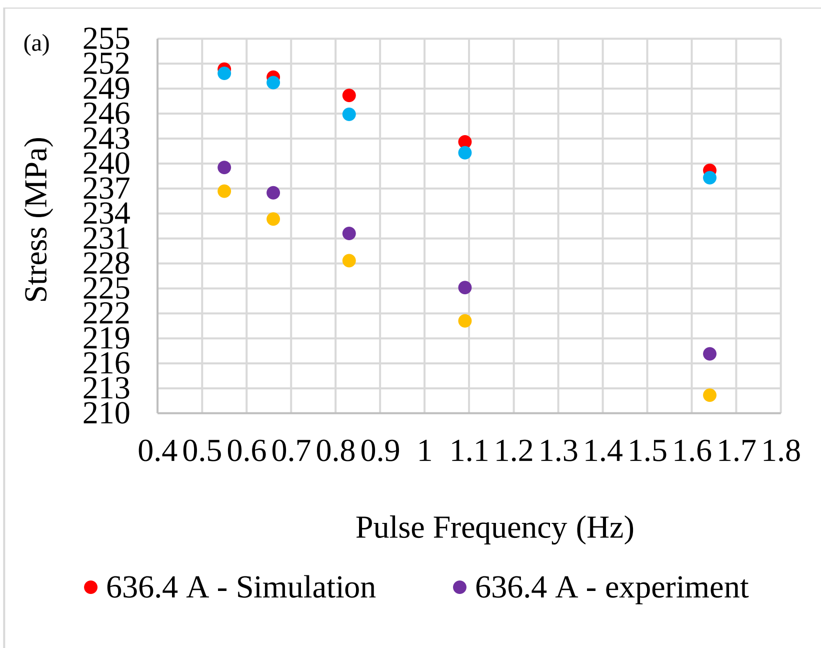

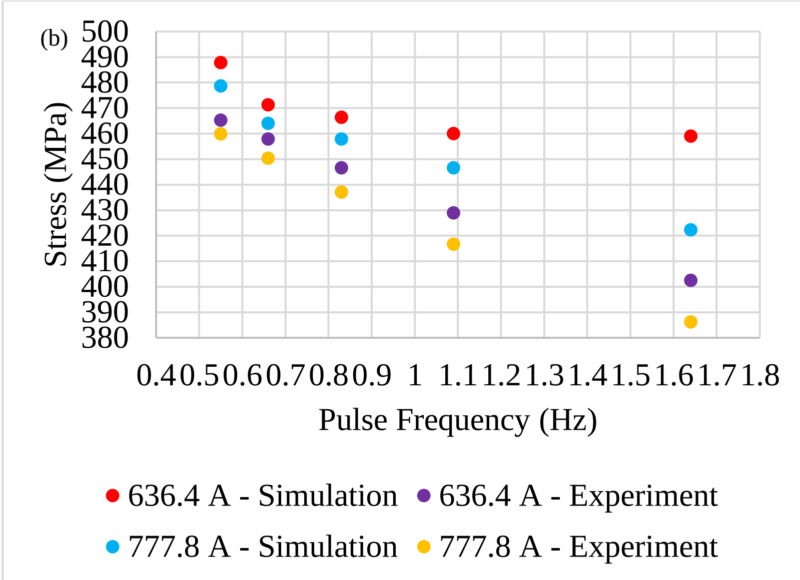

Figure 4.19: Ultimate tensile strength variation with pulse frequency (a) Samples contain 0.09%C (b) Samples contain 0.39% C

Figures 4.19 (a) and (b) depict the experimentally and computationally derived variations in ultimate tensile strength corresponding to each effective current. Notably, all simulation-generated stress-strain curves, plotted up to the ultimate tensile strength, consistently exhibited values noticeably lower than their experimental counterparts. This highlights the imperative to enhance the simulation methodology by incorporating an advanced material evaluation model. Such a model should encompass dislocation dynamics and crystal plasticity to accurately portray modifications in grain boundaries, dislocations, and other microstructural features. This enhancement is crucial for enhancing the accuracy and reliability of simulation results.

5 CONCLUSIONS AND RECOMMENDATIONS

This study investigated the influence of high-amplitude, low-frequency pulsed electric current on the formability of plain carbon steel using samples with two different carbon contents (0.09 wt.% C and 0.39 wt.% C). The findings provide valuable insights into the effects of electroplasticity, microstructural modifications, and thermal behavior under pulsed current conditions.

5.1 Proposal of appropriate parameters for pulsed electric current

A comprehensive literature review was conducted to determine suitable pulse parameters for electroplasticity studies in low and medium carbon steels. Based on the experimental results, an effective current of 777.8 A and a pulse frequency of 0.83 Hz were identified as optimal conditions for enhancing formability. The application of pulsed electric current led to a gradual reduction in yield stress with increasing pulse frequency compared to standard tensile tests. Additionally, ductility increased progressively up to a pulse frequency of 0.83 Hz, demonstrating the influence of electroplasticity on the tensile properties of carbon steels. However, beyond this frequency, ductility decreased due to a higher rate of dislocation generation than dislocation annihilation. These findings highlight the importance of selecting appropriate pulse parameters to optimize material behavior.

5.2 Investigation of microstructural changes and their influence on mechanical properties

Microstructural analysis revealed significant changes in grain structure and fracture surface characteristics under pulsed electric current. The grains at the fracture surface appeared to have an intermediate size between the as-normalized state and the samples tested without current. The observed increase in grain size at the fracture surface with increasing pulse frequency indicates an improvement in plasticity. Fractographic analysis further confirmed that the size and depth of dimples increased with pulse frequency, reinforcing the correlation between electroplasticity and enhanced ductility. However, careful control of energy input is crucial to prevent excessive material damage and fracture.

From an industrial perspective, the findings indicate that significant improvements in formability can be achieved by selecting a pulse frequency close to 0.83 Hz and an effective current of 777.8 A. This suggests that precise manipulation of pulse parameters can be used to control grain size, tailoring the mechanical properties of carbon steels to specific manufacturing requirements. Moreover, tensile testing under pulsed current application resulted in increased toughness and fracture strain for both steels. Notably, the percentage increase in fracture strain (70.84% for 0.09% C and 50.89% for 0.39% C) was higher than that of toughness (52.64% for 0.09% C and 41.93% for 0.39% C), emphasizing the potential benefits of electroplasticity in enhancing ductility.

5.3 Development and validation of a simulation model for thermal effects

A simulation model was developed to analyze the thermal effects of pulsed electric current and was validated through experimental data. The results indicated that the maximum temperature accumulation within the material was insufficient to induce phase transformations, confirming that the observed changes in mechanical behavior were primarily due to electroplasticity rather than thermal effects. Additionally, the induced magnetic flux density remained constant with pulse frequency. Specifically, a flux density of 0.11 T was recorded at an effective current of 636.4 A, while a flux density of 0.14 T was observed at 777.8 A for both steels. These findings provide further evidence that electroplasticity influences mechanical behavior independently of significant thermal contributions.

5.4 Industrial implications and future research

The phenomenon of electroplasticity can be effectively utilized to enhance the efficiency of existing cold forming processes in industrial applications. The ability to reduce yield stress and improve ductility through precise pulse current control opens opportunities for optimized manufacturing techniques, particularly in applications requiring improved formability of carbon steels.

Future research should focus on further microstructural characterization, particularly through Transmission Electron Microscopy (TEM), to confirm dislocation mechanisms under pulsed electric current. Additionally, exploring higher current amplitudes and lower pulse frequencies could provide deeper insights into the electroplasticity effect and its potential applications in advanced metal forming processes.

5.5 Project success and final remarks

The successful completion of this research demonstrates the effectiveness of pulsed electric current in enhancing the formability of plain carbon steels through electroplasticity. By systematically investigating the influence of pulse parameters, microstructural changes, and thermal effects, the study has provided valuable insights into optimizing pulse current applications for industrial metal forming processes. The experimental results align well with the developed simulation model, confirming that the observed improvements in ductility and reduction in yield stress were primarily due to electroplasticity rather than thermal effects. Furthermore, the identification of an optimal pulse frequency (0.83 Hz) and current amplitude (777.8 A) establishes a practical framework for future applications. Despite challenges encountered in the pulse generator setup, the successful implementation of the final method validates the approach taken in this research. Overall, the study contributes significantly to the understanding and practical utilization of electroplasticity in manufacturing, paving the way for improved efficiency and precision in metal forming processes.

REFERENCE

1. T. Islam and H. M. M. A. Rashed, “Classification and application of Plain Carbon Steels,” Reference Module in Materials Science and Materials Engineering, 2019. doi:10.1016/b978-0-12-803581-8.10268-1
2. A. Alaswad, K. Y. Benyounis, and A. G. Olabi, “Optimization techniques in material processing,” Reference Module in Materials Science and Materials Engineering, 2016. doi:10.1016/b978-0-12-803581-8.04004-2
3. V. I. Stashenko, O. A. Troitskii, and N. N. Novikova, “Electroplastic drawing medium-Carbon Steel,” Journal of Machinery Manufacture and Reliability, vol. 38, no. 4, pp. 369–372, 2009. doi:10.3103/s1052618809040128
4. M.-J. Kim et al., “Electric current–assisted deformation behavior of Al-mg-si alloy under uniaxial tension,” International Journal of Plasticity, vol. 94, pp. 148–170, 2017. doi:10.1016/j.ijplas.2016.09.010
5. N. Chakraborti, “The genetic secrets of making, shaping and treating of steel,” Materials and Manufacturing Processes, vol. 20, no. 3, pp. 333–334, 2005. doi:10.1081/amp-200053415
6. I. Baker, Fifty materials that make the world, 2018. doi:10.1007/978-3-319-78766-
7. J. Spoerl, “A brief history of iron and steel production,” Academia.edu, https://www.academia.edu/en/31060927/A_Brief_History_of_Iron_and_Steel_Production (accessed Jan. 16, 2024).
8. P. C. Gasson, “Materials Sciences and Engineering – Eighth Edition. W. D. Callister and D. G. Rethwisch John Wiley and Sons, the atrium, Southern Gate, Chichester, West Sussex, PO19 8SQ, UK. 2010. 968PP. illustrated. £47.99. ISBN 978-0-470-50586-1.,” The Aeronautical Journal, vol. 115, no. 1168, pp. 388–389, 2011. doi:10.1017/s0001924000005947
9. Abbas Sheyaa Alwan, Muna Abbass, and Jalal M. Jalil, “Welding consumables. covered electrodes for manual metal arc welding of Stainless and heat resisting steels. classification,” See discussions, stats, and author profiles for this publication at: https://www.researchgate.net/publication/293333803 Parametric Study of Metallurgical and Heat Transfer Characteristics of Manual Metal Arc Welding Process, Sep. 2009. doi:10.3403/01242444u
10. The Iron Carbon Phase Diagram, https://www.tf.uni-kiel.de/matwis/amat/iss/kap_6/illustr/s6_1_2.html (accessed Jan. 16, 2022).
11. B. Chandra Kandpal et al., “Effect of heat treatment on properties and microstructure of Steels,” Materials Today: Proceedings, vol. 44, pp. 199–205, 2021. doi:10.1016/j.matpr.2020.08.556 A case study of heat treatment on AISI 1020 steel - global journals, https://globaljournals.org/GJRE_Volume14/4-A-Case-Study-of-Heat.pdf (accessed Jan. 18, 2024).
12. A case study of heat treatment on AISI 1020 steel - global journals, https://globaljournals.org/GJRE_Volume14/4-A-Case-Study-of-Heat.pdf (accessed Jan. 18, 2024).

13. General Kinematics, “Cold forging vs. hot forging: Pros and cons,” General Kinematics, https://www.generalkinematics.com/blog/cold-forging-vs-hot-forging/ (accessed Jan. 26, 2022).
14. Extrusion process : Working, types, application, advantages and ..., https://paulmurphyplastics.com/2019/09/25/extrusion-process-working-types-application-advantages-and-disadvantages/ (accessed Jan. 26, 2022).
15. D. Richter, “Advantages, disadvantages of deep drawing and stamping,” Charles Richter, https://www.charlesrichter.com/the-advantages-and-disadvantages-of-deep-drawing/ (accessed Jan. 26, 2022).
16. O.A. Troitskii, V.I. Likhtman, "The anisotropy of the action of electron and γ radiation on the deformation of zinc single crystals in the brittle state," Sov. Phys. Dok., vol. 8, no. 91, 1963.
17. V. Y. KRAVCHENKO, "EFFECT OF DIRECTED ELECTRON BEAM ON MOVING DISLOCATIONS," SOVIET PHYSICS JETP, vol. 24, no. 1967, p. 6, 1966.
18. Yu. I. Bolko, Ya. E. Geguzin, and Yu. I. Klinchuk, Drag of dislocations by an electron wind in metals, http://jetp.ras.ru/cgi-bin/dn/e_054_06_1156.pdf (accessed Jan. 29, 2022).
19. X. Zhang *et al.*, “Electron Force-induced dislocations annihilation and regeneration of a superalloy through electrical in-situ transmission electron microscopy observations,” *Journal of Materials Science & Technology*, vol. 36, pp. 79–83, Jan. 2020. doi:10.1016/j.jmst.2019.08.008
20. N. K. Dimitrov, Y. Liu, and M. F. Horstemeyer, “Electroplasticity: A review of mechanisms in electro-mechanical coupling of ductile metals,” *Mechanics of Advanced Materials and Structures*, vol. 29, no. 5, pp. 705–716, Jul. 2020. doi:10.1080/15376494.2020.1789925
21. H. SONG, Z. WANG, and X. HE, “Improving in plasticity of orthorhombic ti2alnb-based alloys sheet by high density electropulsing,” *Transactions of Nonferrous Metals Society of China*, vol. 23, no. 1, pp. 32–37, Jan. 2013. doi:10.1016/s1003-6326(13)62425-5
22. A. F. Sprecher, S. L. Mannan, and H. Conrad, “On the temperature rise associated with the electroplastic effect in Titanium,” *Scripta Metallurgica*, vol. 17, no. 6, pp. 769–772, Jun. 1983. doi:10.1016/0036-9748(83)90491-x
23. M. I. Molotskii, “Theoretical basis for electro- and magnetoplasticity,” *Materials Science and Engineering: A*, vol. 287, no. 2, pp. 248–258, Aug. 2000. doi:10.1016/s0921-5093(00)00782-6
24. M. Molotskii and V. Fleurov, “Magnetic effects in electroplasticity of metals,” *Physical Review B*, vol. 52, no. 22, pp. 15829–15834, Dec. 1995. doi:10.1103/physrevb.52.15829
25. G. Lormand, “Electrical properties of grain boundaries,” *Le Journal de Physique Colloques*, vol. 43, no. C6, Dec. 1982. doi:10.1051/jphyscol:1982625

26. M.-J. Kim et al., “Elucidating the origin of electroplasticity in metallic materials,” Applied Materials Today, vol. 21, p. 100874, Dec. 2020. doi:10.1016/j.apmt.2020.100874
27. T. A. Perkins, T. J. Kronenberger, and J. T. Roth, “Metallic forging using electrical flow as an alternative to warm/hot working,” *Journal of Manufacturing Science and Engineering*, vol. 129, no. 1, pp. 84–94, Jun. 2006. doi:10.1115/1.2386164
28. C. M. Dzialo, M. S. Siopis, B. L. Kinsey, and K. J. Weinmann, “Effect of current density and zinc content during electrical-assisted forming of Copper Alloys,” CIRP Annals, vol. 59, no. 1, pp. 299–302, 2010. doi:10.1016/j.cirp.2010.03.014
29. C. D. Ross, T. J. Kronenberger, and J. T. Roth, “Effect of DC on the formability of ti–6al–4v,” *Journal of Engineering Materials and Technology*, vol. 131, no. 3, May 2009. doi:10.1115/1.3078307
30. W. A. Salandro, C. Bunget, and L. Mears, “Modeling and quantification of the electroplastic effect when bending stainless steel sheet metal,” *ASME 2010 International Manufacturing Science and Engineering Conference, Volume 1*, Jan. 2010. doi:10.1115/msec2010-34043
31. C. D. Lang *et al.*, “Electrically-assisted manufacturing for reduction in forging forces of bearing steels,” *Procedia Manufacturing*, vol. 48, pp. 349–357, 2020. doi:10.1016/j.promfg.2020.05.057
32. H.-D. Nguyen-Tran *et al.*, “A review of electrically-assisted manufacturing,” *International Journal of Precision Engineering and Manufacturing-Green Technology*, vol. 2, no. 4, pp. 365–376, Oct. 2015. doi:10.1007/s40684-015-0045-4
33. Z. Xu, G. Tang, S. Tian, F. Ding, and H. Tian, “Research of electroplastic rolling of Az31 MG Alloy Strip,” *Journal of Materials Processing Technology*, vol. 182, no. 1–3, pp. 128–133, Feb. 2007. doi:10.1016/j.jmatprotec.2006.07.019
34. Y. Lu *et al.*, “The influence of electroplastic rolling on the mechanical deformation and phase evolution of Bi-2223/Ag Tapes,” *Journal of Materials Science*, vol. 45, no. 13, pp. 3514–3519, Mar. 2010. doi:10.1007/s10853-010-4392-9
35. R. Zhu, G. Tang, S. Shi, and M. Fu, “Effect of electroplastic rolling on deformability and oxidation of NITINB shape memory alloy,” *Journal of Materials Processing Technology*, vol. 213, no. 1, pp. 30–35, Jan. 2013. doi:10.1016/j.jmatprotec.2012.08.001
36. R. F. Zhu, G. Y. Tang, S. Q. Shi, and M. W. Fu, “Effect of electroplastic rolling on the ductility and superelasticity of Tini shape memory alloy,” *Materials & Design*, vol. 44, pp. 606–611, Feb. 2013. doi:10.1016/j.matdes.2012.08.045
37. G. Tang, J. Zhang, Y. Yan, H. Zhou, and W. Fang, “The engineering application of the electroplastic effect in the cold-drawing of stainless steel wire,” *Journal of Materials Processing Technology*, vol. 137, no. 1–3, pp. 96–99, Jun. 2003. doi:10.1016/s0924-0136(02)01091-9

38. V. I. Stashenko, O. A. Troitskii, and N. N. Novikova, “Electroplastic drawing medium-Carbon Steel,” *Journal of Machinery Manufacture and Reliability*, vol. 38, no. 4, pp. 369–372, Aug. 2009. doi:10.3103/s1052618809040128
39. J. Asghar and R. N. V, Importance of Tool Configuration in Incremental Sheet Metal Forming of Difficult to Form Materials using Electro-Plasticity, https://raiith.iith.ac.in/902/1/WCE2013_pp1734-1738.pdf (accessed Feb. 16, 2022).
40. Z. T. Xu, L. F. Peng, P. Y. Yi, and X. M. Lai, “Study on a novel electrical-assisted pressure welding process of thin metallic foils,” *Applied Mechanics and Materials*, vol. 271–272, pp. 147–151, Dec. 2012. doi:10.4028/www.scientific.net/amm.271-272.147
41. S. A. Baranov, V. I. Staschenko, A. V. Sukhov, O. A. Troitskiy, and A. V. Tyapkin, “Electroplastic Metal cutting,” *Russian Electrical Engineering*, vol. 82, no. 9, pp. 477–479, Sep. 2011. doi:10.3103/s1068371211090033
42. O. Omoigiade, “Electric current as a steel wire manufacturing tool,” *Materials Science and Technology*, vol. 34, no. 18, pp. 2202–2213, Dec. 2018. doi:10.1080/02670836.2018.1488435
43. W. A. Salandro *et al.*, “Effect of electrical pulsing on various heat treatments of 5xxx series aluminum alloys,” *ASME 2008 International Manufacturing Science and Engineering Conference, Volume 1*, Jan. 2008. doi:10.1115/msec_icmp2008-72512
44. X. Li, X. Li, J. Zhu, X. Ye, and G. Tang, “Microstructure and texture evolution of cold-rolled MG-3al-1ZN alloy by electropulse treatment stimulating recrystallization,” *Scripta Materialia*, vol. 112, pp. 23–27, Feb. 2016. doi:10.1016/j.scriptamat.2015.09.001
45. P. Liang and K.-L. Lin, “Non-deformation recrystallization of metal with electric current stressing,” *Journal of Alloys and Compounds*, vol. 722, pp. 690–697, Oct. 2017. doi:10.1016/j.jallcom.2017.06.032
46. V. Delobelle, G. Chagnon, D. Favier, and T. Alonso, “Study of electropulse heat treatment of cold worked niti wire: From uniform to localised tensile behaviour,” *Journal of Materials Processing Technology*, vol. 227, pp. 244–250, Jan. 2016. doi:10.1016/j.jmatprotec.2015.08.011
47. S. A. Davari and A. S. Wexler, “Quantification of toxic metals using machine learning techniques and spark emission spectroscopy,” Atmospheric Measurement Techniques, vol. 13, no. 10, pp. 5369–5377, Oct. 2020, doi: https://doi.org/10.5194/amt-13-5369-2020.
48. V. Soleymani and B. Eghbali, “Grain Refinement in a Low Carbon Steel Through Multidirectional Forging,” Journal of Iron and Steel Research International, vol. 19, no. 10, pp. 74–78, Oct. 2012, doi: https://doi.org/10.1016/s1006-706x(12)60155-1.
49. J. Duan, D. Farrugia, C. Davis, and Z. Li, “Effect of impurities on the microstructure and mechanical properties of a low carbon steel,” Ironmaking & Steelmaking, vol.

49, no. 2, pp. 140–146, Sep. 2021, doi: https://doi.org/10.1080/03019233.2021.1972270.
50. H.-J. Jeong, J. Park, K. J. Jeong, N. M. Hwang, S.-T. Hong, and H. N. Han, “Effect of Pulsed Electric Current on TRIP-Aided Steel,” International Journal of Precision Engineering and Manufacturing-Green Technology, vol. 6, no. 2, pp. 315–327, Feb. 2019, doi: https://doi.org/10.1007/s40684-019-00060-1
51. H. Xu et al., “Effect of Pulsed Current on the Tensile Deformation Behavior and Microstructure Evolution of AZ80 Magnesium Alloy,” Materials, vol. 13, no. 21, pp. 4840–4840, Oct. 2020, doi: https://doi.org/10.3390/ma13214840.
52. B. Jiang, D. Zhang, H. Xu, Y. Liu, Z. Cao, and X. Yang, “Excellent Ductility in the Extruded AZ61 Magnesium Alloy Tube Induced by Electropulsing Treatment during Tension,” Metals, vol. 11, no. 5, pp. 813–813, May 2021, doi: https://doi.org/10.3390/met11050813.
53. Jae Kyung Roh, Jeong Gil Seo, S.-T. Hong, M.-J. Kim, Heung Nam Han, and J. R. Roth, “The mechanical behavior of 5052-H32 aluminum alloys under a pulsed electric current,” International Journal of Plasticity, vol. 58, pp. 84–99, Jul. 2014, doi: https://doi.org/10.1016/j.ijplas.2014.02.002.
54. H.-J. Jeong, J. Park, K. J. Jeong, N. M. Hwang, S.-T. Hong, and H. N. Han, “Effect of Pulsed Electric Current on TRIP-Aided Steel,” International Journal of Precision Engineering and Manufacturing-Green Technology, vol. 6, no. 2, pp. 315–327, Feb. 2019, doi: https://doi.org/10.1007/s40684-019-00060-1.
55. B. Roodenburg, J. Morren, H. E. (Iekje) Berg, and S. W. H. de Haan, “Metal release in a stainless steel Pulsed Electric Field (PEF) system,” Innovative Food Science & Emerging Technologies, vol. 6, no. 3, pp. 327–336, Sep. 2005, doi: https://doi.org/10.1016/j.ifset.2005.04.006.
56. Ichsan Indhiarto, T. Shimizu, and M. Yang, “Effect of Peak Current Density on Tensile Properties of AZ31B Magnesium Alloy,” Materials, vol. 14, no. 6, pp. 1457–1457, Mar. 2021, doi: https://doi.org/10.3390/ma14061457.
57. N. T. Thien, Y.-H. Jeong, S.-T. Hong, M.-J. Kim, H. N. Han, and M.-G. Lee, “Electrically assisted tensile behavior of complex phase ultra-high strength steel,” International Journal of Precision Engineering and Manufacturing-Green Technology, vol. 3, no. 4, pp. 325–333, Oct. 2016, doi: https://doi.org/10.1007/s40684-016-0041-3.
58. N. Hendeniya, G. A. Abeygunawardena, I. De. Silva, and S. Wickramasinghe, “The tensile electroplasticity of low carbon steel with low amplitude pulse current,” *2020 Moratuwa Engineering Research Conference (MERCon)*, Jul. 2020. doi:10.1109/mercon50084.2020.9185238
59. *Metals Handbook*. Metals Park, OH, 1998.
60. H. Zhang and J. Senkara, *Resistance Welding: Fundamentals and Applications*. Boca Raton (FL): CRC Press, 2012.

61. K. Vedantam, “Johnson - cook strength models for mild and DP 590 steels,” *AIP Conference Proceedings*, 2006. doi:10.1063/1.2263437
62. L. Dingle and M. H. Tooley, *Aircraft Engineering Principles*. London: Routledge, 2017.
63. I. INDHIARTO, “Investigation of Peak Current Density Effect on Magnesium Alloy AZ31B Foil Tensile Properties under High Density Pulsed Current,” National Institute of Informatics, https://tokyo-metro-u.repo.nii.ac.jp/record/2138/files/T00252-001_fulltext.pdf (accessed Mar. 15, 2022).
64. A. Rahnama and R. Qin, “Room temperature texturing of austenite/ferrite steel by electropulsing,” *Scientific Reports*, vol. 7, no. 1, Feb. 2017. doi:10.1038/srep42732
65. T. Dhanushka, G. A. Abeygunawardena, and I. De. Silva, “Effect of pulsed current frequency on electroplasticity in Plain Carbon Steel: An experimental study,” *2023 Moratuwa Engineering Research Conference (MERCon)*, Nov. 2023. doi:10.1109/mercon60487.2023.10355493
66. A. Lahiri, P. Shanthraj, and F. Roters, "Understanding the mechanisms of electroplasticity from a crystal plasticity perspective," Model. Simul. Mater. Sci. Eng., vol. 27, no. 8, 2019, doi: 10.1088/1361-651X/ab43fc.
67. C. W. Burrows, *Correlation of the Magnetic and Mechanical Properties of Steel, by Charles W. Burrows* .. Washington: Government printing Office, 1926.